NASA TECHNICAL NOTE

NASA TN D-7624

NASA TN D-7624

HELICOPTER ROTOR ROTATIONAL NOISE PREDICTIONS BASED ON MEASURED HIGH-FREQUENCY BLADE LOADS

Robert N. Hosier
Langley Directorate
U.S. Army Air Mobility R&D Laboratory

Ramani Ramakrishnan
The George Washington University
Joint Institute for Acoustics and Flight Sciences

Langley Research Center
Hampton, Va. 23665

NATIONAL AERONAUTICS AND SPACE ADMINISTRATION • WASHINGTON, D. C. • DECEMBER 1974

1. Report No.	2. Government Accession No.	3. Recipient's Catalog No.
NASA TN D-7624		

4. Title and Subtitle	5. Report Date
HELICOPTER ROTOR ROTATIONAL NOISE PREDICTIONS BASED ON MEASURED HIGH-FREQUENCY BLADE LOADS	December 1974
	6. Performing Organization Code

7. Author(s)	8. Performing Organization Report No.
Robert N. Hosier and Ramani Ramakrishnan (See Supplementary Notes, block 15)	L-9358
	10. Work Unit No. 760-63-02-11
9. Performing Organization Name and Address	11. Contract or Grant No.
NASA Langley Research Center Hampton, Va. 23665	
	13. Type of Report and Period Covered Technical Note
12. Sponsoring Agency Name and Address	14. Sponsoring Agency Code
National Aeronautics and Space Administration Washington, D.C. 20546	

15. Supplementary Notes

Robert N. Hosier: Langley Directorate, U.S. Army Air Mobility R&D Laboratory

Ramani Ramakrishnan: The George Washington University, Joint Institute for Acoustics and Flight Sciences

16. Abstract

In tests conducted at the Langley helicopter rotor test facility, simultaneous measurements of up to 200 harmonics of the fluctuating aerodynamic blade surface pressures and far-field radiated noise were made on a full-scale nontranslating rotor system. After their characteristics were determined, the measured blade surface pressures were converted to loading coefficients and used in an existing theory to predict the far-field rotational noise. A comparison of the calculated and measured noise shows generally good agreement up to 300 to 600 Hz, depending on the discreteness of the loading spectrum. Specific attention is given to the effects of the blade loading coefficients, chordwise loading distributions, blade loading phases, and observer azimuthal position on the calculations.

17. Key Words (Suggested by Author(s))	18. Distribution Statement
Rotational noise Helicopter Blade loads Loading distributions	Unclassified – Unlimited STAR Category 01

19. Security Classif. (of this report)	20. Security Classif. (of this page)	21. No. of Pages	22. Price*
Unclassified	Unclassified	84	$4.75

*For sale by the National Technical Information Service, Springfield, Virginia 22151

CONTENTS

HELICOPTER ROTOR ROTATIONAL NOISE PREDICTIONS BASED ON MEASURED HIGH-FREQUENCY BLADE LOADS

Robert N. Hosier
Langley Directorate, U.S. Army Air Mobility R&D Laboratory

Ramani Ramakrishnan
The George Washington University
Joint Institute for Acoustics and Flight Sciences

SUMMARY

The results of tests, conducted at the Langley helicopter rotor test facility, which simultaneously measured up to 200 harmonics of the fluctuating aerodynamic blade surface pressures and the far-field radiated noise are reported. These tests were conducted on a full-scale nontranslating rotor system. The experimental apparatus and procedures, data reduction and analysis, generalized loading results, and rotational noise theory are discussed. After their characteristics were determined, the measured blade surface pressures were converted to loading coefficients and used in an existing theory to predict the far-field rotational noise. The effects of the blade loading coefficients, chordwise loading distribution, blade loading phases, and observer azimuthal position on the noise calculations are explained. A comparison of the calculated and measured noise shows generally good agreement through 300 to 600 Hz, depending on the discreteness of the loading spectrum. These data form an important step in developing the ability to predict rotor noise from aircraft while in the design stage.

INTRODUCTION

The detectability and community acceptance of helicopters depend in a large part on the noise characteristics of the main and tail rotors. This rotor noise can be conveniently grouped into two general categories, broadband and discrete. Some of the sources of broadband noise are the tip and trailing-edge vortices and boundary-layer turbulence. Discrete noise consists of impulsive noise such as blade-vortex interaction and advancing-blade compressibility shock, thickness noise resulting from mass displacement near transonic tip speeds, and rotational noise generated by thrust and drag forces.

In most flight conditions the predominant rotor noise source is the rotational noise. For many years this noise was predicted from a knowledge of only the uniform aerodynamic loads (ref. 1) but, except at high tip speeds, agreement with measured acoustic data was poor beyond the first few harmonics.

In the mid 1960's theoreticians postulated that the rotational noise could be attributed to both the uniform and fluctuating aerodynamic lift and drag forces. Rotational-noise prediction theories, based on the fluctuating blade-force assumption, were then developed, and theoretical calculations of rotational noise were made (refs. 2 to 10). These theories, all of similar content, required a priori knowledge of the amplitude and distribution of the high-frequency fluctuating aerodynamic blade surface pressures to calculate the far-field rotational noise. However, no measurements of these pressures existed. (In refs. 6 and 11 approximately 30 and 10 pressure harmonics, respectively, were measured, but for the purpose of the computations in this report on the order of 100 or more pressure harmonics are required.) Because of the lack of data, theoretical models of the fluctuating blade surface pressure spectra were developed and the agreement between calculated and measured rotational noise was found to be dependent on the loading model chosen. In reference 6, five sound harmonics were computed and fell within 10 dB of measured data.

In reference 12 the combined rotational and broadband noise from helicopter main and tail rotors is calculated from computed rotor performance parameters. The rotational noise calculations are made for hover and forward flight and the results agree with measured data within 10 dB up to about 10th sound harmonic.

In reference 7 the rotational noise equations were developed in terms of blade loading coefficients (the ratio of a blade pressure harmonic to the uniform pressure) and chordwise-loading-distribution functions. Although spanwise loading distributions are also included, it is suggested that the loading can be concentrated at an effective blade radius. Reference 13 contains a critical review of the theories of references 6 and 7. Reference 14 suggests that the mechanisms for the fluctuating aerodynamic blade loads are inflow turbulence, gusts, rotor-fuselage interaction and rotor-wake interaction.

This paper reports results from tests conducted at the Langley helicopter rotor test facility which simultaneously measured both the fluctuating-aerodynamic-blade surface pressures and the radiated rotor noise. In some conditions, as many as 200 pressure harmonics were measured and used in conjunction with the theory of references 7 and 8 to predict the far-field noise. Specific attention is given to the experimental equipment, instrumentation, and procedures, the data reduction and analysis, the generalized loading results, the rotational noise theory, a discussion of the blade pressure and loading data, and a comparison of measured and calculated rotational noise based on the measured fluctuating blade loading coefficients. The importance of chordwise loading distributions, blade-loading phase angles, and observer azimuthal position are also discussed.

SYMBOLS

The units for the physical quantities defined in this paper are given both in the International System of Units, SI, and the U.S. Customary Units.

A	rotor disk area, m^2 (ft^2)
a_0	speed of sound, m/sec (ft/sec)
B	number of blades
C_0	Fourier coefficient of zeroth order
C_m	Fourier coefficient of m^{th} order
$\overline{C}_L$	mean rotor lift coefficient, $6C_T/\sigma$
C_T	rotor thrust coefficient, $T_T/\rho A V_t^2$
c	blade chord, m (ft)
D	observer distance from source, m (ft)
D_F	total rotor drag force, $L_T \sin \beta$, N (lb)
$\overline{F}$	force vector, N (lb)
F_i	i^{th} component of $\overline{F}$
$\bar{f}_0$	force vector normal to $\bar{y}$ (see appendix A and fig. 20)
$J_q(Z_0)$	Bessel function of the first kind of order q and argument Z_0
$j = \sqrt{-1}$	
K_D	drag operating constant $\frac{ND_F}{Ra_0M_e}$, N/m^2 (lb/ft^2)
K_L	lift operating constant $\frac{NL_F}{Ra_0} \sin \sigma'$, N/m^2 (lb/ft^2)
L	load per blade per unit span, N/m (lb/ft)
L_F	total rotor lift force $L_T \cos \beta$, N (lb)
L_T	total rotor aerodynamic load, N (lb)

M_e	effective Mach number, $0.8M_t$
M_t	tip Mach number, $\Omega r_t/a_0$
m,mB	sound pressure harmonic numbers
N	rotor shaft frequency, Hz
P	general blade pressure, N/m^2 (lb/ft^2)
P_q,P_s	amplitude of q^{th} or s^{th} fluctuating blade pressure harmonic, N/m^2 (lb/ft^2)
P_{rms}	root-mean-square amplitude of fluctuating blade pressure, N/m^2 (lb/ft^2)
P_0	amplitude of zeroth (uniform) blade pressure harmonic, N/m^2 (lb/ft^2)
p	acoustic pressure, N/m^2 (lb/ft^2)
q	mode number ($q_\pm = mB \pm s$)
R	observer distance from rotor center, m (ft)
r_t	rotor tip radius, m (ft)
r	distance along rotor measured from rotor center, m (ft)
r_e	effective rotor radius $0.8r_t$, m (ft)
SP	sound pressure, N/m^2 (lb/ft^2)
SPL	sound-pressure level, dB (re 0.00002 N/m^2)
SP_{mB}	amplitude of mB^{th} sound pressure harmonic, N/m^2 (lb/ft^2)
S_q	jump function ($S_q = 0$ for $q < mB$; $S_q = 1$ for $mB \leq q$)
s	pressure or loading harmonic number
T_T	total rotor thrust, N (lb)

t	time variable, sec
V_t	rotor tip speed Ωr_t, m/sec (ft/sec)
$\bar{x}$	observer coordinate vector, m (ft)
x_1, x_2, x_3	rectangular coordinates
$\bar{y}$	source coordinate vector, m (ft)
Z_0	Bessel function argument, $mBM_e \cos \sigma'$
α_{rms}	root-mean-square blade loading coefficient, $\frac{P_{rms}}{P_0}$
α_s	s^{th} blade loading coefficient, $\frac{P_s}{P_0}$
β	effective blade force angle, rad
γ_q	limit and directivity function, $mBJ_q(Z_0)$
Δ	increment
$\delta( )$	Dirac delta function
η, ξ	arbitrary phase constants, rad
θ	blade-observer azimuthal angle, rad
λ_{mB}	wavelength of mB^{th} acoustic harmonic
ρ	density of air, kg/m^3 (slugs/ft^3)
σ	rotor solidity, $\frac{Bc}{\pi r_t}$
σ'	observer elevation angle, rad
τ	time period, sec
ϕ_q, ϕ_s	phase angles of the blade pressure or blade loading harmonic, rad

χ_{mB} chordwise loading distribution spectrum function

ψ rotor azimuthal angle, rad

Ω angular frequency $2\pi N$

Subscripts:

diff differential

g gage

int integrated

rms root mean square

EXPERIMENTAL EQUIPMENT, INSTRUMENTATION, AND PROCEDURES

To provide the previously unavailable high frequency aerodynamic blade surface pressures necessary to validate the rotational noise theories, a full scale test was conducted to simultaneously measure the fluctuating blade surface pressures and the far-field radiated noise. This section outlines the experimental equipment, instrumentation, and procedures used in this test.

Equipment

Helicopter rotor test facility.- The fluctuating blade surface pressures were measured at the Langley helicopter rotor test facility shown in figure 1. Although the rotor used had a diameter of 10.65 m (35 ft), this facility can be used to study rotors up to 21.3 m (70 ft) in diameter. It has a maximum rpm, thrust, and torque capability of approximately 400 rpm, 66.723 kN (15 000 lb), and 24.4 kN-m (18 000 ft-lb), respectively. The facility is equipped with 60 slip rings to transmit the data from the rotating blades to the ground recording station.

Rotor system.- The rotor system used for the tests was a four-bladed hingeless rotor. Table I provides a general description of the rotor. A more complete description can be found in references 15, 16, and 17.

Microphone array.- The radiated far-field noise was measured with two microphones located 45.72 m (150 ft) from the rotor axis as shown in figure 2. The first microphone was 9.14 m (30 ft) above the rotor disk plane; the second microphone was in the rotor disk plane.

L-74-1888

Figure 1.- Langley helicopter rotor test facility.

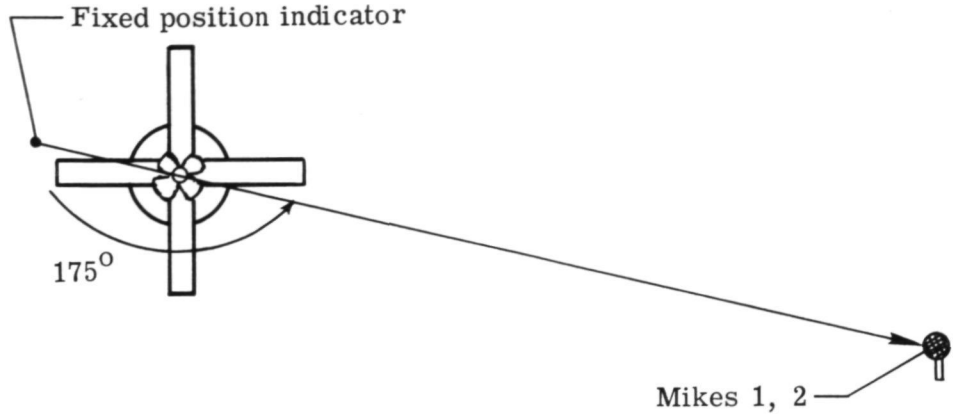

(a) Plan view.

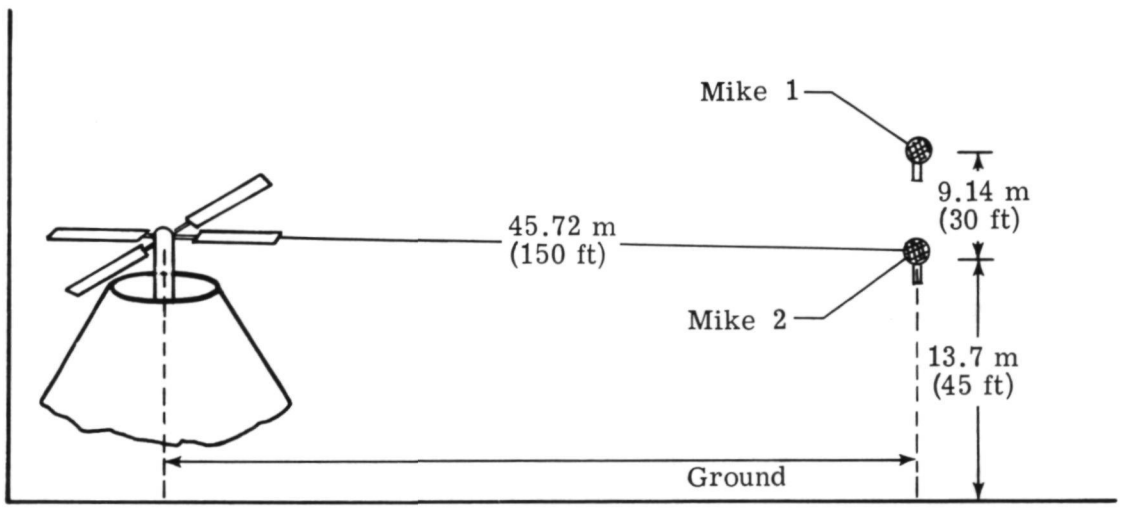

(b) Elevation view.

Figure 2.- Schematic of microphone positions.

TABLE I.- ROTOR SYSTEM PARAMETERS

Type rotor system	Hingeless
Diameter, m (ft)	10.67 (35)
Number of blades	Four
Blade chord, m (in.)	0.33 (13)
Blade weight per blade, N (lb)	382.5 (86)
Airfoil section	Modified NACA 0012
Blade taper	0
Total blade twist (root to tip), deg	-5
Disk area, m^2 (ft^2)	88.5 (962)
Solidity	0.0818
Forward blade sweep, deg	1.4

Performance measurement system.- The rotor performance parameters – thrust, shaft torque, rpm, and geometric blade tip pitch – were measured by a system of strain-gage bridges and potentiometers. The output of these sensors was monitored with digital voltmeters and manually recorded in a test log.

Instrumentation

Two data acquisition systems, one for blade surface pressure measurements and one for acoustic measurements, were used for these tests. Each system, with its accompanying subsystems, is described in this section.

Blade surface pressure measurements.- The high-frequency fluctuating blade pressures were measured using the system shown as a block diagram in figure 3. This system may be divided into three distinct sections: pressure transducers, signal conditioners, and data recording equipment.

Pressure transducers: The high-frequency fluctuating-blade surface pressures were obtained from commercially available semiconductor strain-gage absolute-pressure transducers which were sealed at atmospheric pressure (see fig. 4). These paddle type transducers had a flat frequency response from dc to 5000 Hz with a resonance frequency of 25 000 Hz. When excited by 10 V dc, the transducer produced an output of about 1 mV per 1149 N/m^2 gage (6 mV/psig). The entire transducer, including the bridge circuitry, was 1.27 cm (0.5 in.) long and 0.0889 cm (0.035 in.) thick with a diaphragm diameter of 0.635 cm (0.25 in.). The transducers were mounted on the surface of one rotor blade as shown schematically in figure 5. Originally there were upper and lower surface transducers at each station; however, the lower surface 30-percent-chord transducer failed

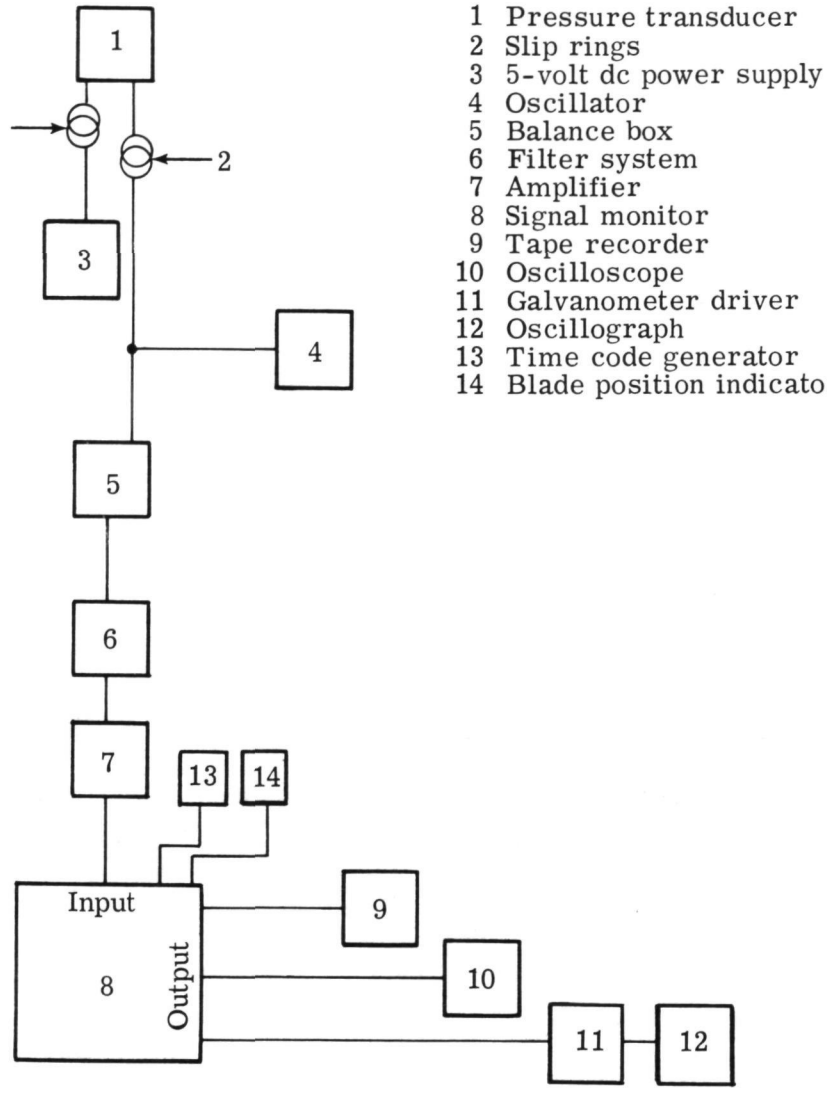

1 Pressure transducer
2 Slip rings
3 5-volt dc power supply
4 Oscillator
5 Balance box
6 Filter system
7 Amplifier
8 Signal monitor
9 Tape recorder
10 Oscilloscope
11 Galvanometer driver
12 Oscillograph
13 Time code generator
14 Blade position indicator

Figure 3.- Block diagram of blade pressure data acquisition system.

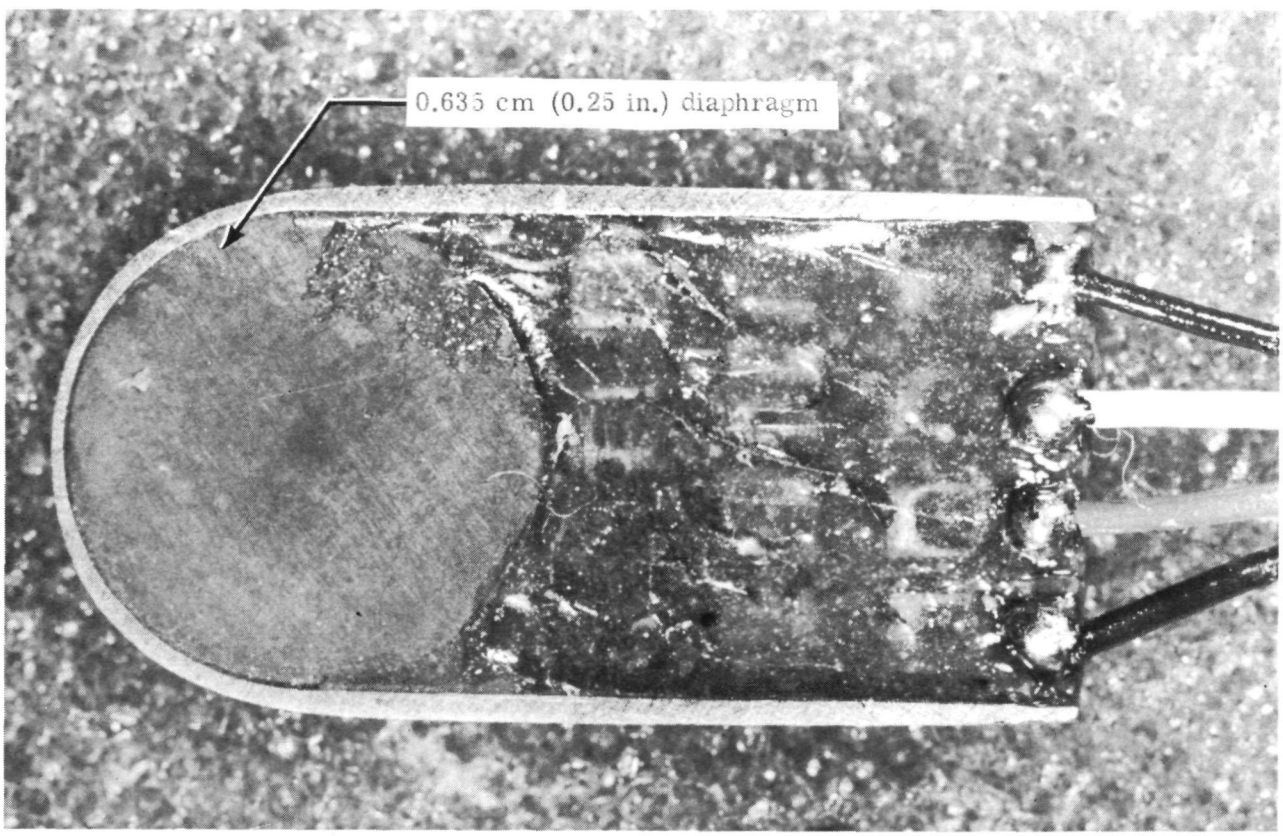

L-72-1546.1

Figure 4.- Photograph of surface of pressure transducer used for blade pressure measurements.

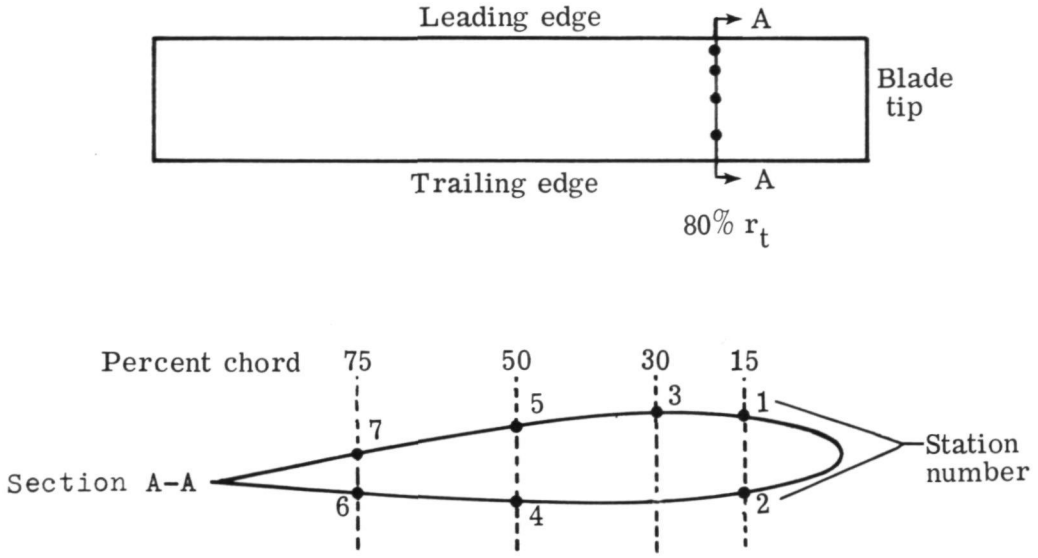

(a) Location of pressure transducers.

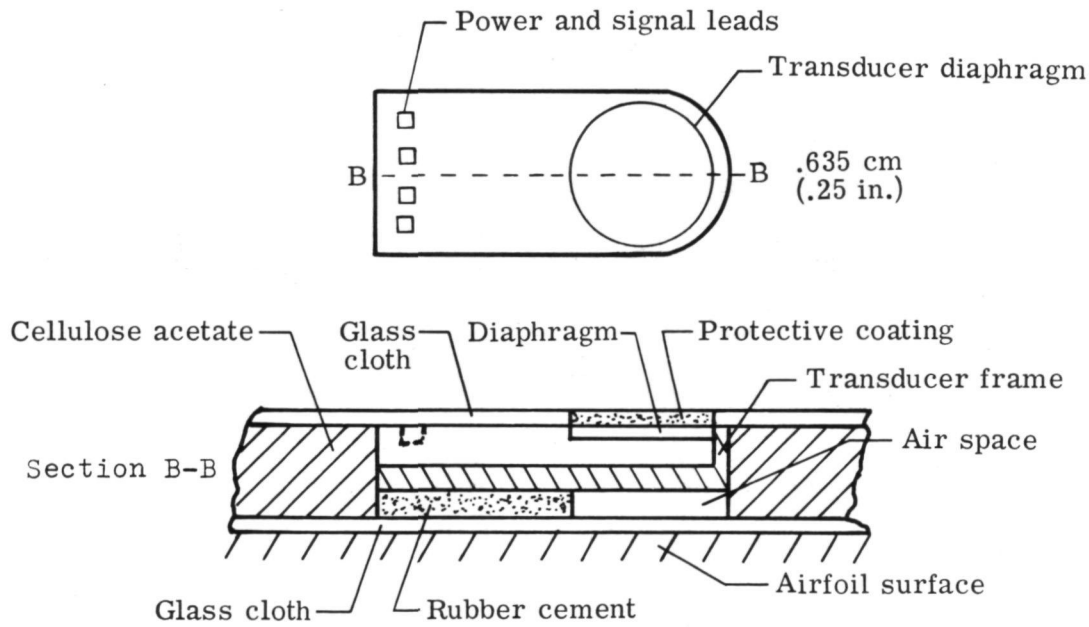

(b) Schematic of transducer mounting.

Figure 5.- Schematics of location and mounting of surface pressure transducers.

before data acquisition began. To relieve case strains which may have developed because of blade bending, care was taken to achieve a cantilevered mounting by not bonding the transducer under the diaphragm area.

Each pressure transducer was calibrated with a commercially available discrete frequency acoustic calibrator at a level of 62 N/m^2 gage (0.009 psig) rms and at a frequency of 250 Hz. The calibrations were performed twice daily several days prior to each test. The mean level of these calibrations was taken to be the nominal calibration level. In order to achieve a constant amplitude calibration, an audio oscillator was used to electronically simulate the mean level of the dynamic calibrations. This electrical calibration was introduced at the input to the balance box and recorded on FM magnetic tape as the transducer amplitude calibration.

Signal conditioners: The output of the pressure transducers was passed through slip rings to a balance box where offsets due to changes in temperature, atmospheric pressure, and variation of individual gage zero balance were nulled. The slip ring noise, always of concern in this type of experiment, was found to have a maximum overall rms level of 50 μV or 57.45 N/m^2 gage (0.0083 psig) based on the sensitivity of the pressure transducers. A typical time history and spectrum of the slip ring noise are shown in figure 6. From this figure, it is seen that the slip ring noise is concentrated below 60 Hz; but this is also the range where the aerodynamic pressures are of largest amplitude.

The balanced output was then amplified to obtain sufficient levels for FM recording on magnetic tape. Two different filters were also applied at this point. The first was a 10 000 Hz low-pass filter and the second was a dc blocking band-pass filter with a 10 000 Hz cutoff. The low-pass filter was used to measure the dc (uniform) pressures while the band-pass filter was used to measure the dynamic pressures. Both filters had essentially the same dynamic response, but the latter allowed amplification of the dynamic data without exceeding the FM recording limit. The frequency response of the blade surface pressure measuring system was found to be limited by the response of the transducers. Figure 7 shows the frequency response of the dynamic pressure measurement system in the dc blocking configuration. The 6 dB down point is at 10 000 Hz. Because of the transducer frequency response limit, all of the pressure data analysis was confined to 5000 Hz.

Recording equipment: All blade pressure data were multichannel, FM recorded on 1-inch magnetic tape at a speed of 152.4 cm/sec (60 ips). The carrier frequency was 108 000 Hz with a recording bandwidth of dc to 20 000 Hz.

Time-code generator: A standard IRIG A 10 000 Hz time code was recorded on a separate recorder channel. This time code provided time markers every 0.1 sec which were used to identify tape segments for digitizing the data.

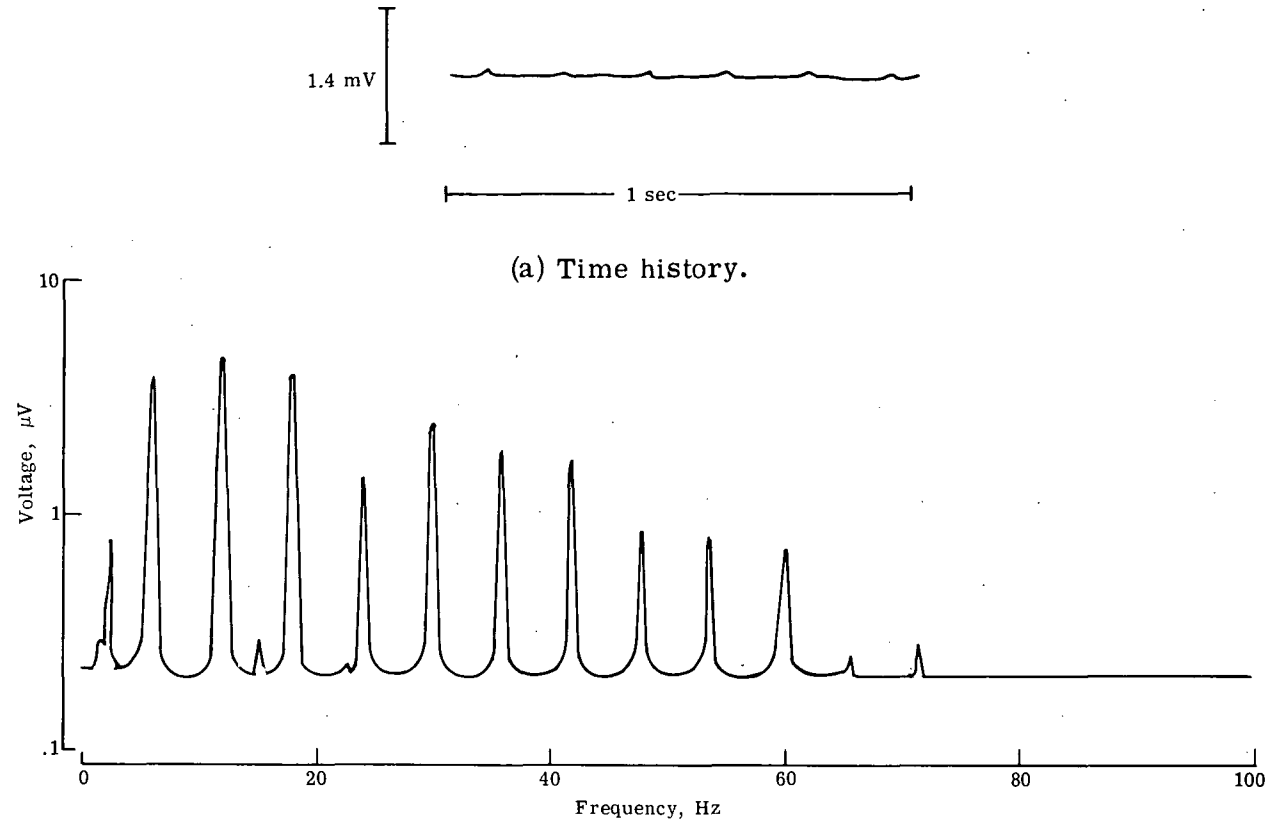

(a) Time history.

(b) Voltage spectrum.

Figure 6.- Typical slip ring noise.

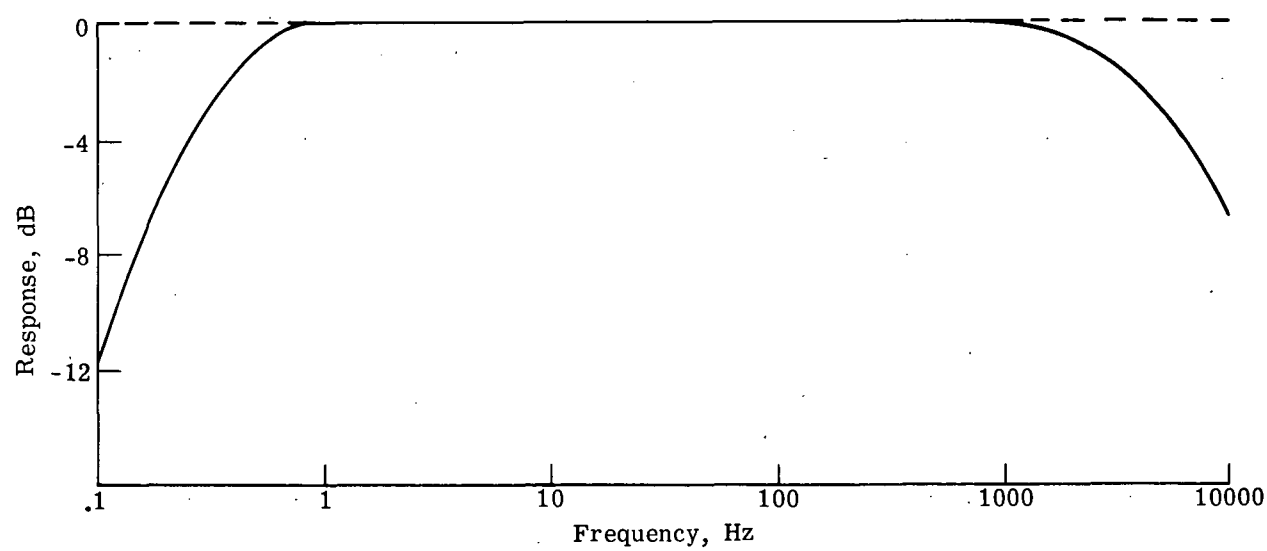

Figure 7.- Typical frequency response of blade pressure data acquisition system in the dc blocking configuration.

Position indicator: The azimuthal position of the instrumented blade was recorded four times per revolution by a blade pulse position indicator. The pulse was obtained from a voltage applied to a reed switch and capacitor circuit triggered every 90^{o} by a magnet attached to the rotor shaft.

Acoustic measurements.- Figure 8 shows a block diagram of acoustic data acquisition system. The microphones were commercially available, piezoelectric, ceramic type, having a frequency response flat within 3 dB over the frequency range of 12 Hz to 10 000 Hz. The signal outputs from both microphones were multichannel, FM recorded on magnetic tape. The frequency response of the complete measuring system was flat to within 3 dB from 12 Hz to 10 000 Hz. Figure 9 shows a typical frequency-response curve for the measuring system. The entire sound measurement system was calibrated in the field prior to and after each test. Calibrations were performed with a commercially available discrete frequency calibrator with a 1000 Hz sine-wave signal at a sound pressure level of 124 dB.

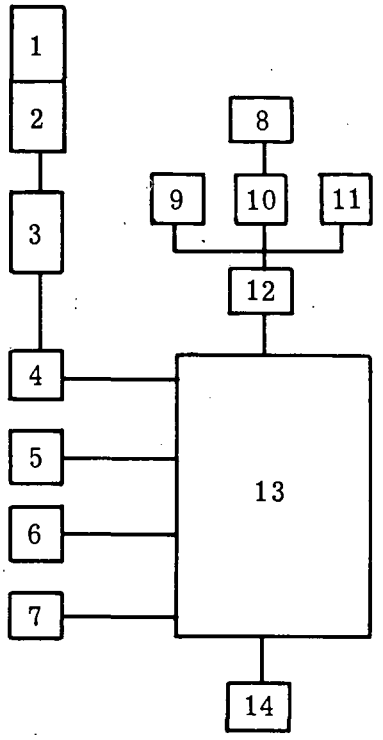

1 Microphone
2 Preamplifier
3 Booster amplifier
4 Sound level meter
5 10 000 Hz time code
6 Voice microphone
7 Blade azimuthal position indicator
8 Oscillograph
9 Oscilloscope
10 dc amplifier
11 Real time analyzer
12 Tape-recorder monitor switch
13 Tape recorder
14 110-volt power supply

Figure 8.- Block diagram of acoustic data acquisition system.

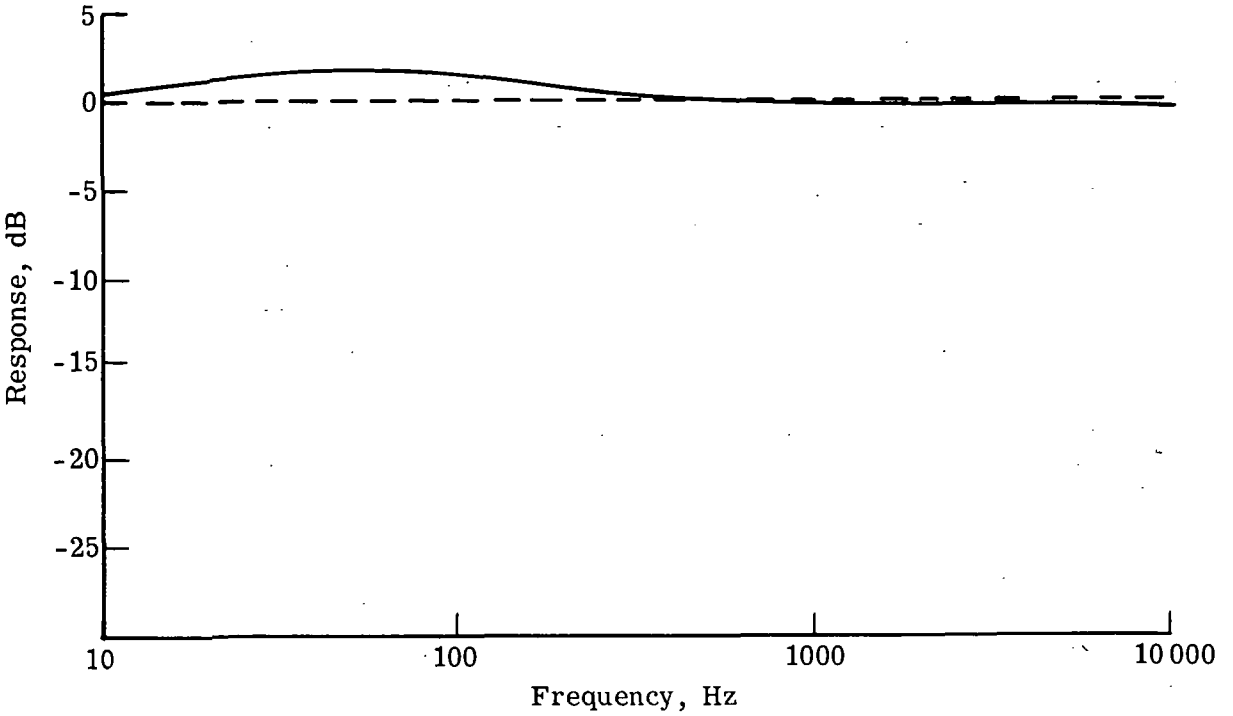

Figure 9.- Typical frequency-response curve for the entire acoustic data system.

Experimental Procedure

A regular check on all the measuring systems was performed before operation of the facility. In order to insure low ambient noise levels, the experiments were conducted during the predawn hours. Wind velocities during these tests did not exceed 2.24 m/sec (5 mph).

Table II lists the test conditions studied. Recording of the data was begun only after insuring that steady state was reached for each test condition. Each filter condition was used with two sets of amplification, the first with the maximum possible gain and the second with the next lowest gain setting. The latter case served as a precautionary measure in the event that the maximum gain case caused the data to exceed the voltage limit of the FM recording channel. The maximum allowable amplification for each test case was determined from oscilloscope monitors. In addition, a real-time narrow band analyzer was used to provide on-line displays of the pressure and acoustic spectra. After assuring that systems were operating properly, approximately 45 sec of blade pressure and acoustic data were recorded simultaneously for each test case.

TABLE II.- TEST CONDITIONS

Condition	rpm	Blade passage frequency, Hz	Mach number, M_e, at 80-percent span	Lift, L_F		Torque, $D_F r_e$		Angle of attack, β, at 80-percent span, deg
				N	lb	N-m	lb-ft	
1	225	15.0	0.30	14 612	3 285	6 345	4 680	10.23
2	225	15.0	.30	22 743	5 113	15 253	11 250	15.15
3	261	17.4	.35	31 714	7 130	22 300	16 450	15.40
4	263	17.5	.36	6 792	1 527	3 661	2 700	4.78
5	265	17.7	.36	12 530	2 817	5 626	4 150	7.40
6	355	23.7	.48	18 553	4 171	7 864	5 800	6.45
7	355	23.7	.48	44 613	10 030	23 726	17 500	12.03

DATA REDUCTION AND ANALYSIS

Oscillograph records of all blade pressure and acoustic channels were reviewed following recording of the test data; data which exceeded the recording limit were eliminated from further consideration. Test conditions which provided the most intense rotational noise were chosen for further analysis from the remaining data. A 20-second period of data from each of these conditions was chosen for analog-to-digital conversion. Initially the data were digitized at a rate in excess of 10 000 samples per second to provide blade loading coefficients to 5000 Hz. Examination of these data indicated that because of the calm inflow environment (hover with a 2.24 m/sec (5 mph) wind) no discrete blade pressure harmonics were visible beyond 1000 Hz. More severe operating conditions would have produced more intense high-frequency discrete blade pressures. To allow more efficient use of the computerized Fourier transform routines (ref. 18), the data were redigitized at a rate of 4000 samples per second. Antialiasing low-pass filters with a cutoff frequency of 2000 Hz were applied to the data before digitizing.

The primary input parameters for the rotational-noise prediction computer program – fluctuating blade loading spectra – were obtained by first digitizing the blade pressure data and then using a Fourier transform computer program (ref. 18) to obtain pressure spectra. These complex spectra, produced for each of the seven absolute pressure transducers (fig. 5), were then summed for each pair of upper and lower surface transducers to give a differential pressure spectrum at each chordwise station. After normalizing their amplitudes by the uniform pressure the differential spectra (now loading spectra) were then either used directly in the rotational-noise prediction computer program or they were chordwise integrated and supplied to the computer program for noise prediction. The integrated spectrum was obtained by employing a spline interpolation (ref. 19) routine and a combined Simpson-Newton 3/8 rule integration procedure (ref. 20). The uniform pressure was first obtained by measuring the dc shift of each transducer

from its zero position on the oscilloscope records. Later the methods of references 21 to 24 were used because changes occurred in the transducer electronic balance.

Although the prediction program required only the blade loading harmonics (periodic data), fluctuating blade pressures, by nature, contain random components. To increase the accuracy of the estimate of the blade load data, that is, to increase the statistical degrees of freedom, spectrum averaging was employed. Table III indicates the statistical degrees of freedom and the 90-percent confidence limits associated with each test case.

TABLE III.- NINETY-PERCENT CONFIDENCE LIMITS OF DATA ANALYSIS BY FAST FOURIER TRANSFORM PROGRAM

Condition	rpm	Analysis bandwidth	Number of averages	Degrees of freedom	Error band, dB
1	225	1.25	25	50	1.6 to -1.8
2	225	1.25	25	50	1.6 to -1.3
3	261	1.09	21	42	1.4 to -1.8
4	263	1.10	22	44	1.4 to -1.8
5	265	1.10	22	44	1.4 to -1.8
6	355	1.48	29	58	1.3 to -1.5
7	355	1.48	29	58	1.3 to -1.5

The acoustic data, which were measured simultaneously with the fluctuating blade pressures, were also spectrum analyzed. Thus, it was possible to directly compare the predicted and measured rotational noise. The statistical degrees of freedom and the 90-percent confidence limits for the measured acoustic spectra are also given in table III.

GENERALIZED LOADING RESULTS AND DISCUSSION

Prior to calculating the rotational noise, the loading data from the seven test conditions listed in table II were studied to identify trends and to collapse the data where possible. This section reports the results of that effort.

Time Histories of Blade Pressure Data

A total of seven transducers were used to measure the gage pressure on the upper and lower blade surfaces at four chordwise stations at 80-percent span. A pair of transducers was used at the 15-, 50-, and 75-percent chord stations; but because the lower surface transducer failed, only a single transducer was used at the 30-percent chord station

(see fig. 5). Figure 10 shows typical pressure time histories from the upper and lower surface gages at 15- and 50-percent chord. These data (from condition 6, table II) show the fundamental 1/rev oscillation with higher frequency oscillations superimposed. The periodic nature of these data is indicative of steady but nonuniform blade pressures. It can be seen that the upper and lower surface pressure peak-to-peak amplitudes are nearly equal at each chord station. From figure 10 it can be seen that the percentage of high-frequency blade loads increases from the 15-percent to the 50-percent station; however, the peak-to-peak amplitude is less at 50-percent chord than at 15-percent chord. It can

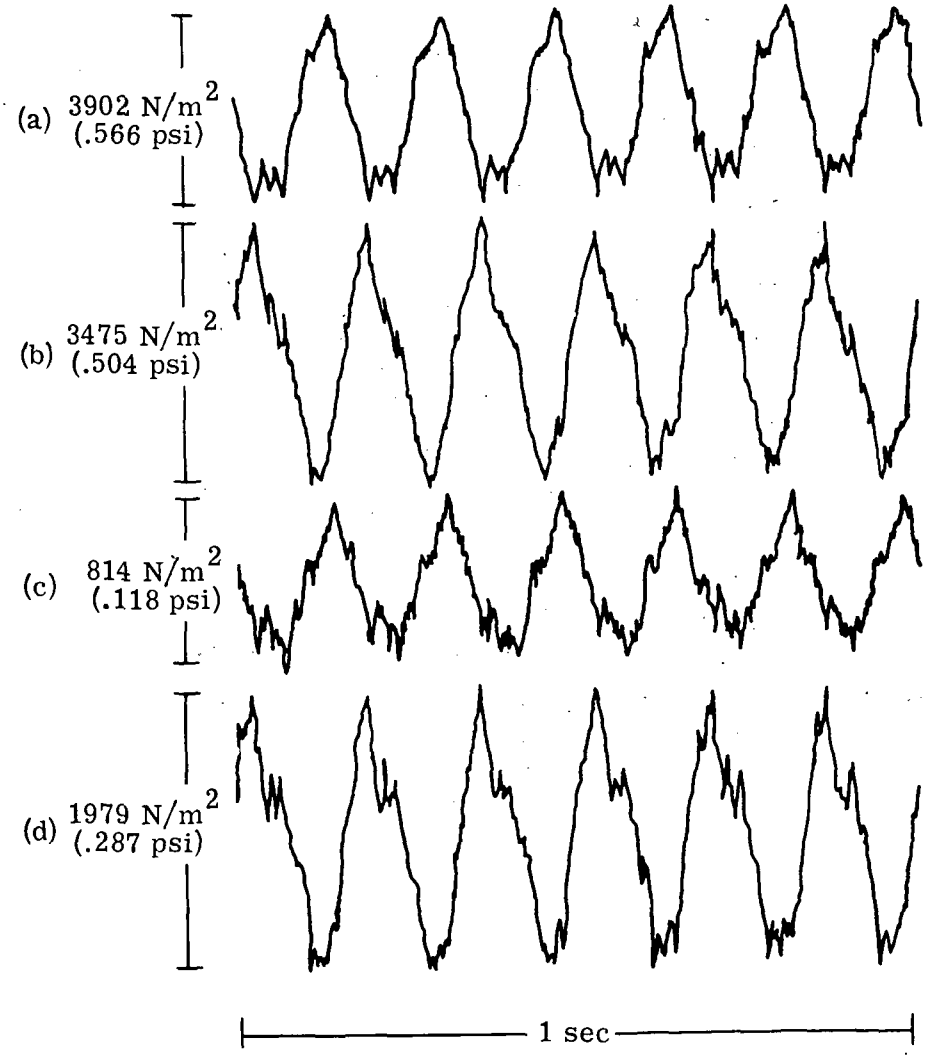

Figure 10.- Typical gage pressure time histories from upper and lower surface transducers at (a) 15-percent chord, upper surface, (b) 15-percent chord, lower surface, (c) 50-percent chord, upper surface, and (d) 50-percent chord, lower surface.

also be seen that the upper and lower surface pressures at each station are approximately 180^{o} out of phase.

Root-Mean-Square Levels of Blade Pressure Data

Table IV(a) shows the rms gage pressures at each of the seven stations and the mean lift coefficients $\overline{C}_L$ for all the test conditions. Again it is observed that except for stations 4 and 5 the upper and lower surface rms pressures at each chord station are nearly equal with a general decrease in level from leading to trailing edge. These data are plotted in figure 11(a). Except for conditions 6 and 7, the rms levels remain nearly constant at each station for all $\overline{C}_L$. For comparison the maximum overall rms system noise level is also shown in figure 11(a).

TABLE IV.- ROOT-MEAN-SQUARE GAGE PRESSURES AND MEAN LIFT COEFFICIENTS

(a) Absolute values

Condition	$\overline{C}_L$	Root-mean-square gage pressure, N/m^2, at –						
		Station 1	Station 2	Station 3	Station 4	Station 5	Station 6	Station 7
1	0.619	903	641	268	813	220	199	186
2	.938	827	620	227	510	220	206	275
3	.991	923	744	275	751	241	241	337
4	.210	717	648	289	434	172	158	151
5	.383	779	620	268	496	172	193	165
6	.317	1048	889	406	586	227	227	262
7	.759	1399	1165	482	854	255	372	351
Condition	$\overline{C}_L$	Root-mean-square gage pressure, psi, at –						
		Station 1	Station 2	Station 3	Station 4	Station 5	Station 6	Station 7
1	0.619	0.131	0.093	0.039	0.118	0.032	0.029	0.027
2	.938	.120	.090	.033	.074	.032	.030	.040
3	.991	.134	.108	.040	.109	.035	.035	.049
4	.210	.104	.094	.042	.063	.025	.023	.022
5	.383	.113	.090	.039	.072	.025	.028	.024
6	.317	.152	.129	.059	.085	.033	.033	.033
7	.759	.203	.164	.070	.124	.037	.054	.057

(b) Percent of uniform load

Condition	$\overline{C}_L$	Root-mean-square gage pressure, % of uniform load, at –						
		Station 1	Station 2	Station 3	Station 4	Station 5	Station 6	Station 7
1	0.619	12.7	98.9	5.4	368.7	4.5	126.1	15.9
2	.938	8.5	28.7	3.5	107.2	5.7	41.1	17.7
3	.991	9.0	29.9	4.1	126.7	6.0	43.2	20.8
4	.210	16.8	42.9	8.8	40.4	8.3	62.2	20.7
5	.383	14.0	138.5	6.6	75.0	6.8	311.1	17.6
6	.317	20.4	115.2	10.7	73.9	9.5	165.0	30.2
7	.759	16.5	74.5	8.4	523.6	7.3	110.2	25.6

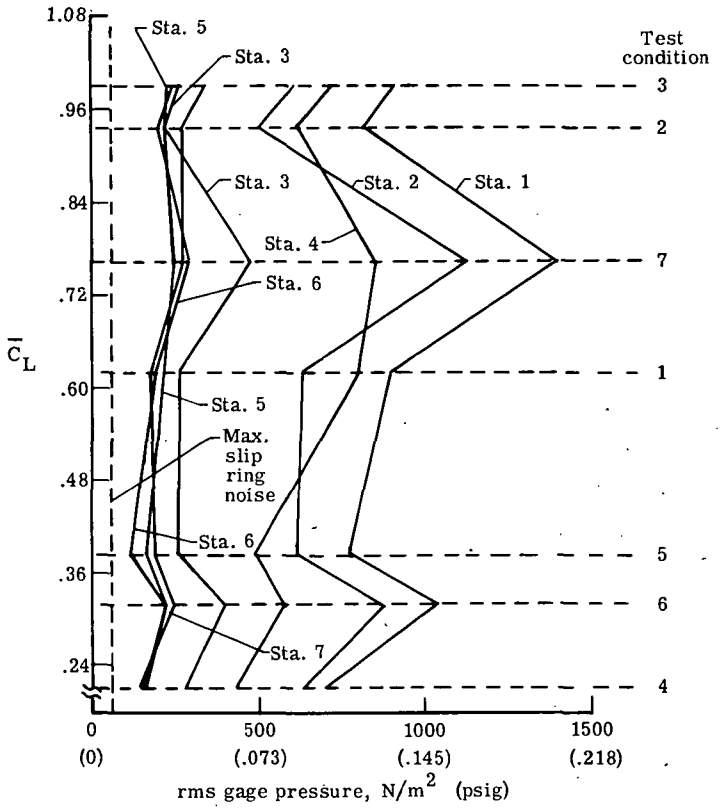

(a) rms gage pressure for all stations.

Figure 11.- Mean lift coefficient $\bar{C}_L$ plotted against rms gage pressures and rms loading coefficients $\alpha_{rms,g}$. (Test conditions refer to table II and station numbers refer to fig. 5.)

In table IV(b) and figures 11(b) and 11(c) the rms gage blade loading coefficients, $\alpha_{rms,g} = \frac{P_{rms,g}}{P_{0,g}}$, are shown for all the test conditions. The upper surface coefficients (fig. 11(b)) maintain nearly the same shape as the upper surface gage pressures (fig. 11(a)); but now, with the exception of station 1, the level of the coefficients increases going from the leading edge to the trailing edge. This is caused by the small normalizing uniform pressures, $P_{0,g}$, at the trailing portion of the airfoil as compared with $P_{0,g}$ at the leading portion of the airfoil. This effect will be seen later in both the differential blade loading coefficients and in the rotational noise calculations. The lower surface blade loading coefficients (fig. 11(c)) behave much more erratically than the lower surface pressures (fig. 11(a)) or than the upper surface coefficients (fig. 11(b)). Their distorted shapes are caused by very small and erratic uniform blade pressures on the lower surface.

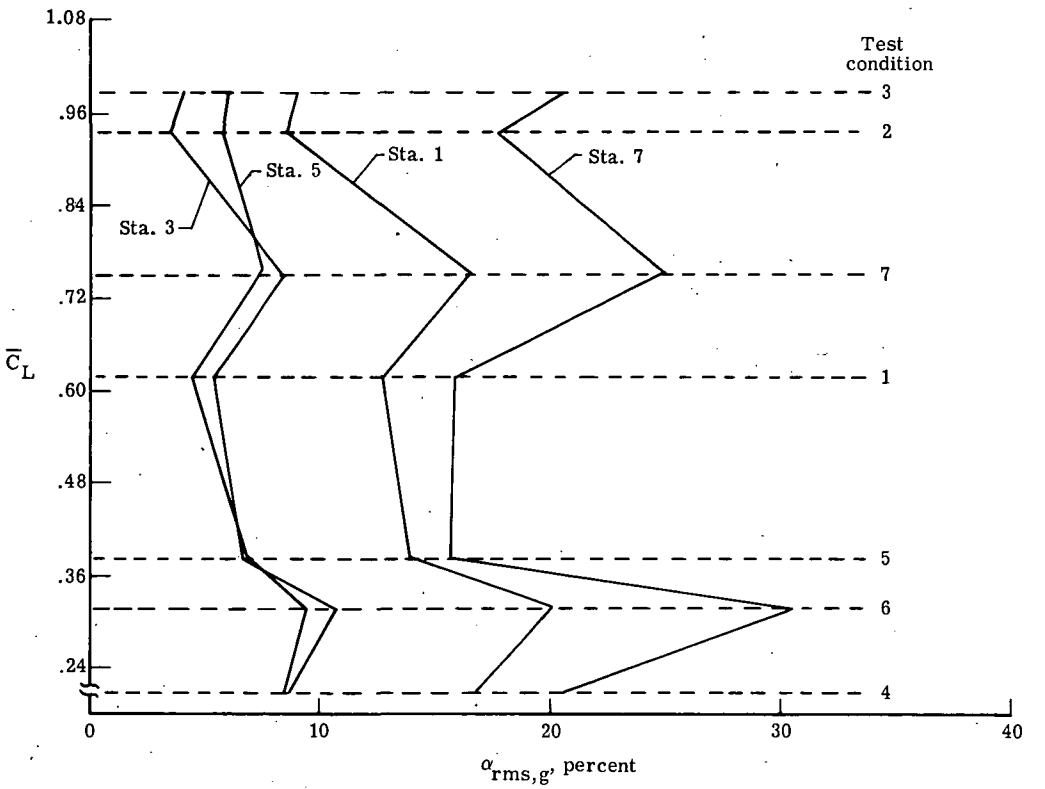

(b) $\alpha_{rms,g} = P_{rms,g}/P_{0,g}$ for each upper surface station.

Figure 11.- Continued.

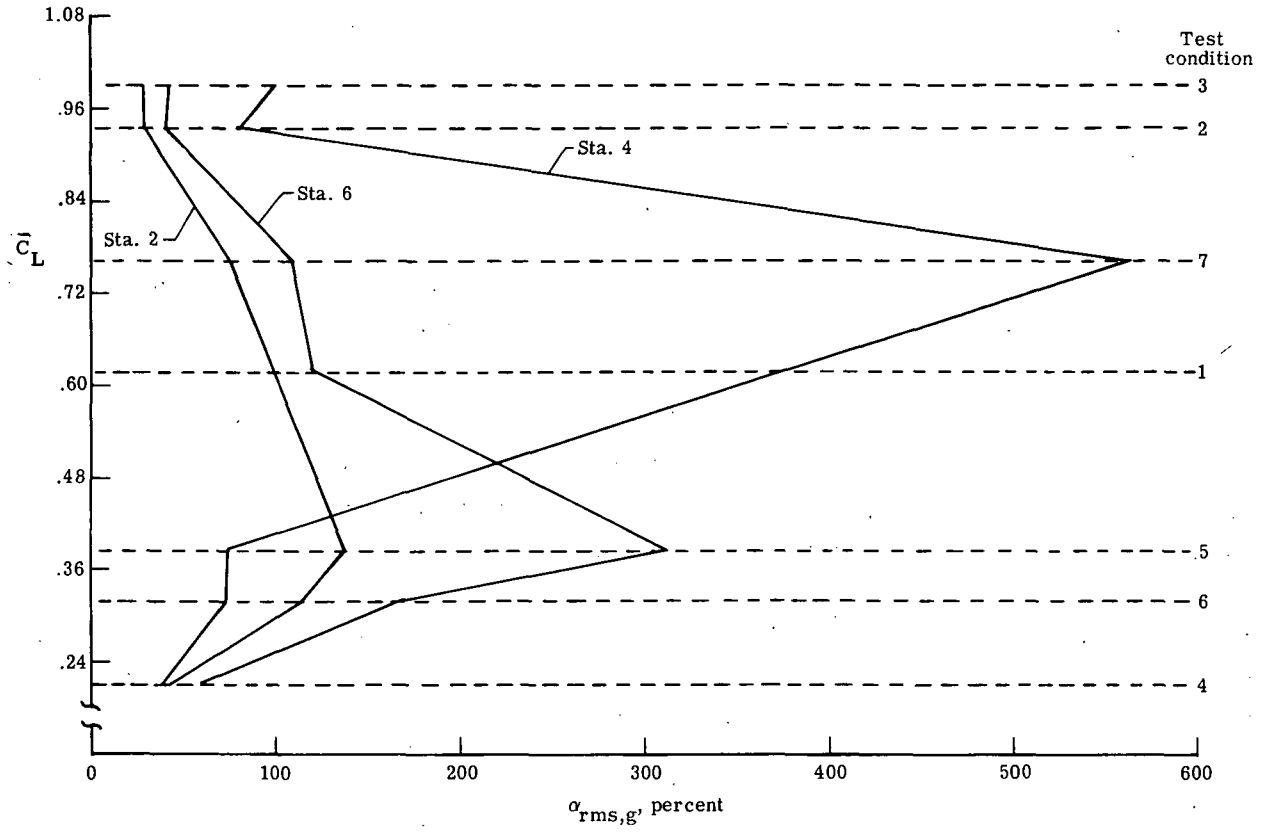

(c) $\alpha_{rms,g} = P_{rms,g}/P_{0,g}$ at each lower surface station.

Figure 11.- Concluded.

Blade Pressure Spectra

Typical pressure amplitude spectra from data measured at stations 1, 2, 5, and 4 are shown in figures 12(a), 12(b), 12(c), and 12(d), respectively. By comparing figures 12(a) and 12(b) and figures 12(c) and 12(d), it can be seen that the upper and lower surface spectra are quite similar at each chord station. About 50 blade loading harmonics are evident in figures 12(a) and 12(b) through about 300 Hz. Beyond this point a transition to a broadband spectrum occurs, although there seem to be intermittent areas of discrete data at these higher frequencies. The cause of these tones is not known.

Although not obvious from figure 12, it will be shown in connection with figure 15 that the blade pressures at the 50- and 75-percent chord stations generally tended to have less discrete content than did the pressures at the 15- and 30-percent chord stations. This increased randomness over the aft portion of the chord may be caused by increased boundary-layer turbulence in that area. In these tests, no blade pressure harmonics were ever observed above 1000 Hz. However, tests conducted with more severe inflow conditions may produce blade pressure harmonics up to or beyond 1000 Hz.

System Noise

In order to determine the pressure data system electrical noise, the pressure transducers were replaced by dummy bridges while leaving the remainder of the signal conditioning intact. The rotor system was then operated over the range of conditions shown in table II. The pressure data system output included both the slip ring and signal conditioning noise. Figure 13(a) to 13(d) show the typical pressure equivalent system electronic noise spectra for the data from stations 1, 2, 5, and 4. It can be seen in this figure that the system noise is concentrated below 60 Hz. The harmonic separation is equal to the shaft frequency and the harmonic levels are less than 11.6 N/m^2 gage (0.00166 psig). Comparison of figures 12 and 13 shows that a minimum signal to noise ratio of about 10 dB (a factor of 3) is maintained for the 15-percent chord transducer at frequencies below 60 Hz. Above 60 Hz the signal-to-noise ratio exceeds 20 dB. For the 50-percent chord transducer the signal-to-noise ratio is less than 10 dB at some of the harmonics below 60 Hz. Above 60 Hz the signal-to-noise ratio exceeds 20 dB. The signal-to-noise ratio at the 30- and 75-percent chord stations was similar to that at the 15- and 50-percent chord stations, respectively. These signal-to-noise ratios were judged to be acceptable for these tests.

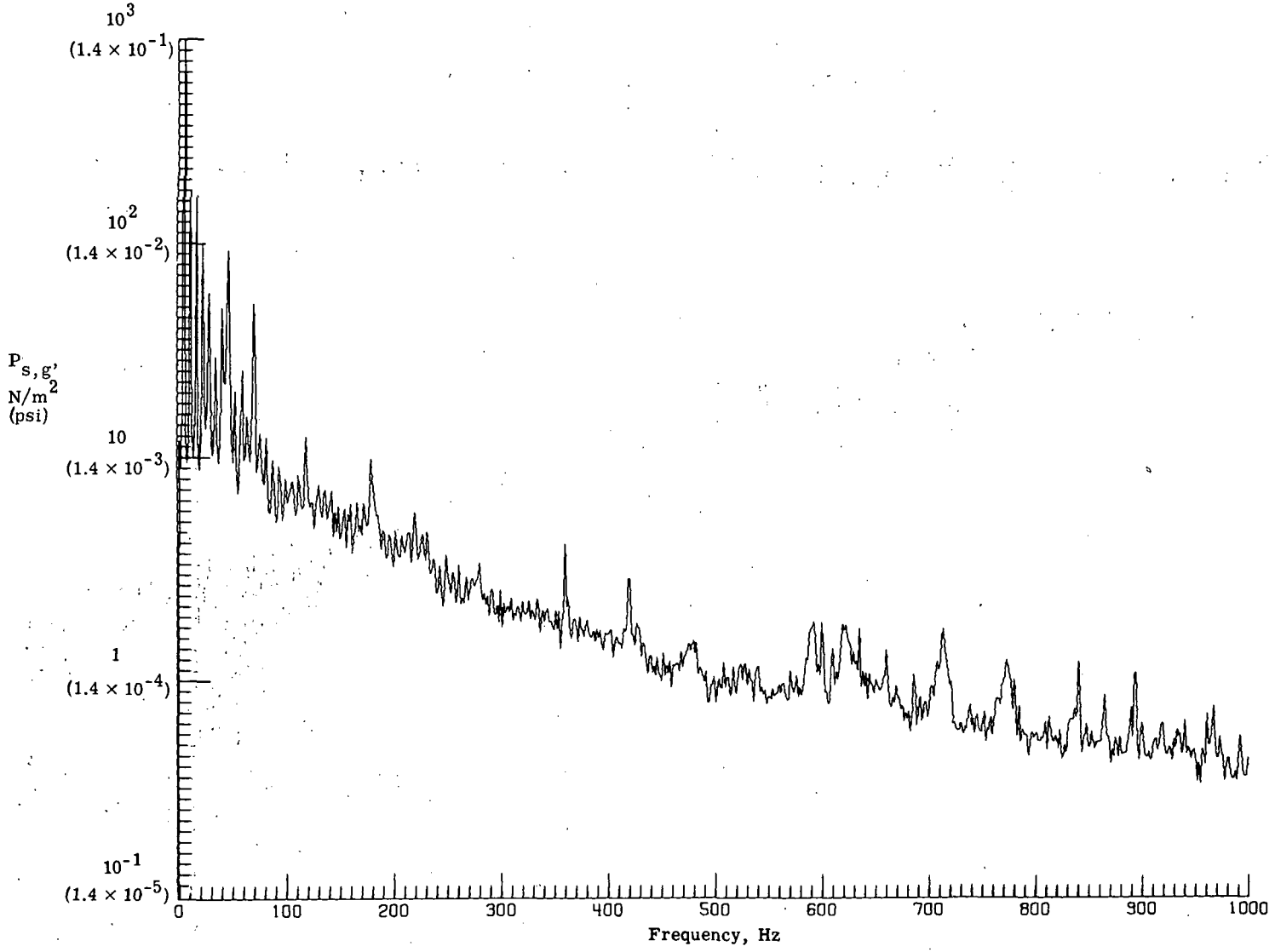

(a) 15-percent chord, upper surface.

Figure 12.- Typical surface pressure spectra.

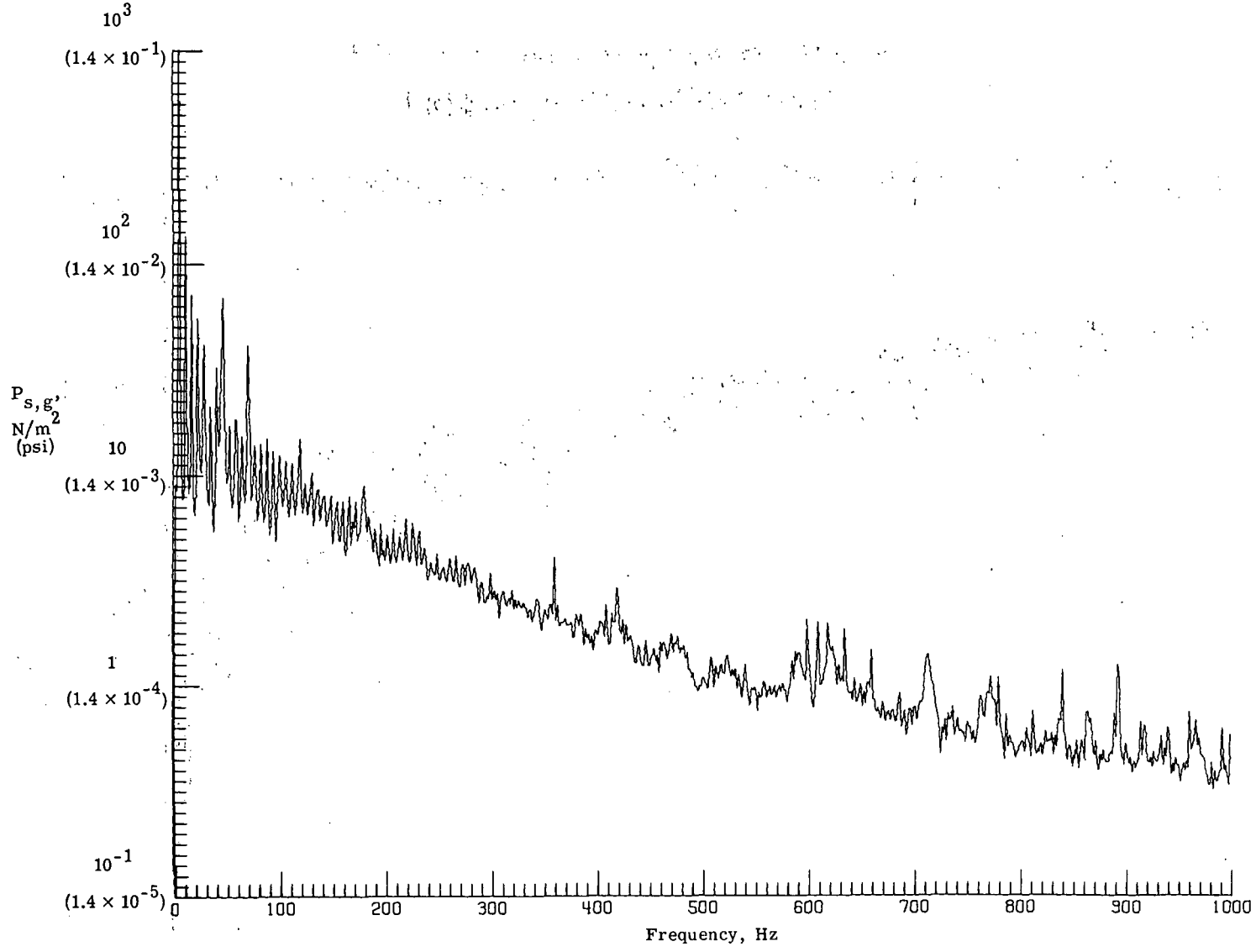

(b) 15-percent chord, lower surface.

Figure 12.- Continued.

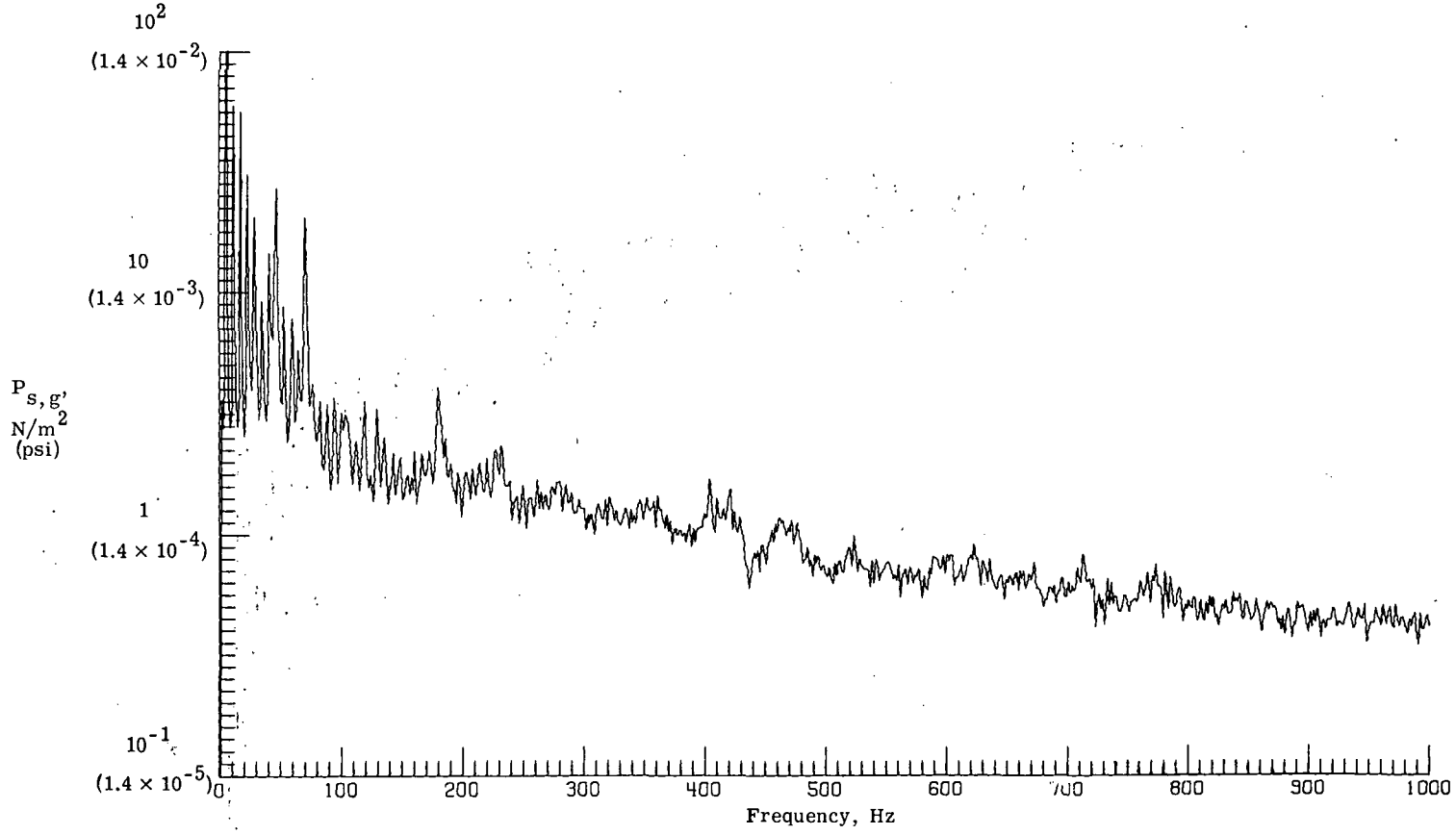

(c) 50-percent chord, upper surface.

Figure 12.- Continued.

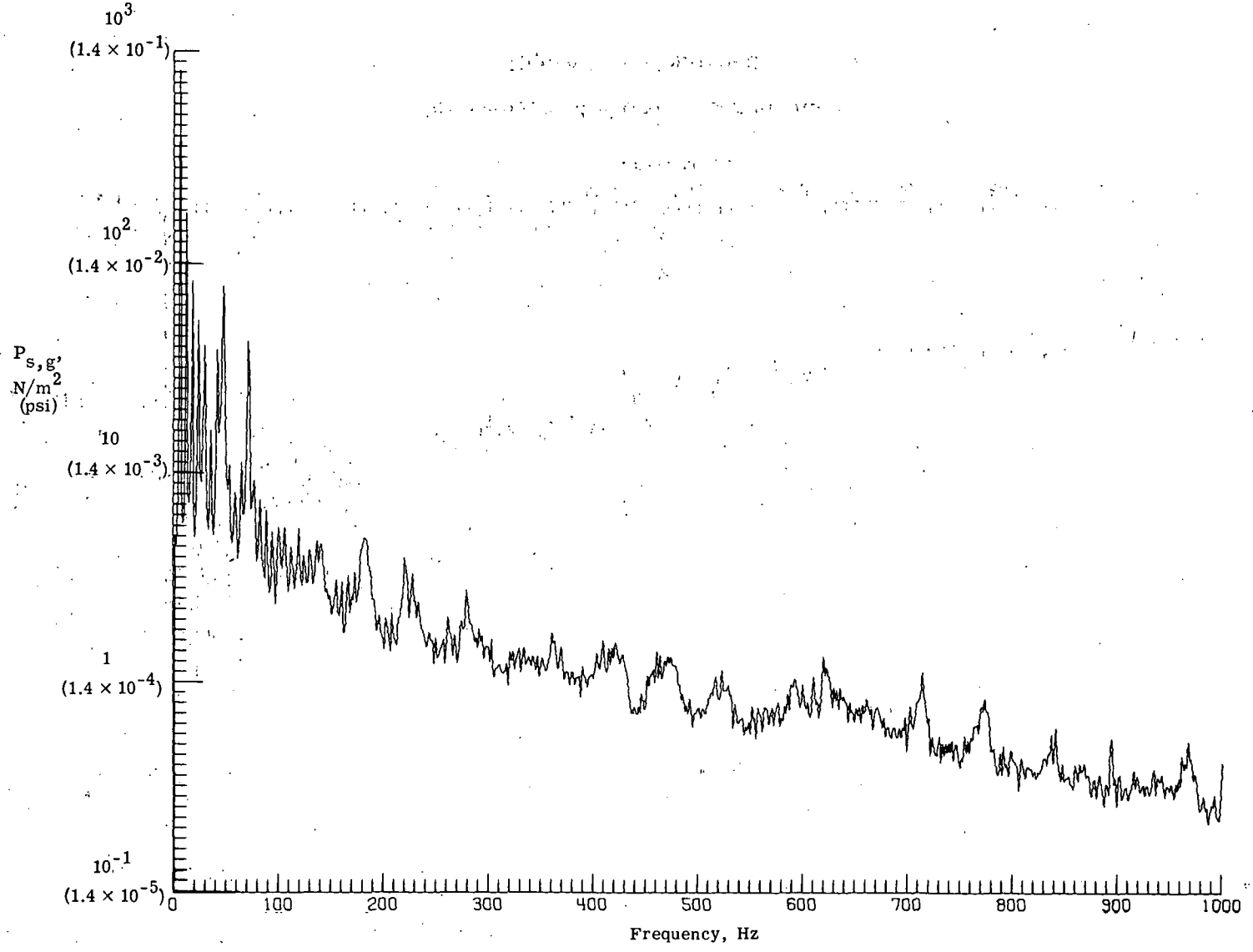

(d) 50-percent chord, lower surface.

Figure 12.- Concluded.

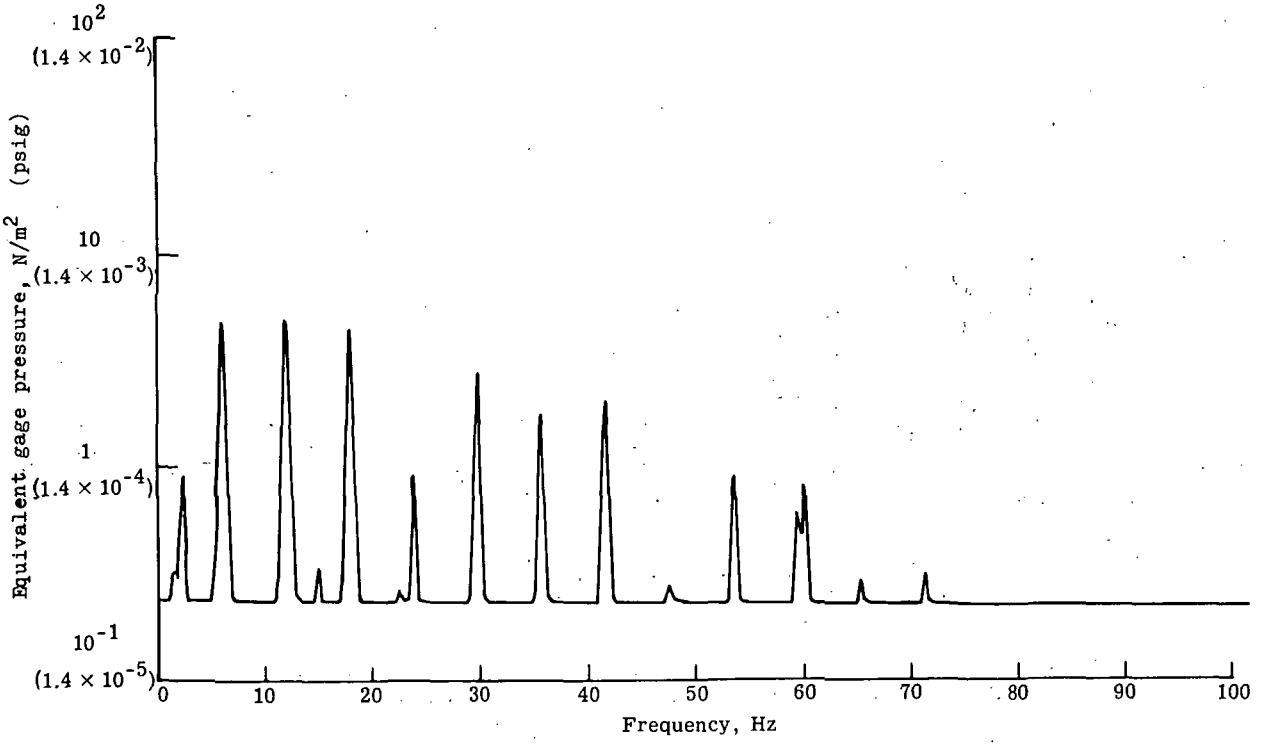

(a) 15-percent chord, upper surface.

Figure 13.- Typical pressure equivalent system electronic noise spectra for stations 1, 2, 5, and 4.

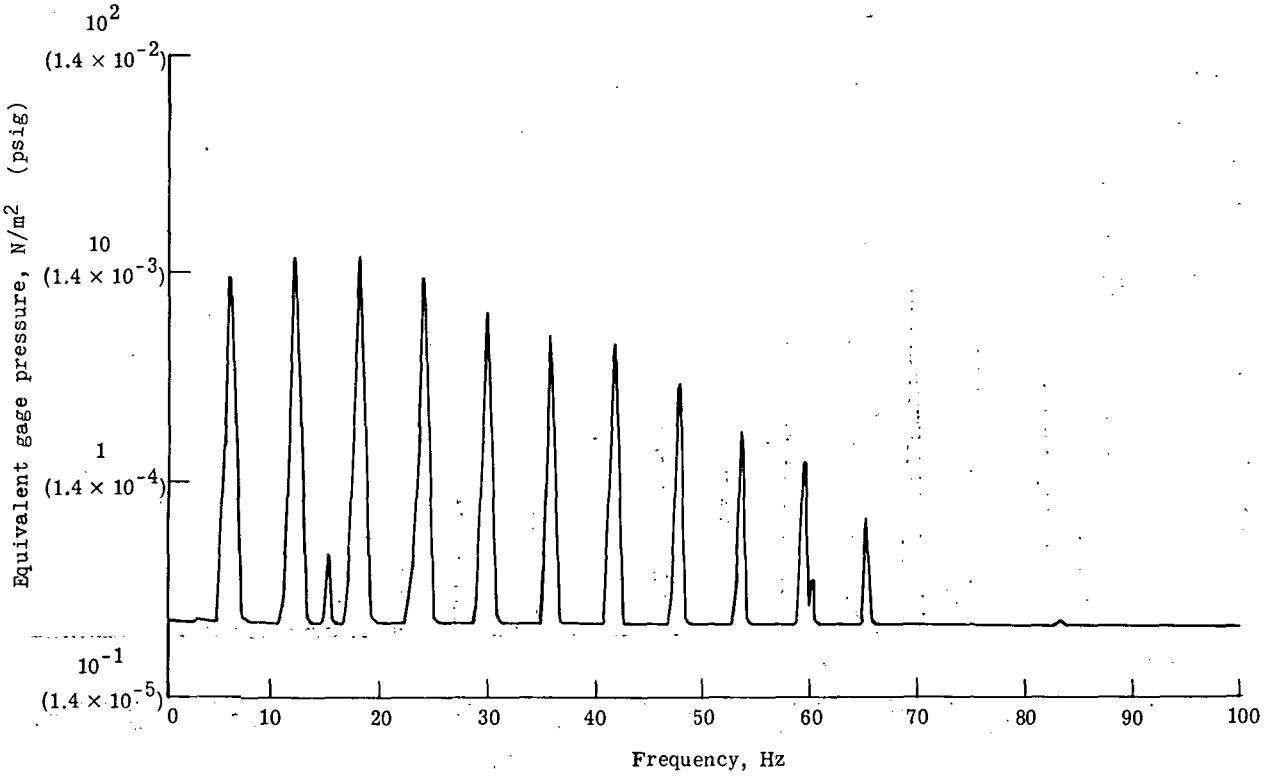

(b) 15-percent chord, lower surface.

Figure 13.- Continued.

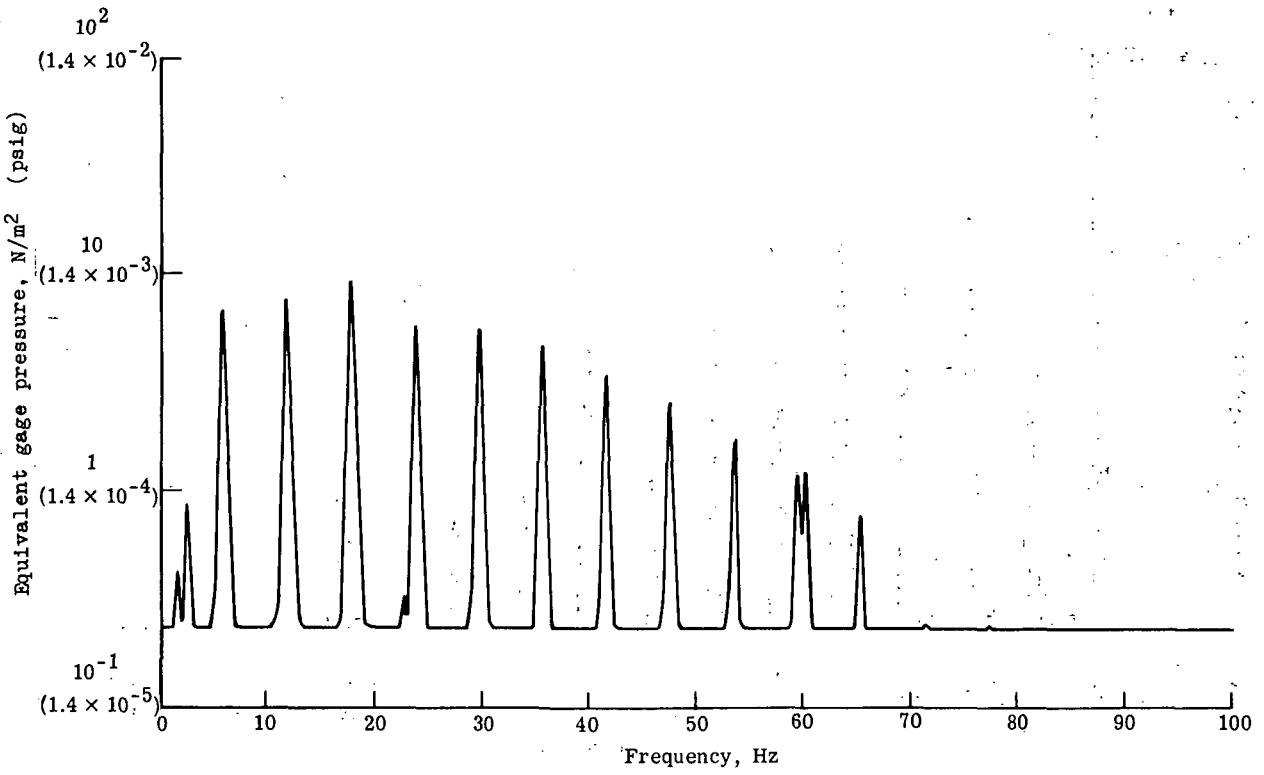

(c) 50-percent chord, upper surface.

Figure 13.- Continued.

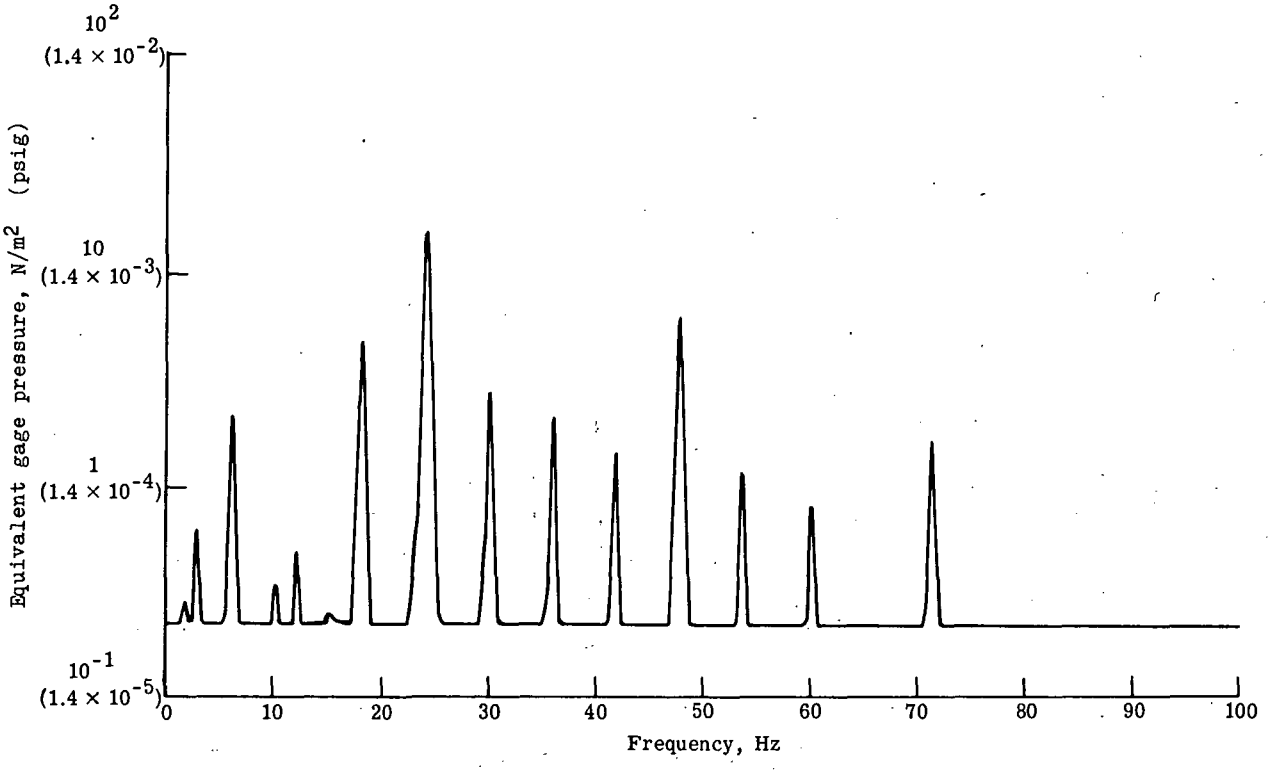

(d) 50-percent chord, lower surface.

Figure 13.- Concluded.

Comparison of Measured Blade Pressures and Acoustic Spectra

The measured far-field acoustic spectrum generated by the blade pressures shown in figures 12(a) to 12(d) is presented in figure 14. Comparison of the pressure and acoustic spectral characteristics indicates some similarity between the spectra. The acoustic spectrum shows one acoustic harmonic for every four blade loading harmonics. This four to one correspondence is caused by the four blades on the rotor. The transition region where the discrete spectrum begins to become broadband in both the blade loading and acoustic spectra occurs between 300 Hz and 400 Hz. In these tests the discrete spectrum rarely extended beyond 500 Hz in either the pressure or acoustic data.

The far-field acoustic spectrum amplitude decreases more slowly in amplitude than the loading spectrum. This is caused by the fact that each sound harmonic is generated by a multiplicity of blade loading harmonics (see section entitled "Rotor Rotational Noise Theory").

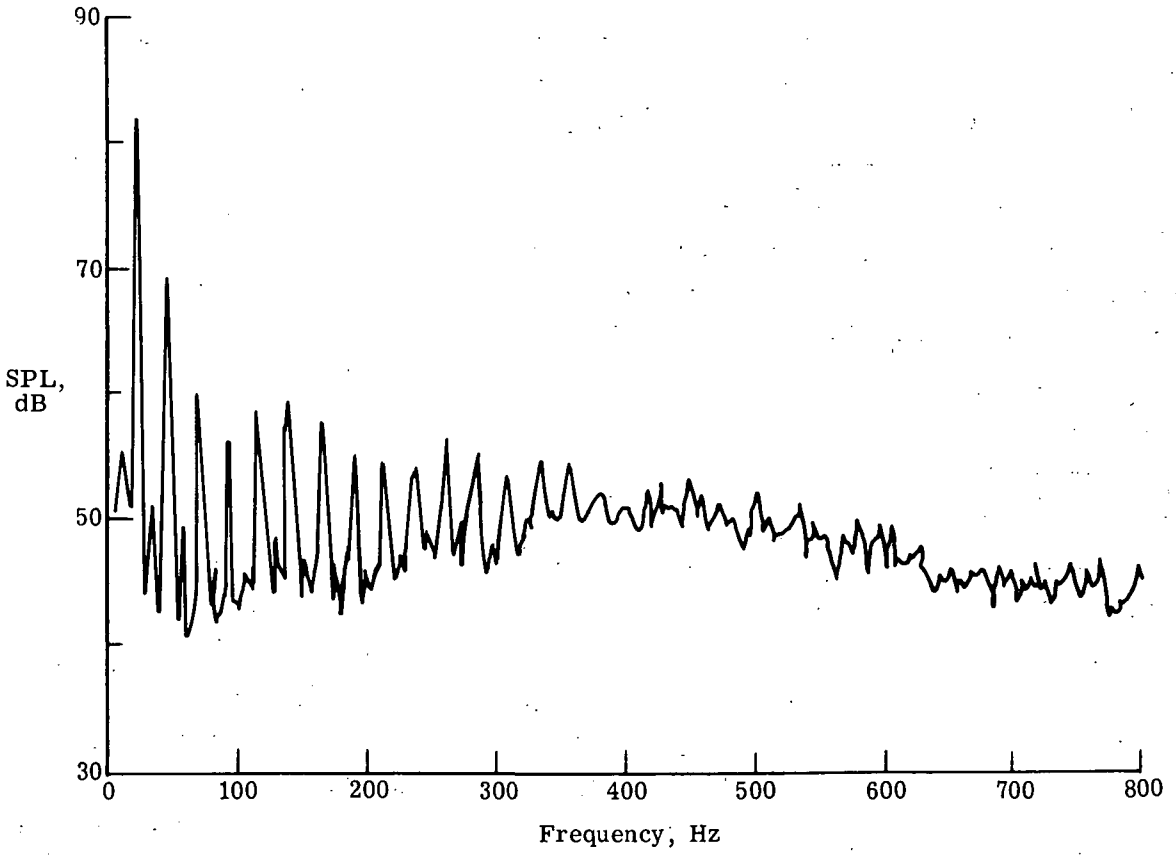

Figure 14.- Measured acoustic spectrum at microphone position 1 (see fig. 2). Thrust, 18 554 N (4171 lb); $\bar{C}_L$ = 0.317; rpm, 355.

Differential Blade Loading Spectra

Differential loading spectra at each station were obtained by performing a complex addition of the upper and lower surface gage pressure spectra and then normalizing by the differential uniform pressure. (Note: Hereinafter, all blade loading coefficients and pressures are based on gage pressures; therefore, the subscript g will be dropped.) At the 30-percent chord station where only an upper surface pressure transducer was used, the differential coefficients were approximated by doubling the amplitude of the upper surface blade pressure. This is believed reasonable because the upper and lower surface pressures are comparable in magnitude, but the upper surface uniform pressure is much greater than the lower surface uniform pressure. Hence, this doubling process approximates quite closely the realistic values of the blade pressure coefficients $\alpha_{s,diff}$.

In order to characterize the differential blade loading coefficients $\alpha_{s,diff}$ spectra obtained at each condition listed in table II were superimposed on the same plot for each chordwise station. The results are shown in figure 15. The bands from the 15- and 30-percent chord stations are very similar in level and shape (compare figs. 15(a) and 15(b)). At these two stations, the levels $\alpha_{s,diff}$ ranged from 65 percent at low frequencies (at the 15-percent chord station excluding 0 Hz where $\alpha_{s,diff} = 1$) to 0.003 percent at high frequencies (the lowest level at the 30-percent station). The spectrum fall-off rate ranges from 7 to 10 dB per octave (beginning with the first harmonic) throughout the entire spectrum. This fall-off rate is considerably less than the 15 dB per octave fall-off rate suggested in references 3 and 6 but agrees well with the 7 dB per octave fall-off rate, over the first 30 harmonics, reported in reference 25. The maximum level of the first harmonic is 65 and 25 percent of the differential uniform pressure $P_{0,diff}$ for the 15- and 30-percent chord stations, respectively.

Figures 15(c) and 15(d), taken from 50- and 75-percent chord, respectively, show a more rapid transition to broadband loads and larger levels in the high-frequency portion of the spectrum. However, the level of the first harmonic remains nearly the same as at the forward chord stations.

The reason for the increase in the high frequency spectrum levels at the trailing stations (when compared with the leading stations) can be understood from figure 16. This figure shows typical differential blade pressure $\left(P_{s,diff} = \alpha_{s,diff} \times P_{0,diff}\right)$ spectra from 15- and 75-percent chord. Although the levels of the low-frequency harmonics are less at 75-percent chord than at 15-percent chord, the high-frequency broadband pressures are higher in level at the 75-percent chord position. Also, the $P_{0,diff}$ at 75-percent chord is 17 percent of the $P_{0,diff}$ at 15-percent chord. These combined effects result in much higher blade loading coefficients $\alpha_{s,diff}$ at the aft chord positions, especially at high frequencies. As will be shown later, the low fall-off rates, the quick transition to broadband loads, and the high levels at 50- and 75-percent chord have a direct effect in the rotational noise calculations.

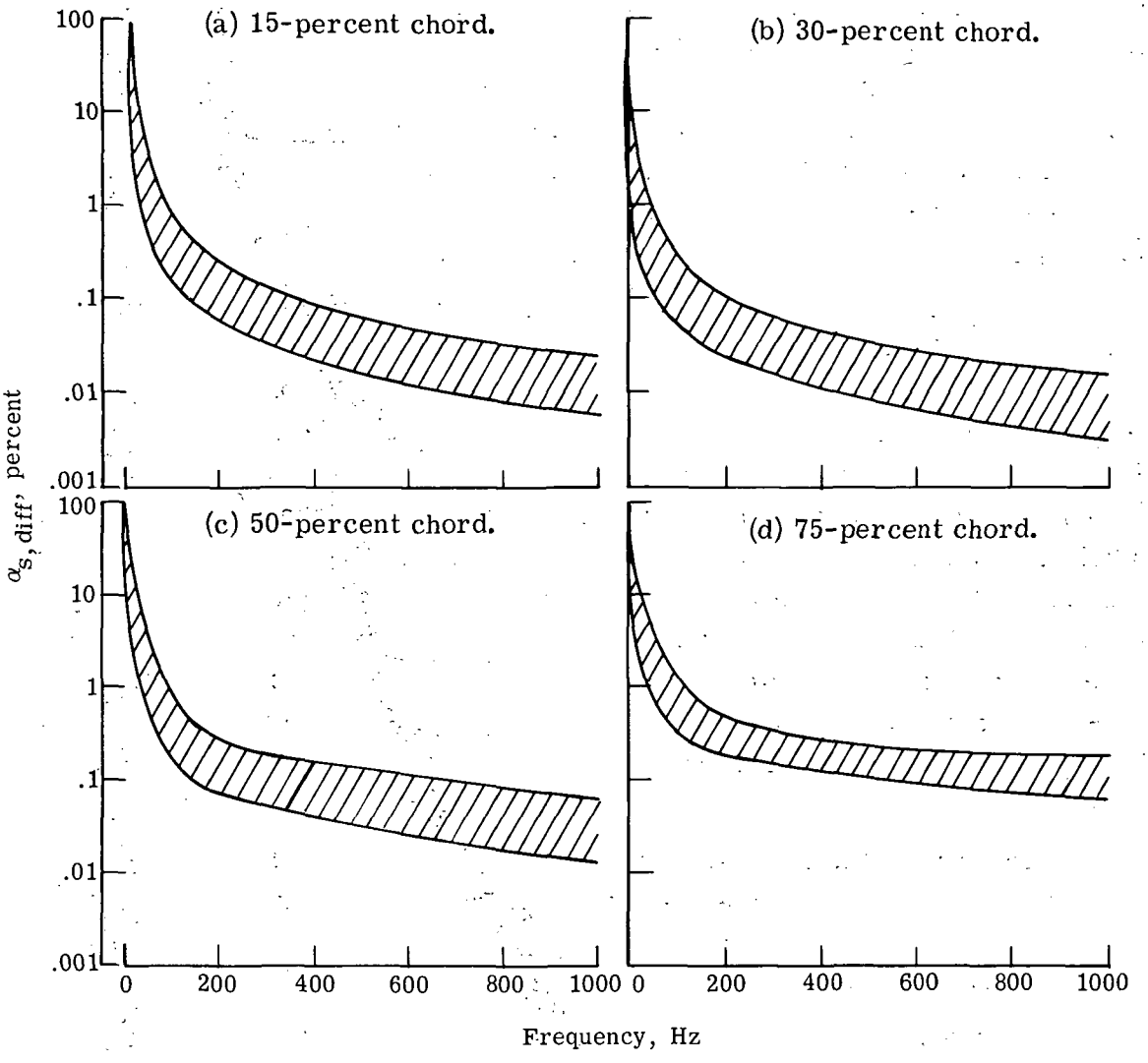

Figure 15.- Composite differential blade loading coefficients $\alpha_{s,diff}$ (for all test conditions listed in table II) at 15-, 30-, 50-, and 75-percent chord.

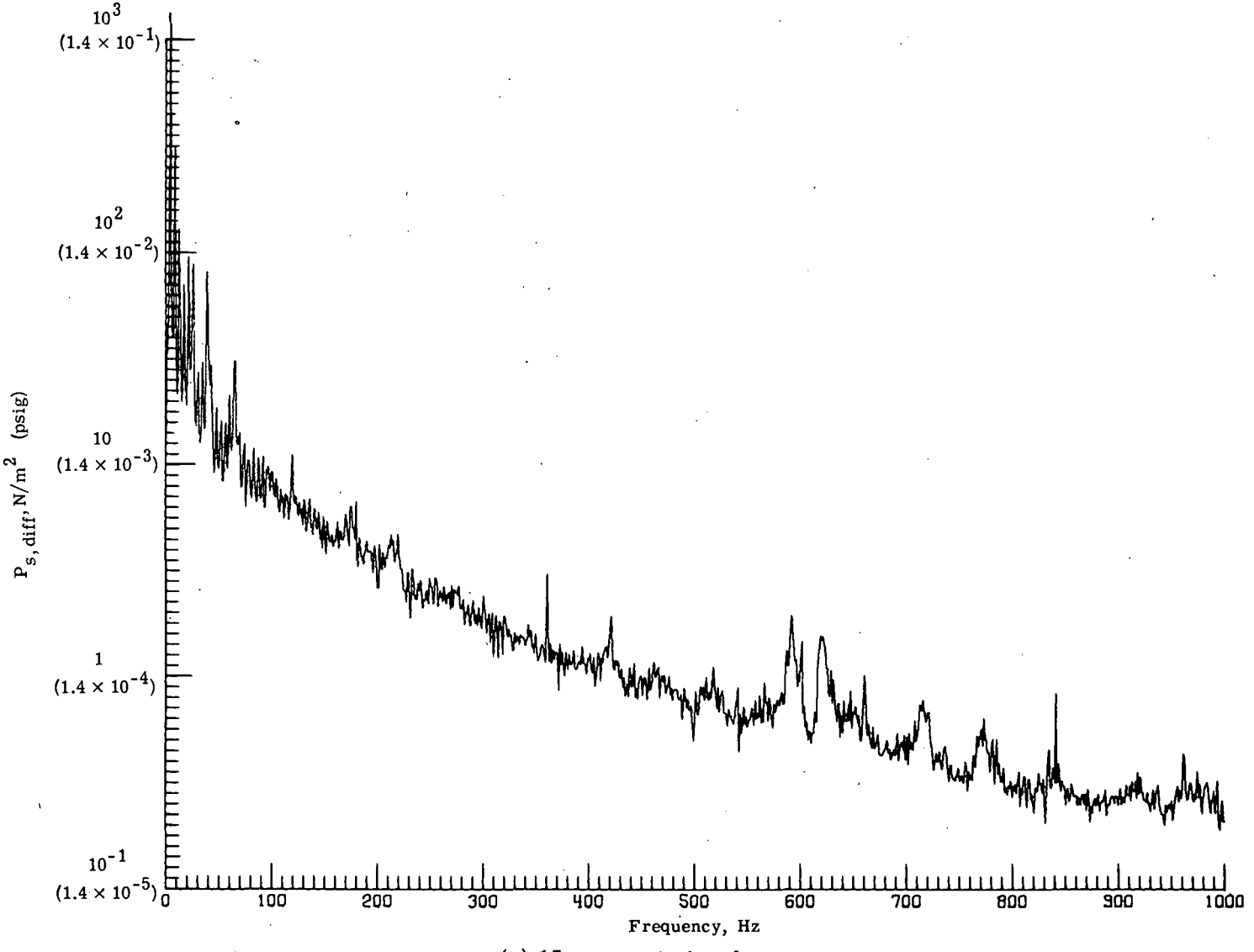

(a) 15-percent chord.

Figure 16.- Typical differential blade pressure spectra.

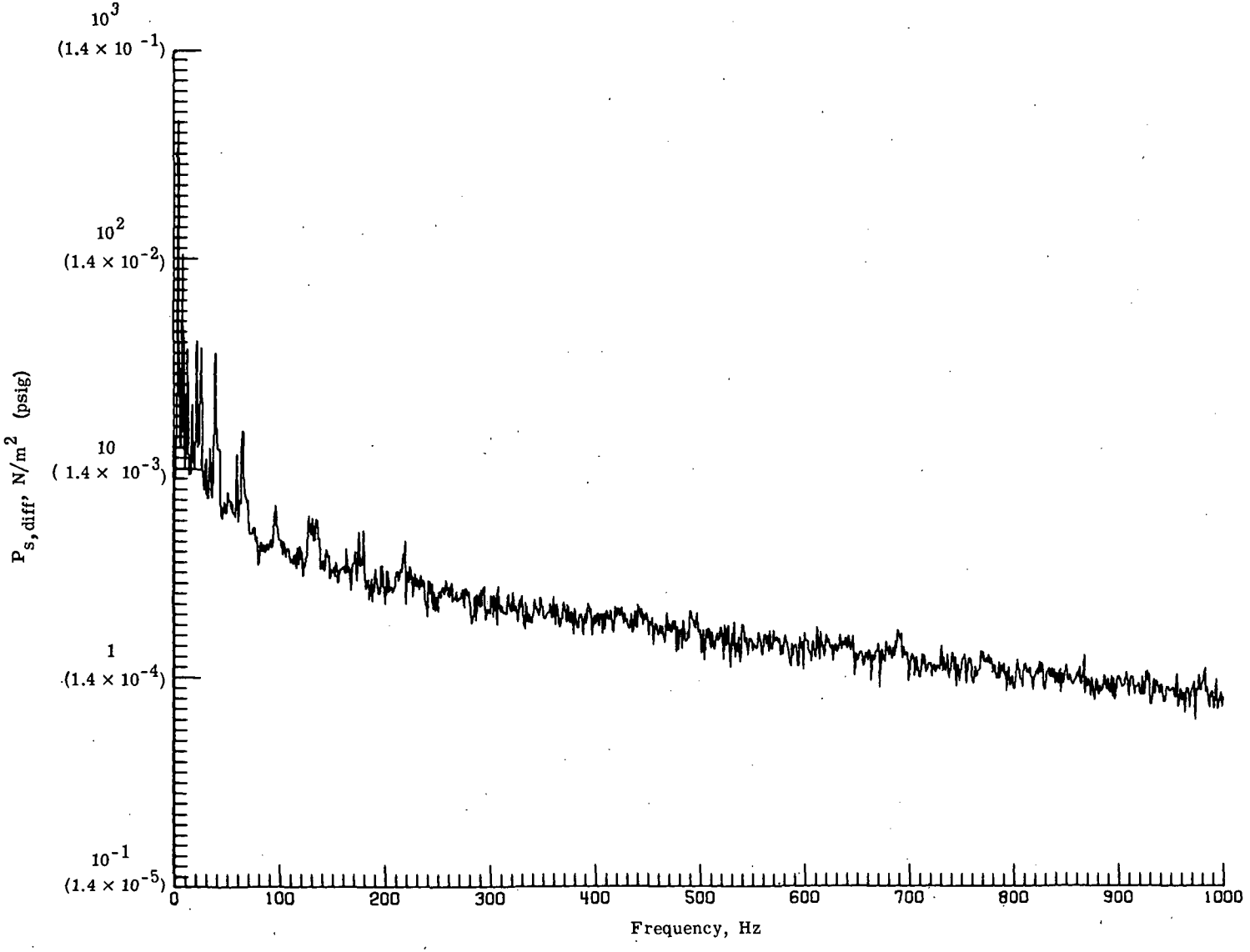

(b) 75-percent chord.

Figure 16.- Concluded.

Integrated Differential Blade Loading Coefficients

Because of the variation of the differential blade loading coefficients from chord station to chord station, the following procedure was used to produce loading coefficient spectra representative of the entire 80-percent span station. The amplitude and phase of each differential blade pressure harmonic measured at each chord station were used in a spline interpolation routine (see ref. 19) to provide better definition of the chordwise pressure distribution. In performing the interpolation, the conventional assumption that the blade pressure amplitude is zero at the leading and trailing edges was made. The interpolated blade pressure amplitudes and phases were then chordwise integrated using a Simpson-Newton 3/8 rule (see ref. 20). Integrated differential blade loading coefficients $\alpha_{s,diff,int}$ were then formed by normalizing the amplitudes of the integrated pressure harmonics by the integrated differential uniform lift $P_{0,diff,int}$. Figure 17(a) shows a typical full-chord integrated $\alpha_{s,diff,int}$ spectrum. It is characterized by a predominance of low-frequency discrete tones which gradually make a transition into a continuous spectrum near 200 Hz. The first harmonic level is 41 percent of the uniform load. The spectrum fall-off rate begins at about 12 dB per octave and then gradually flattens to a 6 dB octave rate. The flattening of the spectrum is attributed to the influence of the higher amplitude broadband data at the 50- and 75-percent chord stations.

In order to reduce the influence of the more broadband loading at 50- and 75-percent chord, the amplitudes of the blade pressures beyond 40-percent chord were set equal to zero after interpolation. The pressures were then integrated and normalized over the leading 40 percent of the rotor blade. Figure 17(b) shows a typical 40-percent chordwise-integrated blade loading coefficient spectrum. This spectrum is characterized by a predominance of low-frequency discrete tones which gradually make a transition into a continuous spectrum. However, the transition occurs near 300 Hz rather than 200 Hz as in the full-chord case. The first harmonic level is about 47 percent of the uniform load. This is comparable with the 41 percent observed in the full-chord case. The fall-off rate is about one-half of the full-chord case, beginning with a 6 dB per octave and increasing to 8 dB per octave. Occasional discrete spikes can also be observed in the continuous portion of the spectrum. These may be caused by periodic inflow turbulence, although there is no conclusive evidence to support this. Also, although the spectrum does tend to become continuous beyond 300 Hz, there are intermittent areas of discrete spectrum up to 700 Hz.

Superimposed Integrated Differential Blade Loading Spectra

The superimposed integrated differential $\alpha_{s,diff,int}$ spectra at 80 percent span from all the conditions listed in table II are shown in figures 18(a) and 18(b). Figure 18(a) shows the superimposed full chord integration spectrum. It reflects the fall-off trend seen in the typical spectrum, a rapid initial fall-off with a rather rapid flattening of the fall-off.

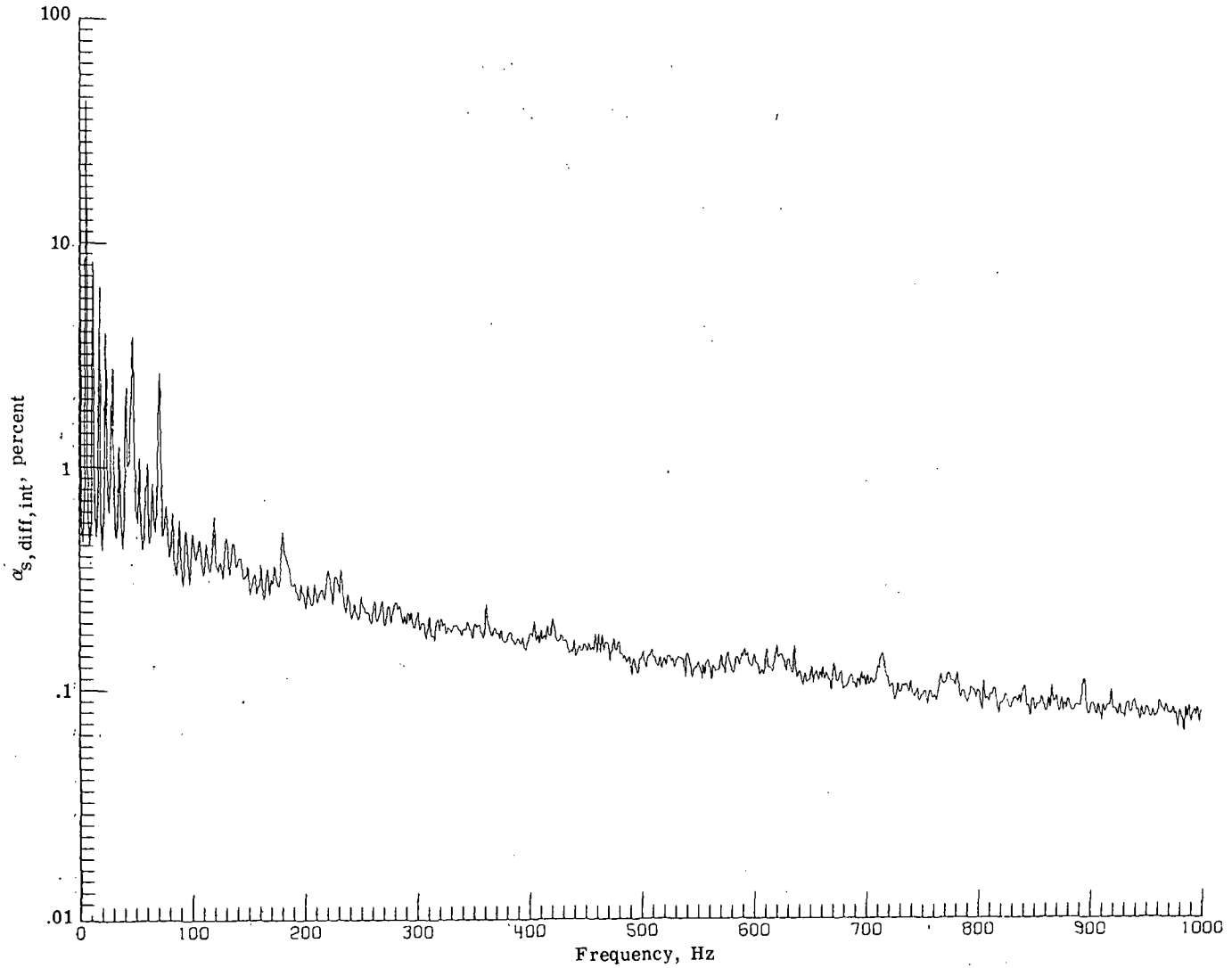

(a) Full chord integration.

Figure 17.- Typical integrated differential blade loading coefficients.

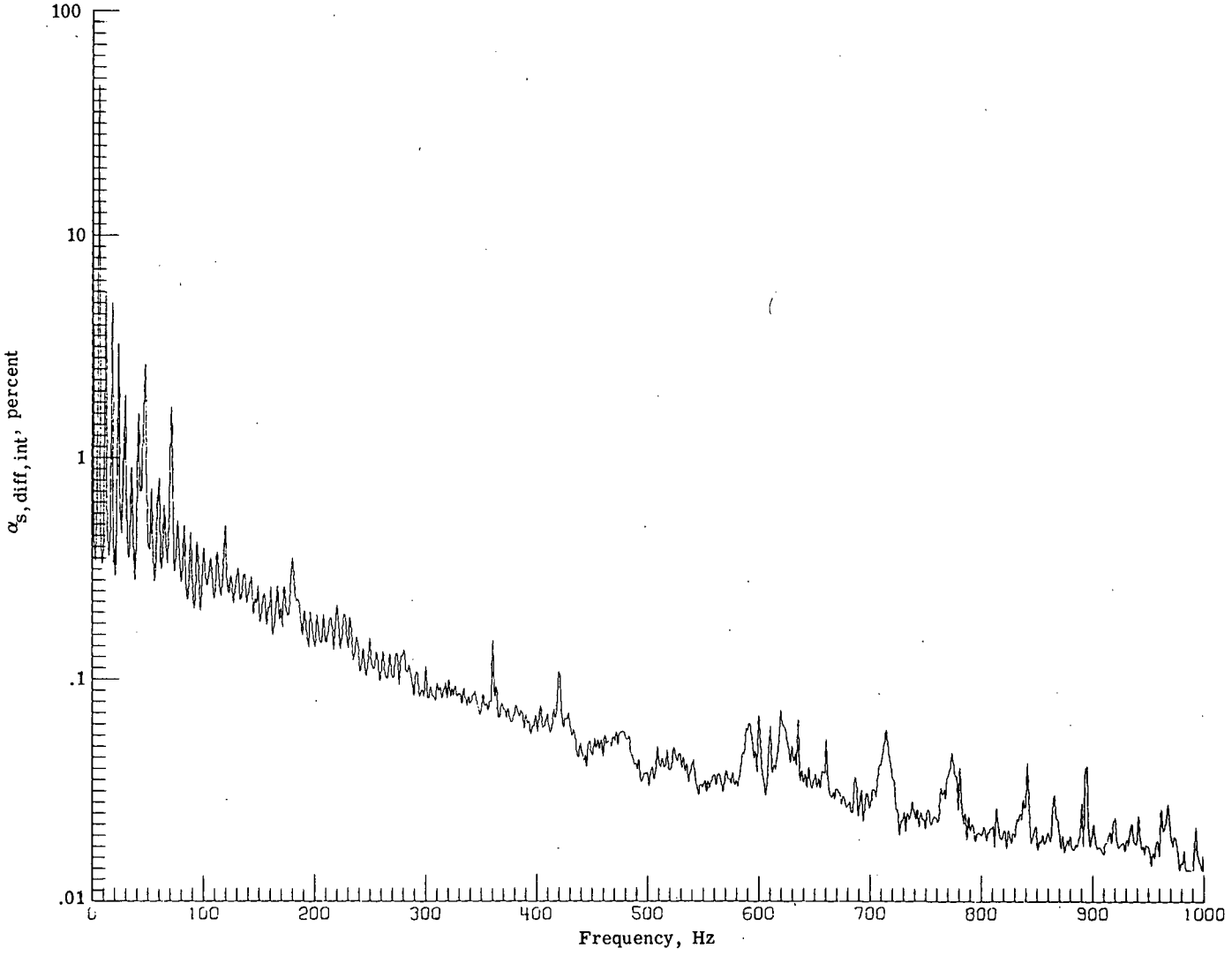

(b) 40-percent chord integration.

Figure 17.- Concluded.

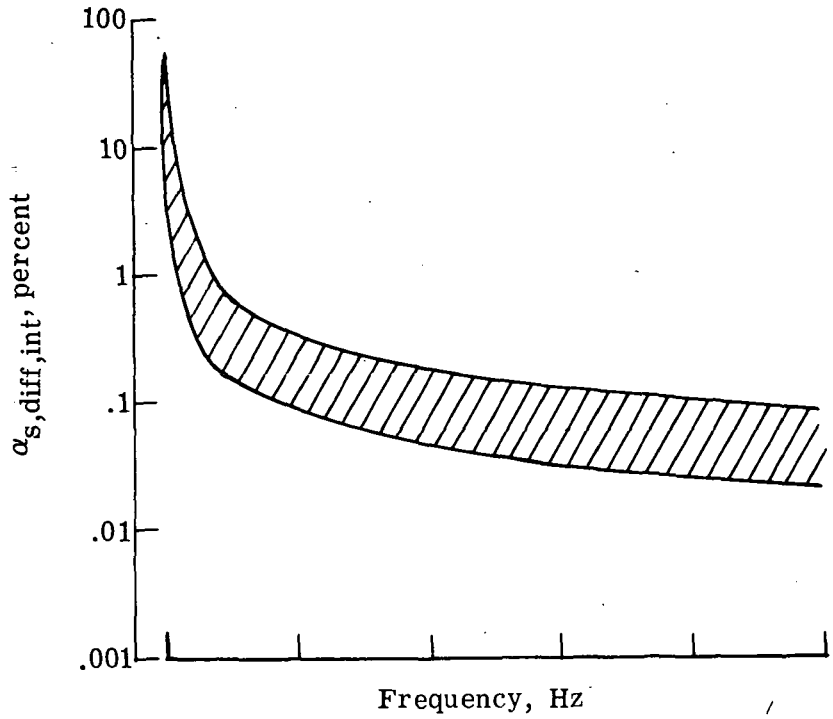

(a) Full-chord integration.

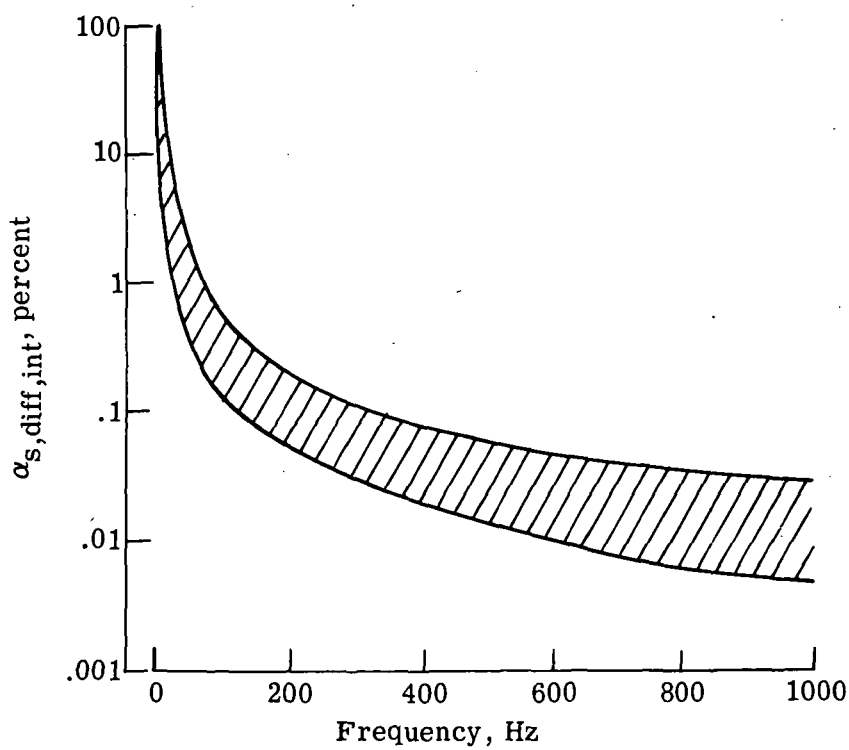

(b) 40-percent chord integration.

Figure 18.- Superimposed integrated differential blade loading coefficients.

The superimposed 40-percent chord integrated differential $\alpha_{s,diff,int}$ spectra are shown in figure 18(b). Again the fall-off trend observed in the typical spectrum is reflected in the superimposed spectrum. The spectrum begins with and sustains a 7 to 10 dB per octave fall-off. The fundamental blade-loading harmonic amplitude is seen to have a maximum level of about 65 percent of the uniform loading in both the full and 40-percent integration cases.

ROTOR ROTATIONAL NOISE THEORY

Background

The classical theory on discrete noise radiation is that presented in reference 1. There the far-field acoustic analysis was based on the sound radiated from a uniform blade loading force under steady inflow conditions. The predictions resulting from reference 1 agreed with measured rotational noise data only for rotors and propellers with high tip Mach numbers. At moderate and low tip Mach numbers the results diverged drastically from the measured data (see fig. 19), with the exception of the first harmonic.

Reference 26 extended the work of reference 1 by incorporating forward-speed effects for a propeller. The theories of references 2 and 7 were the first to formulate the fluctuating aerodynamic blade loads concept for rotor rotational-noise prediction. In reference 6 measured blade loading data were used to predict rotor rotational noise up to the 10th acoustic harmonic but good agreement was achieved for about the first 5 acoustic harmonics.

In order to allow calculations of the rotational noise based on the blade loading data measured in this study, the theory of references 7 and 8 was used. This section outlines the salient points of that theory.

Fluctuating-Blade Loads Theory

The objective of the analysis is to solve a wave equation of the form

$$\frac{1}{a_0^2}\frac{\partial^2 P}{\partial t^2} - \frac{\partial^2 P}{\partial x_i^2} = \frac{\partial Q}{\partial t} - \frac{\partial F_i}{\partial x_i} + \frac{\partial^2 T_{ij}}{\partial x_i \partial x_j} \tag{1}$$

The mass source monopole Q accounts for discrete thickness noise radiation; however, it is considered of secondary importance for low and medium tip speed rotors and will not be included in the analysis. The stress tensor T_{ij} is a quadrupole source and, therefore, will also be neglected in the analysis. This leaves only the force $\overline{F}$ (the bar indicates a vector quantity) on the right-hand side of equation (1). The forces and rotor coordinate system used are shown in figure 20.

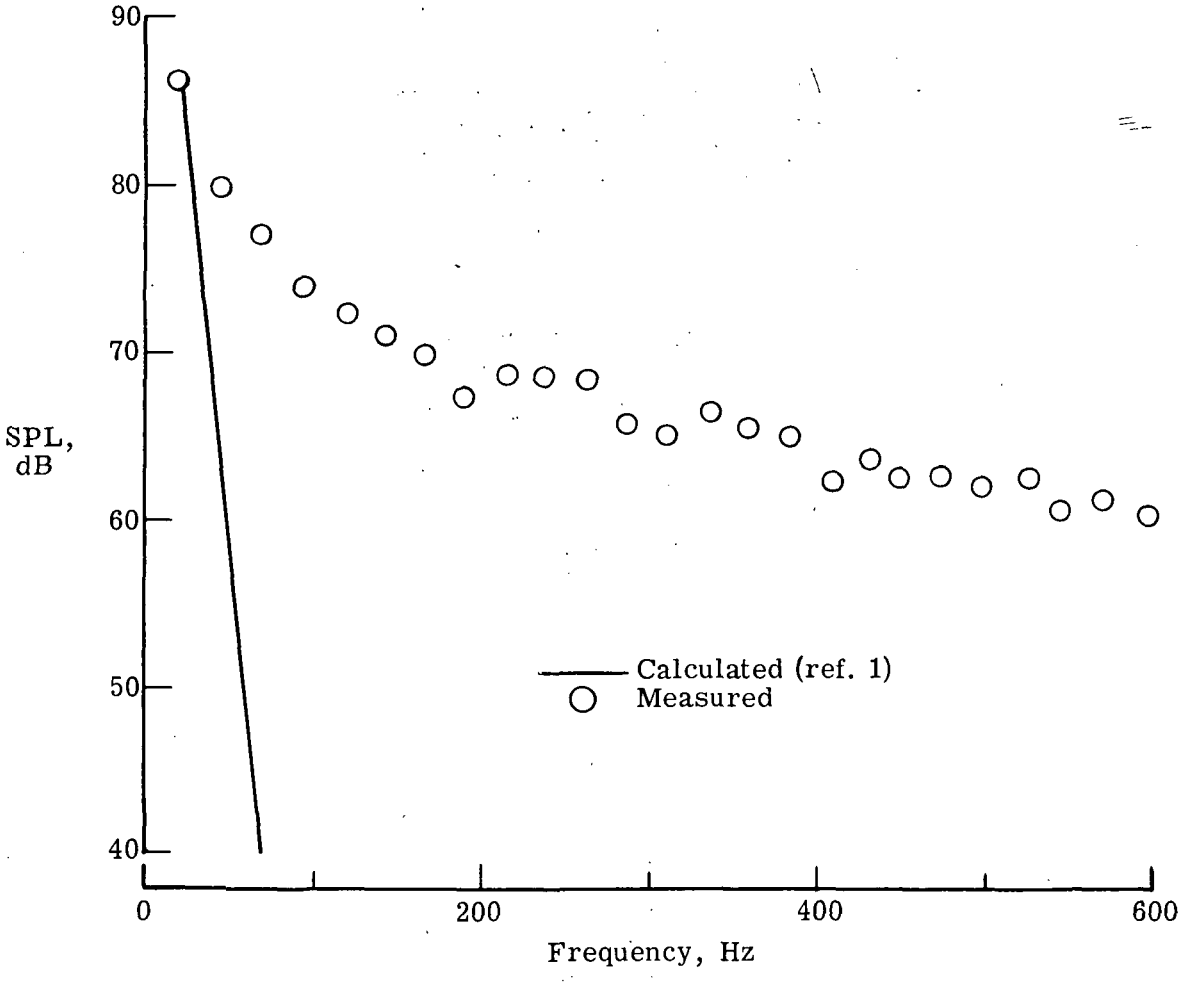

Figure 19.- Comparison of measured rotational noise with calculated values obtained by using the procedure of reference 1.

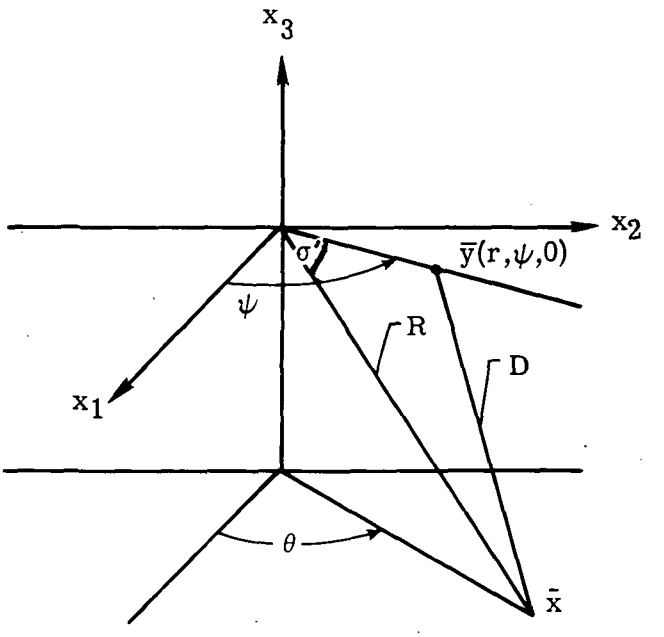

(a) Rotor.

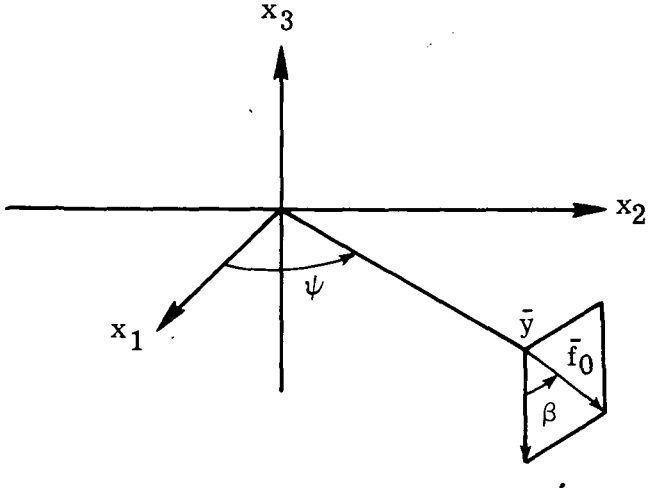

(b) Forces.

Figure 20.- Coordinate system.

In deriving equation (1), it was assumed (refs. 2 and 27) that the fluid was an inviscid and nonconducting medium. The force field component F_i should include all the loads on the rotor system. In the theory of reference 7 the forces are considered to be concentrated at an effective rotor radius of 0.8 span. Figure 21 conceptually illustrates the components of these aerodynamic blade pressures (or forces) at an arbitrary effective radius r_e. It is seen that the pressures are composed of uniform and fluctuating components. Furthermore, the fluctuating component contains both periodic and nonperiodic pressures. Only the uniform and periodic components are required to calculate rotational noise and, as will be seen later, use of nonperiodic data causes the calculated noise levels to deviate from the measured noise. A detailed solution of equation (1) for the far-field radiated sound pressure is presented (following the analysis of ref. 7) in appendix A. Highlights of that solution are now discussed.

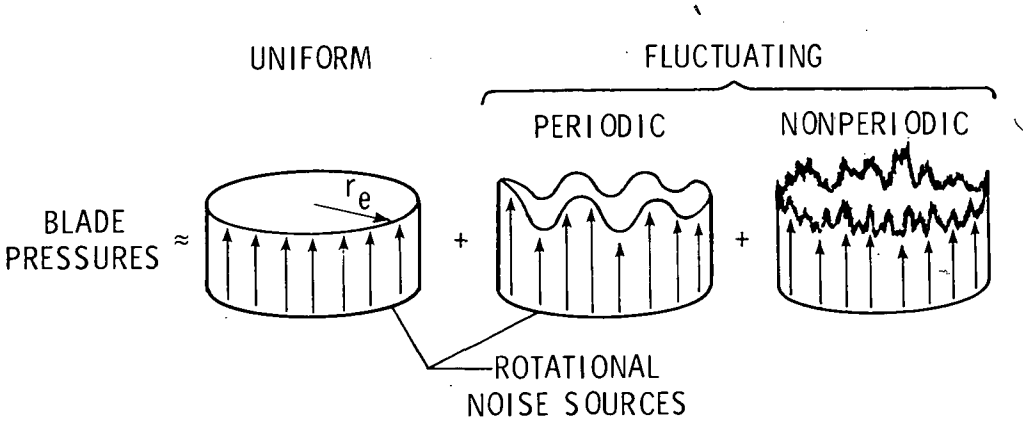

Figure 21.- Components of aerodynamic blade pressures.

If loading phases and observer azimuth angle θ are ignored, the contribution of the s^{th} blade loading coefficient to the mB^{th} far-field sound pressure harmonic is (see appendix A, equation A(15))

$$\underline{SP}_{mB,s} = \frac{\alpha_s}{2} \chi_{mB} \left[\left(K_L - K_D \frac{q_-}{mB} \right) \gamma_{q_-} + \left(K_L - K_D \frac{q_+}{mB} \right) \gamma_{q_+} \right] \tag{2}$$

Blade loading coefficients.- For purposes of interpretation, equation (2) can be divided into three quantities. The first quantity is the contribution of the fluctuating blade loads given by the blade loading coefficient $\alpha_s = P_s/P_0$. As discussed earlier, the coefficients α_s may come from individual blade measurement stations or may be integrated

across the chord to provide a spectrum representative of a particular spanwise station. Both station and integrated blade-loading-coefficient spectra are used later in this report to calculate the rotational noise.

Chordwise loading distribution.- The second quantity of equation (2) is the loading distribution function χ_{mB}. This function could describe both the spanwise and chordwise distribution of the uniform and fluctuating blade loads. However, since the spanwise distribution was ignored by concentrating all the loading at 0.8 span, only the chordwise distribution of the blade loads was included in this analysis. Figure 22 illustrates a typical chordwise loading distribution. In figure 22(a) the resultant uniform and fluctuating loads are shown at a given instant of time. The mean area under the distribution represents the total load per blade. The magnitude of this load is absorbed in the operating parameters K_L and K_D. The shape of the distribution is contained in the function χ_{mB}, determined from a Fourier decomposition of the distribution as a function of time. Figure 22(b) shows a time history of the loading distribution as seen at an arbitrary, but fixed, point on the rotor disk. It will be noted that the reaction of the air is a reflection of the blade pressure distribution about the leading edge of the airfoil. Also, the time history has a periodic nature with a period $\tau = \frac{1}{BN}$. The duration of the distribution is equal to the blade chord divided by the rotor speed at the disk point. Therefore, χ_{mB} is a function of the acoustic harmonic number mB.

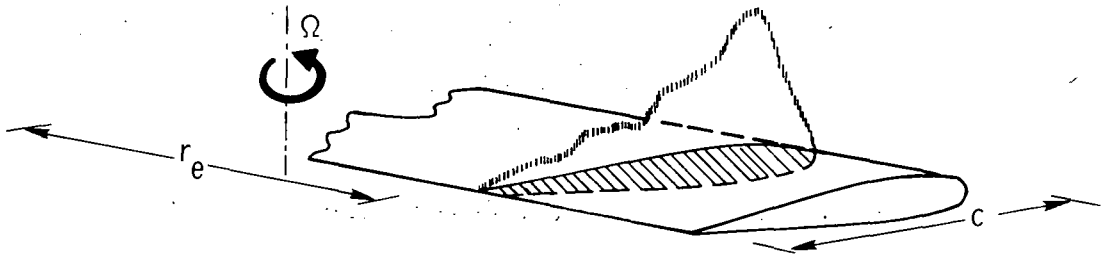

(a) Distribution at instant of time.

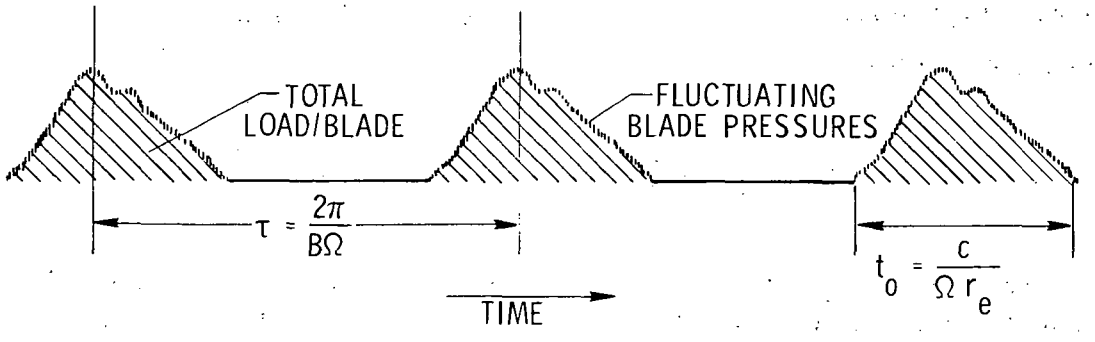

(b) Time history of loading distribution.

Figure 22.- Typical chordwise loading distribution.

In actuality each blade loading harmonic may have a unique chordwise distribution making the distribution function dependent on both the acoustic and loading harmonic numbers. For the purposes of this study both the uniform and fluctuating blade loads were assumed to be chordwise distributed in the same manner. Table V, after reference 8, shows the chordwise distributions and associated χ-functions used in this study. Although not reported here, the exact α_s distributions were measured when the data for this report were acquired.

Operating constants.- The remaining terms in equation (2) form the third quantity in the equation. The term $K_L = \frac{N}{Ra_0} L_F \sin \sigma'$ is called the rotor lift constant and is a function of the shaft frequency N, the observer distance R and observer elevation angle σ', the speed of sound a_0, and the total rotor lift force L_F. The term $K_D = \frac{N}{Ra_0} \frac{D_F}{M_e}$ is called the rotor drag constant and is a function of the total rotor drag D_F, the observer

TABLE V.- CHORDWISE LOADING DISTRIBUTIONS AND ASSOCIATED χ-FUNCTIONS

Distribution		χ-function
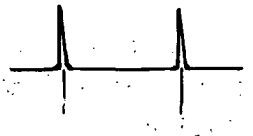	Point loading	$\chi_{mB} = 1$
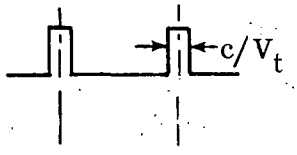	Rectangular loading	$\chi_{mB} = \frac{\sin\left(\frac{mBc}{2r}\right)}{mBc/2r}$
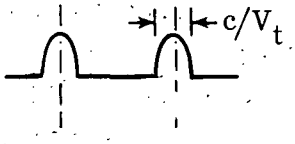	Half-cosine loading	$\chi_{mB} = \frac{\cos\left(\frac{mBc}{2r}\right)}{1 - \left(\frac{mBc}{\pi r}\right)^2}$
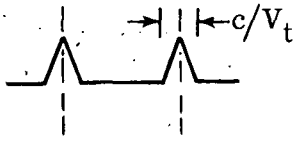	Triangular loading	$\chi_{mB} = \left[\frac{\sin\left(\frac{mBc}{4r}\right)}{mBc/4r}\right]^2$
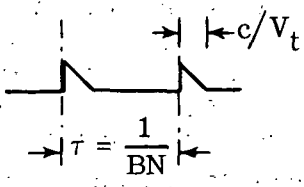	Sawtooth loading	$\chi_{mB} = \frac{1 - \exp\left(-j\frac{mBc}{\pi r}\right) - j\frac{mBc}{\pi r}}{\frac{1}{2}\left(mBc/r\right)^2}$

distance R, the speed of sound a_0, and the effective Mach number M_e (usually the Mach number at 80-percent span). The terms $\gamma_{q_-} = mBJ_{q_-}(mBM_e \cos \sigma')$ and $\gamma_{q_+} = mBJ_{q_+}(mBM_e \cos \sigma')$ are functions of the acoustic harmonic number mB and the Bessel function J_q of argument $mBM_e \cos \sigma'$. The indices $q_\pm = mB \pm s$. The combined effect of these terms is to provide the net lift and drag contributions and overall directivity according to the elevation angle σ'.

General Discussion of Theory

In developing equation (2) the following assumptions were made in reference 7:

(1) Equation (1) is valid only for a nontranslating system.

(2) Far-field approximations are made.

(3) All the rotor loads are concentrated at an effective radius of 0.8 span.

(4) The rotor inflow is steady but nonuniform; therefore, each blade experiences the same load fluctuations every revolution. (Although the inflow is steady and nonuniform, the rotor loads can be Fourier decomposed into steady uniform, or dc, loads and steady nonuniform, or fluctuating, loads.) See figure 21.

(5) The loading distribution across the chord is described by generalized loading profiles. (The Fourier transform of these loading distributions yields the χ-functions discussed earlier in this section.) Typical distributions are: point loading, rectangular loading, half-cosine loading, triangular loading, and sawtooth loading.

The first three assumptions are implicit in the theory but the last two are subject to experimental verification. The pressure-time histories presented earlier (see fig. 10) seem to indicate a steady but nonuniform inflow. Even so, for the purposes of this study, the blade loading spectra were made steady by the averaging techniques discussed in the section "Data Reduction and Analysis." This is seen in the periodic nature of the pressure-time histories and in the discrete nature of the spectra (see fig. 12). In the next section the effect of the various chordwise loading distributions on the radiated noise is discussed, and experimentally determined loading coefficients are used to compute the radiated rotational noise.

From equation (2) it is seen that for a particular mB and s number the resulting sound pressure is generated by two modes, q_- and q_+. These modes are defined as rotating sinusoidal pressure patterns with spinning speeds of $mB\frac{\Omega}{q_-}$ and $mB\frac{\Omega}{q_+}$ for the q_- and q_+ modes, respectively. The spinning effect causes each mode to move periodically toward and away from the observer, allowing each blade loading harmonic to contribute to the level of more than one sound harmonic. Viewed from the observer's frame, each sound harmonic is composed of the contributions of many (in theory an infinite

number) loading harmonics with the strongest contribution coming from the loading harmonic whose order s is equal to the order of the sound harmonic mB.

The final result from this multimodal analysis, including all loading phases $\phi_{q\pm mB}$, the observer azimuthal angle θ, and the retarded time $t - \frac{R}{a_0}$ is (see appendix A, eq. A(21))

$$SP_{mB} = \exp\left[jmB\Omega\left(t - \frac{R}{a_0}\right)\right] \chi_{mB}\left[\frac{\alpha_0}{2}\left(K_L - K_D\right)\gamma_{mB}\exp\left[j\left(mB\theta - \phi_0\right)\right]\left(-j^{mB+1}\right)\right.$$

$$+ \frac{\alpha_{mB}}{2} K_L \gamma_0 \exp\left(-j\phi_{mB}\right)(-j)$$

$$+ \sum_{q=1}^{\infty}\left(\frac{\alpha_{|q-mB|}}{2}\left(K_L - K_D\frac{q}{mB}\right)\gamma_q \exp\left\{j\left[q\theta + \left(2S_q - 1\right)\phi_{|q-mB|}\right]\right\}\right.$$

$$\left.\left. + \frac{\alpha_{mB+q}}{2}\left(K_L + K_D\frac{q}{mB}\right)\gamma_q \exp\left[-j\left(q\theta - \phi_{|mB+q|}\right)\right]\right)\left(-j^{q+1}\right)\right] \tag{3}$$

For a particular sound harmonic mB, the Bessel function J_q varies rapidly with loading harmonic number s. Figure 23 shows the result obtained in reference 27 where the magnitude of the Bessel function $J_q(Z_0) \approx 10^{-4}$ or $J_q(Z_0) \approx 10^{-5}$ for specific values of the order and argument. For this work the criterion

$$q = \left[10 + \frac{5}{4} Z_0\right] \tag{4}$$

(where $Z_0 = mBM_e \cos\sigma'$ and $[\,]$ indicates the integer part of $10 + 5/4\ Z_0$) was chosen as the maximum Bessel function order because any $J_q(Z_0)$ with $q > \left[10 + 5/4\ Z_0\right]$ were assumed to equal zero. Thus, the infinite summation in equation (3) can be replaced by a finite upper limit given by equation (4). Since $q = mB \pm s$, the finite limit is interpreted as defining a band of loading harmonics s, centered about $s = mB$ (that is, $q = 0$), which contribute to each sound harmonic mB (see refs. 7 and 8 and appendix A).

In reference 8 the modes $q_+ = mB + s$ were dropped from the analysis. However, in reference 28 it was commented that the terms q_+ have a nonnegligible effect on the calculations at low acoustic harmonic mB. For this reason the modes q_+ were retained in the present analysis.

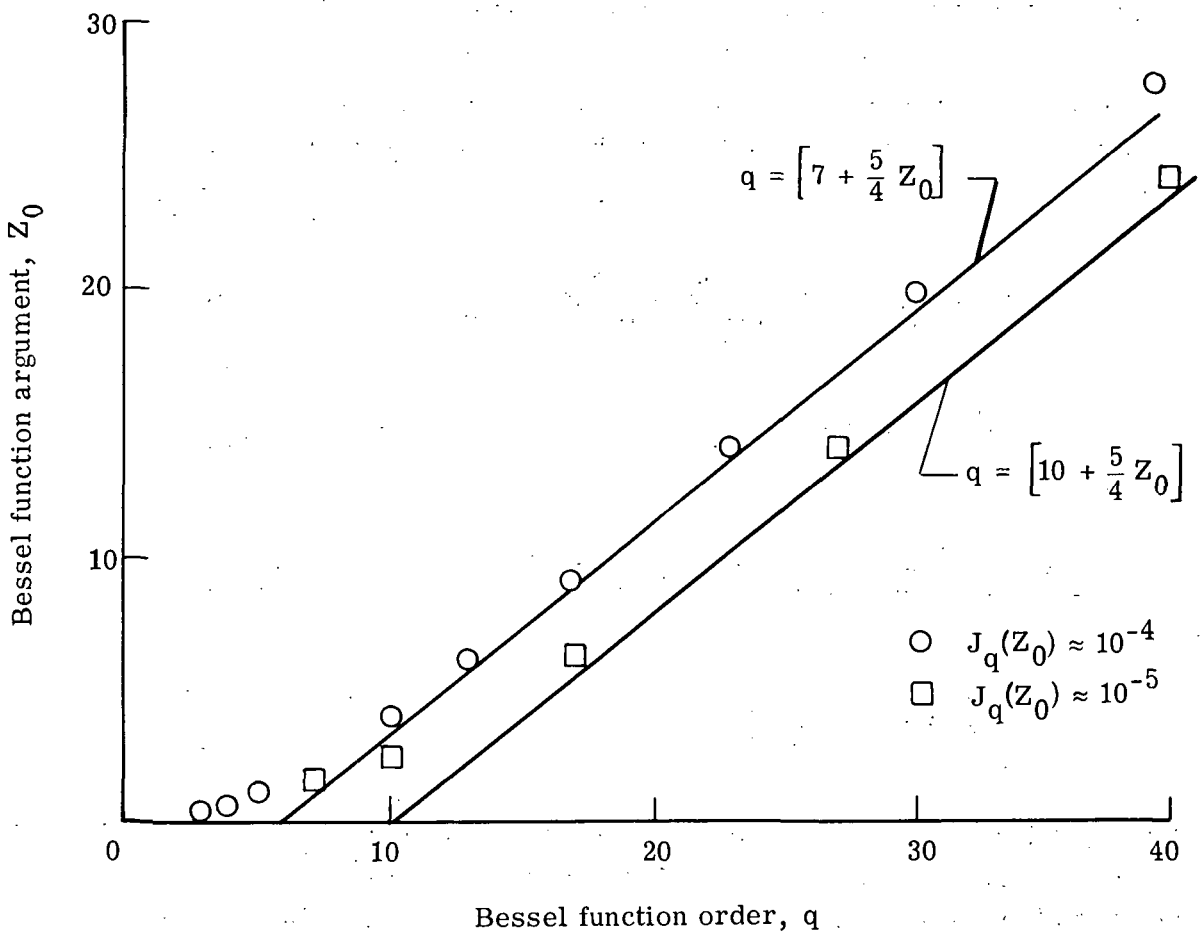

Figure 23.- The effect of argument Z_0 and order q on the Bessel function $J_q(Z_0)$.

If, in equation (3), only the uniform loading (s = 0) is considered and all the phases are neglected (as indicated by the bar), equation (3) reduces to

$$\underline{SP}_{mB} = \left(K_L - K_D\right)\gamma_{mB} \tag{5}$$

This is the same result obtained in reference 1.

COMPARISON OF CALCULATED AND MEASURED ROTATIONAL NOISE

This section presents a comparison of rotational noise calculations, using the theory of references 7 and 8 and the measured blade loading data discussed earlier, with rotational noise measured at microphone positions 1 and 2 (see fig. 2). Data are shown for all seven conditions listed in table II. Before discussing the final results, however, data are pre-

sented which show the effect of various α_s spectra, chordwise distribution (χ) functions, and blade-loading phase angle/observer angle on rotational noise calculations.

Effect of Blade Loading Spectra on Calculated Rotational Noise

In order to implement the theory of references 7 and 8, a knowledge of the blade loading coefficients α_s is required. These coefficients could be obtained from measurements at a single chordwise station or they could come from an integration of the station loading coefficients. In order to determine which loading coefficients allowed the most accurate calculations of the rotational noise, differential blade-loading coefficient spectra from 15-, 30-, 50-, and 75-percent chord stations and from full and 40-percent chordwise integrations were used with a point loading distribution to predict the rotational noise. Typical results from these calculations (based on condition 6, table II) are presented in figure 24. Here calculations using each of the above mentioned blade loading spectra are compared with measured rotational noise spectra. (The circles represent the noise level at the frequencies mBN, harmonics of the blade passage frequency. It should be noted that the noise at these frequencies may not be caused by rotational noise beyond the rotational-broadband transition range.) It can be seen from figure 24(a) that the calculations based on loading data from the 30-, 50-, and 75-percent chord station and the full chord integration did not provide good agreement with the measured noise. Calculations based on loading data from 15-percent chord and a leading 40-percent chordwise integration provided good agreement with the measured noise throughout all but the highest five acoustic harmonics. In a majority of the calculations the 40-percent chordwise loading integration provided the best agreement with measured rotational noise. The poor agreement using the 50- and 75-percent chord station and full chord integration data can be understood in terms of the data shown in figures 15 to 17. In these figures the strong influence of broadband loading over the trailing 50 percent of the airfoil was noted. Since the theory of reference 7 is meant to calculate discrete rotor noise from discrete loading spectra, the broadband content of the 50- and 75-percent chord station and full chord integration spectra causes the calculated rotational noise to not agree with measurements.

Conversely, the good agreement between measurements and calculations using measured blade loading coefficients from the 15-percent chord station, or integrated over the leading 40 percent of the airfoil, may be attributed to a more accurate representation of the discrete blade loading spectrum. There were occasions where calculations using the 40-percent integration did not provide the best agreement with measurements. Figure 24(b) shows such a case. Here, the loading data from 30-percent chord provided the best agreement with measured noise. However, the 40-percent chordwise integration provided the next best agreement. Thus, because the leading 40-percent chordwise integrated, differential loading spectrum provided a good representation of the discrete blade loads and

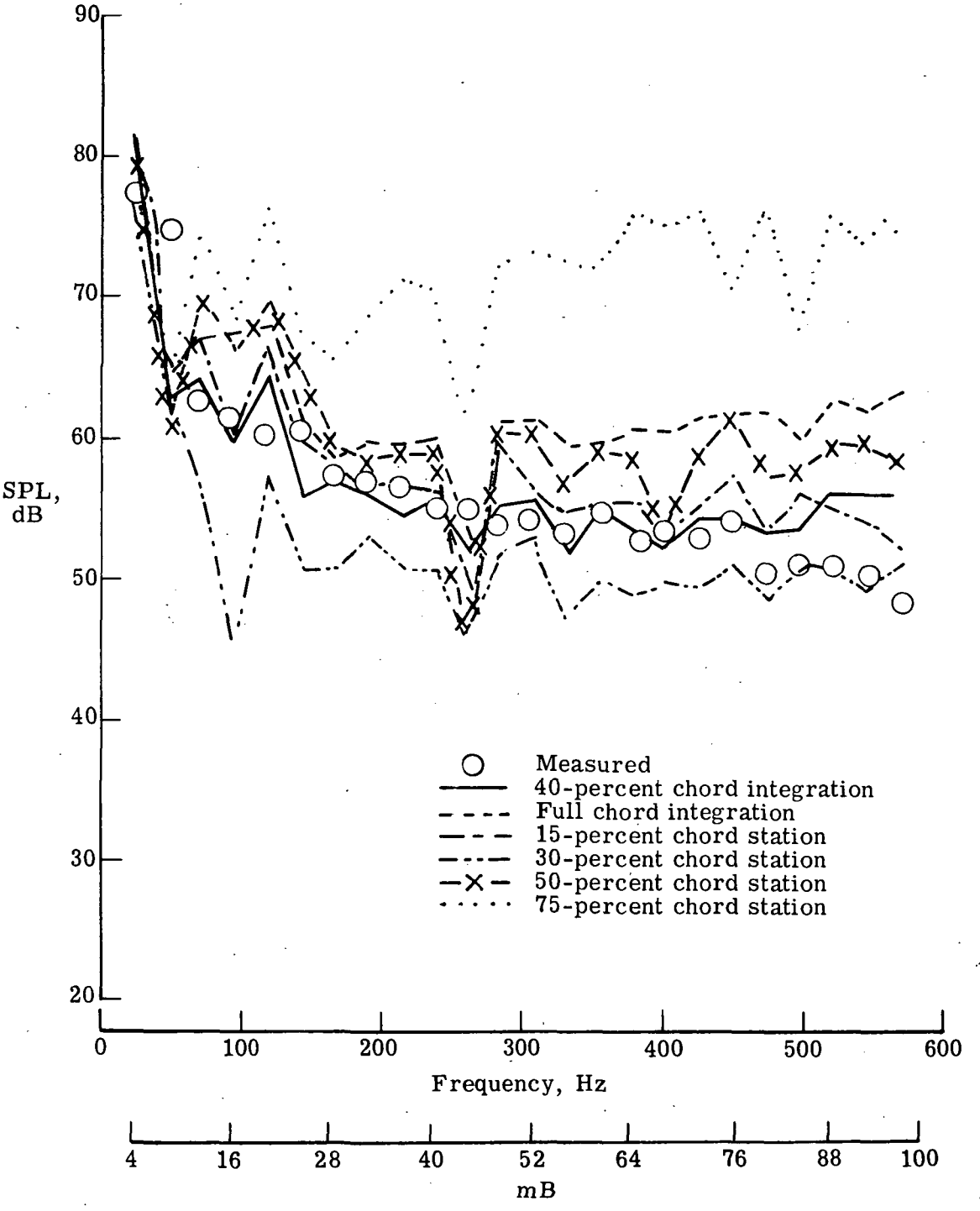

(a) Microphone position 2.

Figure 24.- The effect of various blade loading spectra on calculated rotational noise, obtained by using a point loading distribution.

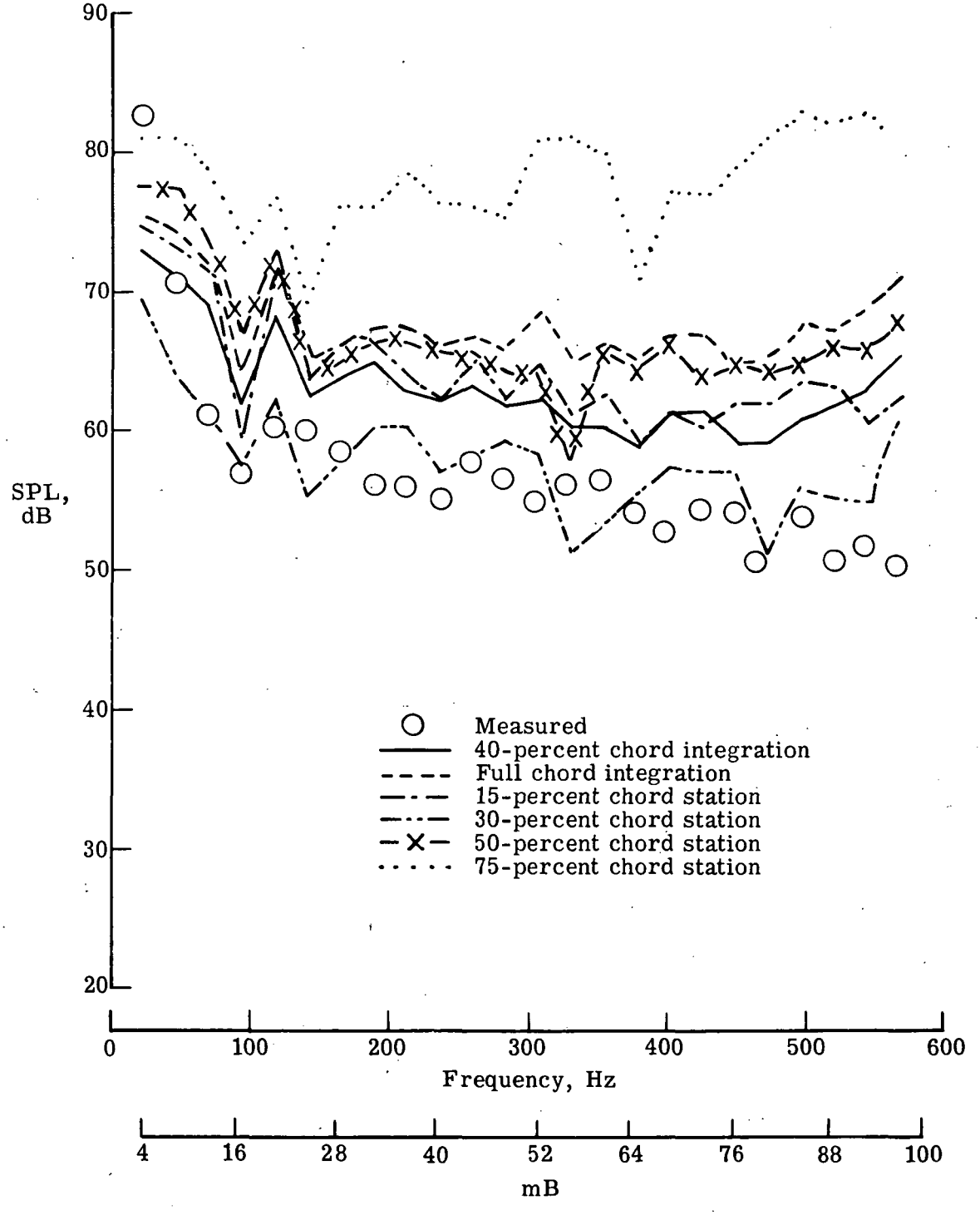

(b) Microphone position 1.

Figure 24.- Concluded.

because it seemed to provide good agreement between calculated and measured rotational noise, it was used to compute the rotational noise for all the conditions listed in table II. These data will be shown later.

Effect of Chordwise Distribution of the Blade Loading Coefficients on Calculated Rotational Noise

In discussing the theory of references 7 and 8, it was mentioned that the chordwise loading distribution function (χ_{mB}) influences the rotational noise calculations. In order to determine the strength of this effect, the leading chordwise integrated, differential loading spectrum was distributed according to each of the functions shown in table V. Typical results (based on condition 6, table II) are shown in figures 25(a) and 25(b). At the low acoustic harmonics, all the distributions seem to provide the same calculated noise level. As the harmonic number increases, however, the influence of each distribution becomes apparent. In figure 25(a), typical of a majority of the cases, it was observed that the point loading distribution provided the best agreement between calculated and measured rotational noise. The rectangular distribution always gave the poorest agreement, while the remaining distributions occasionally provided the best agreement with measured data. One such case is shown in figure 25(b). Here, three distributions provide better agreement with the measured noise than did the point loading distribution. These data indicate that the loading distribution can affect the calculation results particularly at the higher acoustic harmonics.

Effect of Blade-Loading Phase Angle and Observer Angle on Calculated Rotational Noise

In the absence of any conclusive experimental evidence, previous experimenters have assumed either zero or random blade loading phases (refs. 7 and 8). In reference 29 it is concluded that neither the blade loading phases nor the observer angle θ is important for calculating rotational noise for a hovering rotor. In the strictest sense the latter statement is certainly true if a hovering rotor is construed to have only steady, uniform blade loading. However, nonuniformity in the loading, even for the nontranslating rotor studied in this report, will cause a variation in the radiated rotational noise with observer angle θ. Theoretically, the effect of observer angle and blade loading phase ϕ can be seen in exponential terms of the general form $\exp\left[-j\left(q\theta + \phi_{|q\pm mB|}\right)\right]$ (see eq. (3)). Here q is a blade-loading model index. This expression implies that the value of the loading phase, $\phi_{|q\pm mB|}$ will affect the calculated acoustic harmonic SP_{mB} in the same manner as the product $q\theta$. Figure 26 illustrates this effect conceptually. Here, two loading modes, one high order and one low order, are shown in planform superimposed on the rotor disk. The observer position and its associated angle are shown in reference to the line where the Fourier analysis of the blade loading began (appendix B explains the experimental procedure used to determine θ). All loading phases are referenced to this line. Considering

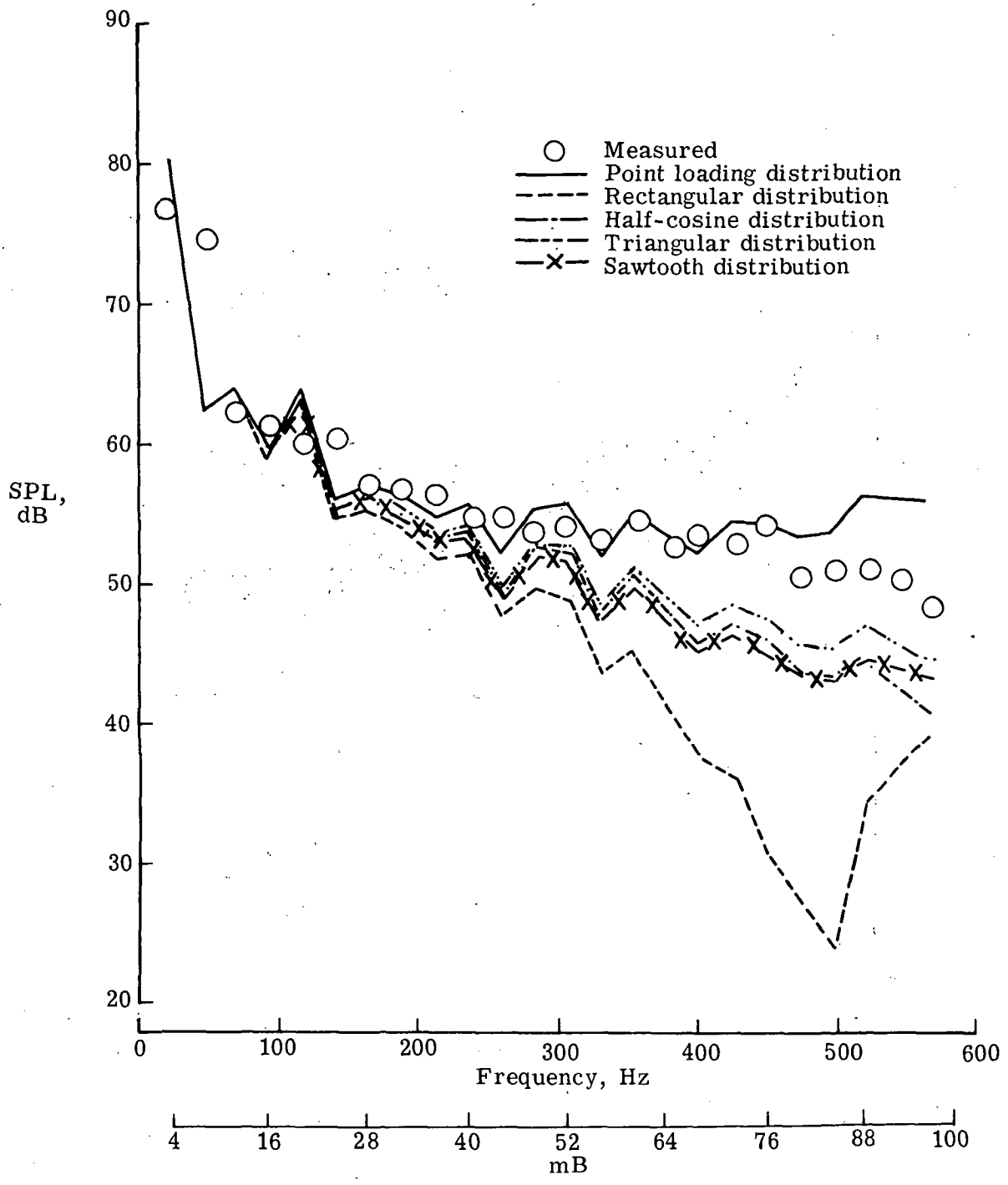

(a) Microphone position 2.

Figure 25.- The effect of various chordwise loading distributions on calculated rotational noise, obtained by using a 40 percent chord integrated loading spectrum.

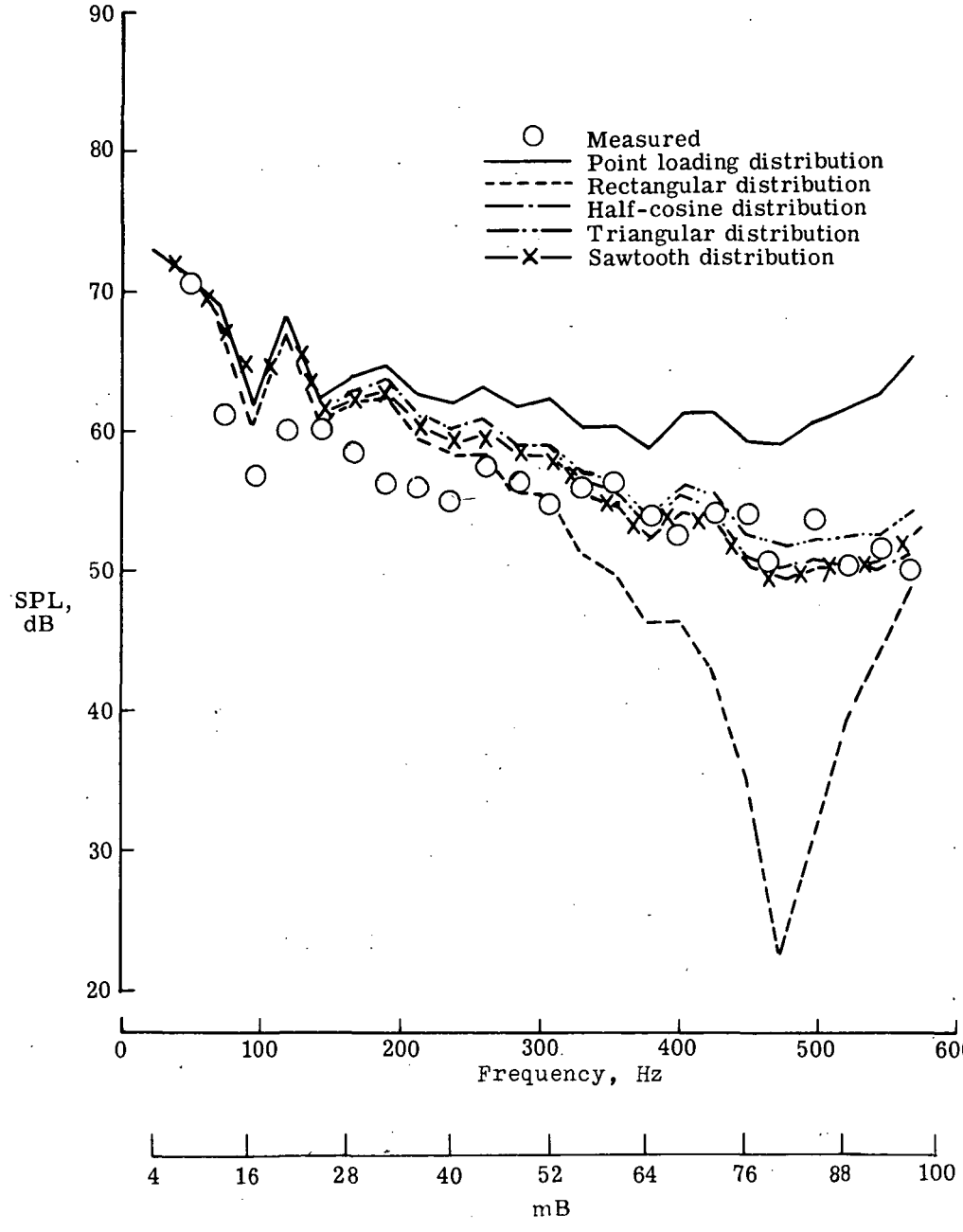

(b) Microphone position 1.

Figure 25.- Concluded.

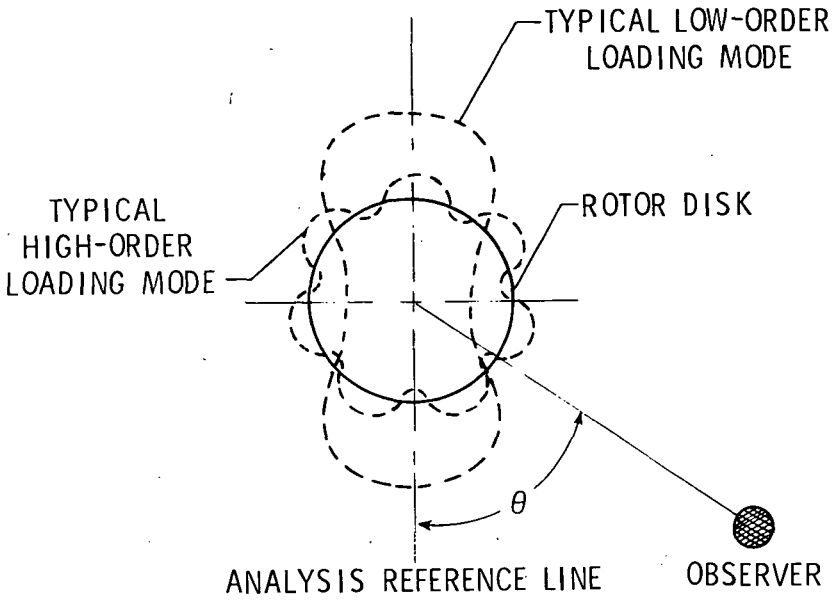

Figure 26.- Conceptual view of typical low-order and high-order blade loading modes and their orientation with respect to observer.

the low-order mode, it can be seen that the noise radiated would be greatly affected by a phase change of, say, $\pi/2$. The acoustic radiation from the high-order mode, however, can be expected to be much more nondirectional than for the low-order mode. Therefore, a phase change of $\pi/2$ would be expected to have little effect on its acoustic radiation pattern. It seems, then, that the blade loading phase and observer angles are most important in determining the level of the low-order sound harmonics.

In order to test this effect, the Fourier transform program described in reference 18 was used to compute the phases of the measured blade loading harmonics. The typical result, as shown in figure 27, was that the phase spectrum was concentrated in a band of $\pm 25^{\circ}$ about 0°. Four trial cases were then conducted for a typical test condition. Three of the four cases consisted of using arbitrary, but constant, phases for the α_S spectra; the fourth case used the actual measured α_S phase spectrum. The results from these four cases are presented in figure 28. Except for the first acoustic harmonic, all the calculated harmonics are coincident. This effect could be expected to spread to a few higher harmonics if the rotational speed were lower.

Final Calculation Results

Because the previously cited rotational noise calculations, based on 40-percent chordwise integrated, differential blade loading coefficients $(\alpha_{s,diff,int})$ and a point chordwise loading distribution $(\chi_{mB} = 1)$, seemed generally to provide the best agreement with

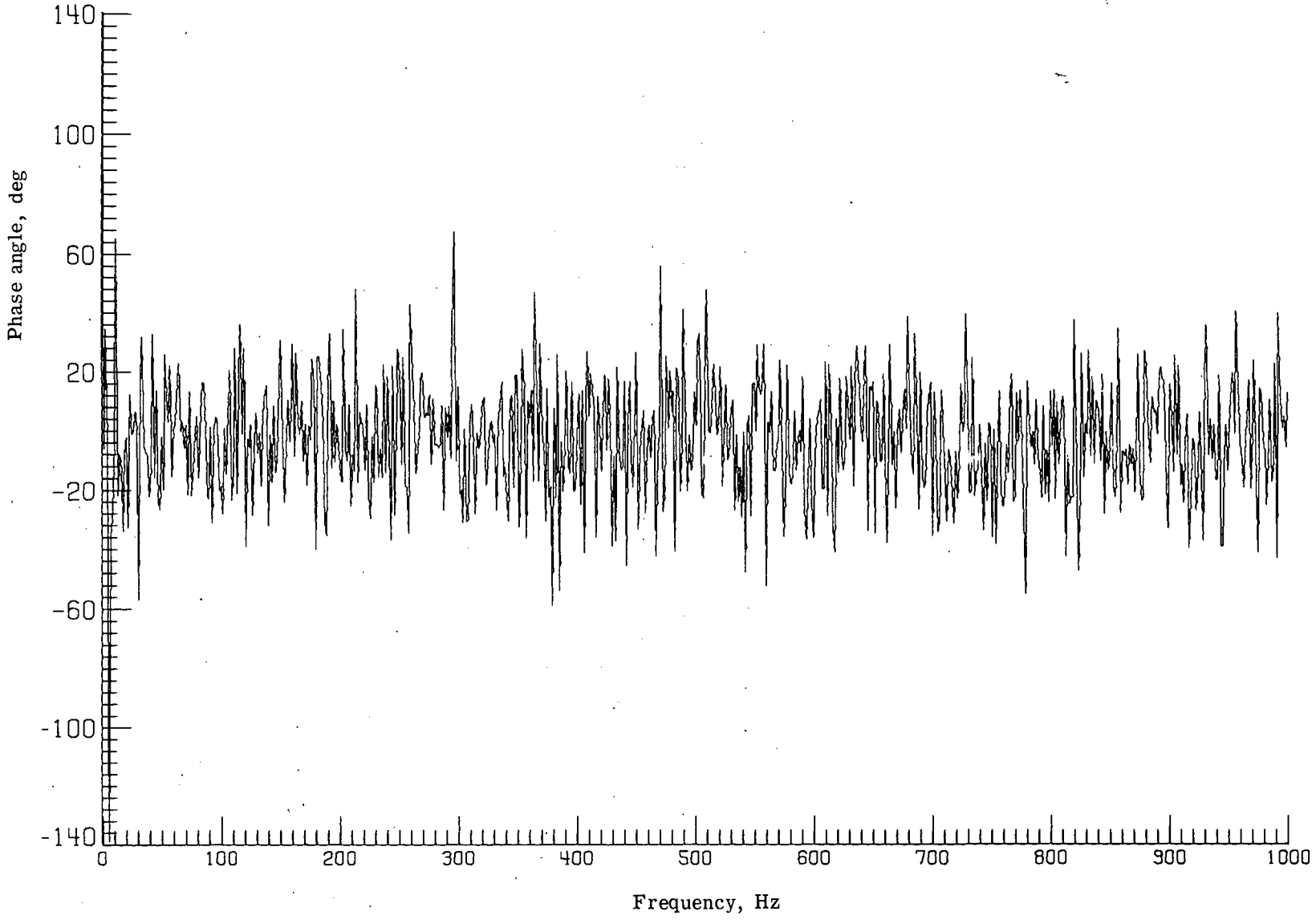

Figure 27.- Typical phase spectrum of measured blade loads.

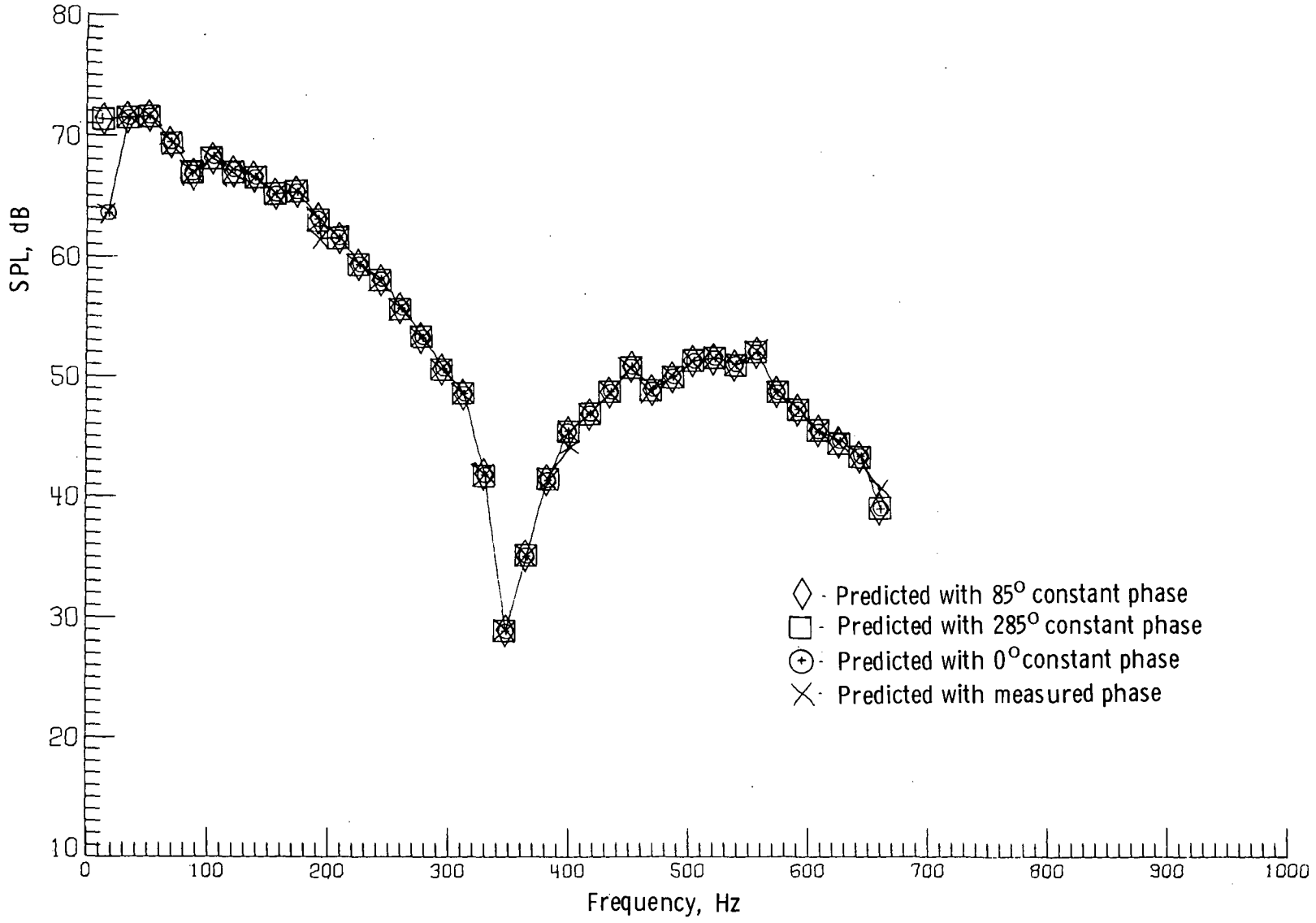

Figure 28.- The effect of absolute phases of blade loading harmonics on the radiated noise field, using a rectangular loading distribution.

measured noise, similar calculations were performed for all the conditions listed in table II. The resulting calculated and measured spectra at microphone positions 1 and 2 (see fig. 2) are displayed in figures 29(a) to 29(n). (In these figures the circles indicate the measured noise levels at frequencies mBN, harmonics of the blade passage frequencies. Therefore, at frequencies above the rotational-broadband transition range, they are not the rotational noise level.) Some general comments can be made regarding these results:

(1) The use of the point loading distribution and integrated blade loading coefficients is not to be construed as a criterion for rotational noise prediction. Their use in these calculations was strictly an engineering judgment since they seem to provide the best agreement with measured rotational noise most of the time.

(2) Generally, the calculated and measured rotational noise spectra show good agreement through 500 Hz. Beyond 500 Hz the calculated and measured spectra begin to diverge in most cases. This may be attributed to the fact that at these frequencies the compact source model begins to break down, that is, the criterion $\lambda_{mB}/2 < c$ is approached $\left(\frac{\lambda_{mB}}{2} = c \text{ at a frequency of } 523 \text{ Hz}\right)$. It is at these frequencies that the shape of the chordwise distribution becomes most important. In order to accurately calculate the rotational noise levels for $\frac{\lambda_{mB}}{2} < c$, it may be necessary to use a unique chordwise distribution for each blade loading coefficient $\alpha_{s,diff,int}$. Implementation of such a technique was beyond the scope of this work, although the information is implicit in the data.

(3) There are several examples (figs. 29(a), 29(b), and 29(h)) where the calculated and measured spectra diverge much below 500 Hz. This is not caused by a deficiency in the theory but seems to be a direct result of an early transition of the loading spectrum from discrete to broadband content.

(4) In a number of cases (figs. 29(a), 29(b), 29(g), 29(h), 29(j), 29(l), and 29(m)) the first-order harmonic is either under or over predicted by 7 to 14 dB. This is believed to be caused by the combined effect of small errors in the measurement of the blade observer angle θ and loading phases ϕ_s, plus a breakdown in the far-field approximations. The effect of θ and ϕ_s on the first-order harmonic amplitudes was discussed earlier. Because the microphone positions were 45.72 m (150 ft) from the rotor axis, even at the highest RPM tested they were only slightly more than three acoustic wavelengths away. This would put them on the boundary between the near field and far field. Thus, better agreement at the lowest acoustic harmonics may, in this case, require the use of near-field terms in the analysis.

(5) The generally good agreement between the measured and calculated rotational noise, based on loading measured at 80-percent span, suggests that the aerodynamic activity in that area is representative of the entire rotor system, at least as far as rotational-noise generation is concerned.

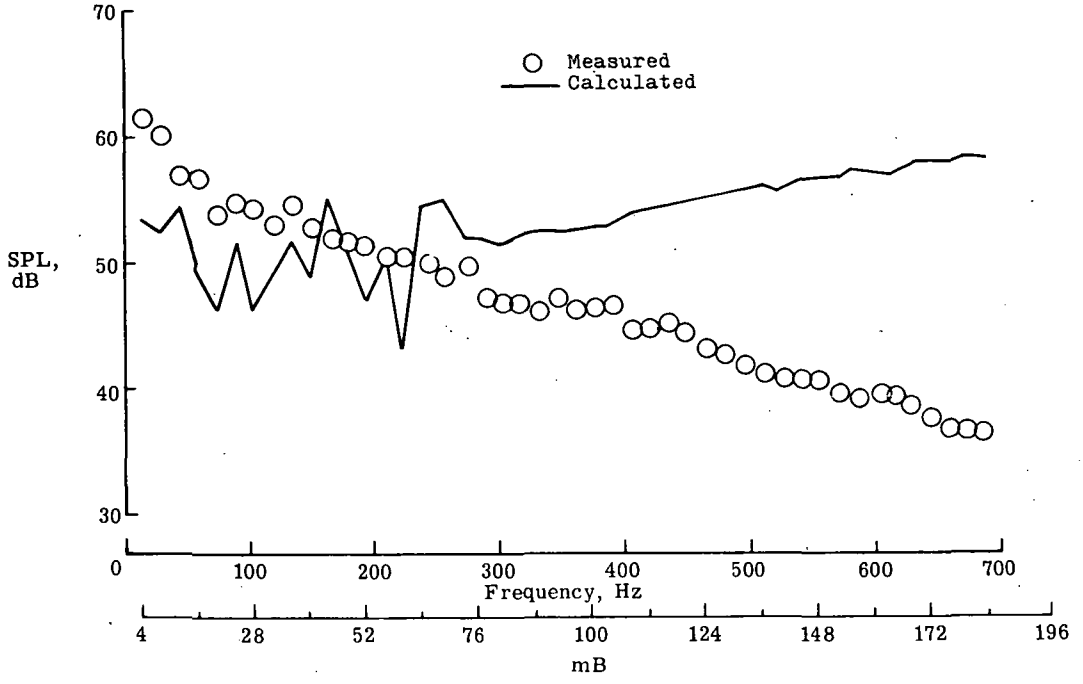

(a) rpm = 225; L_F = 14 612 N (3285 lb); $\overline{C}_L$ = 0.619; σ' = 0^o (microphone position 2).

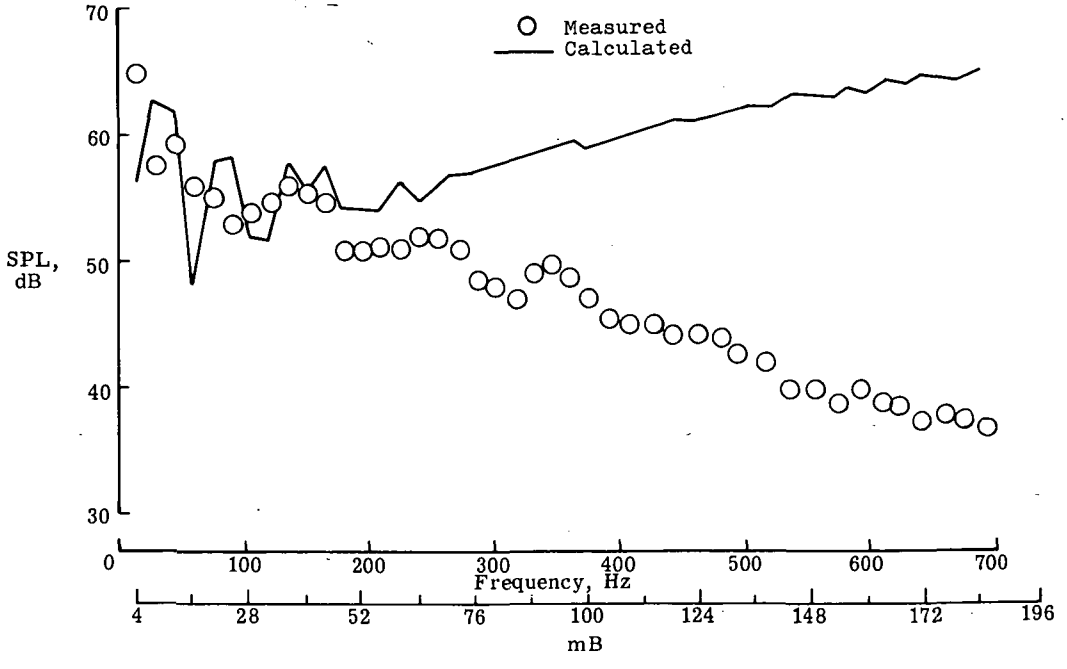

(b) rpm = 225; L_F = 14 612 N (3285 lb); $\overline{C}_L$ = 0.619; σ' = 11^o (microphone position 1).

Figure 29.- Comparison of calculated rotational noise, obtained by using 40-percent chordwise integrated blade loading coefficients and point loading distribution, with measured noise for all conditions listed in table II.

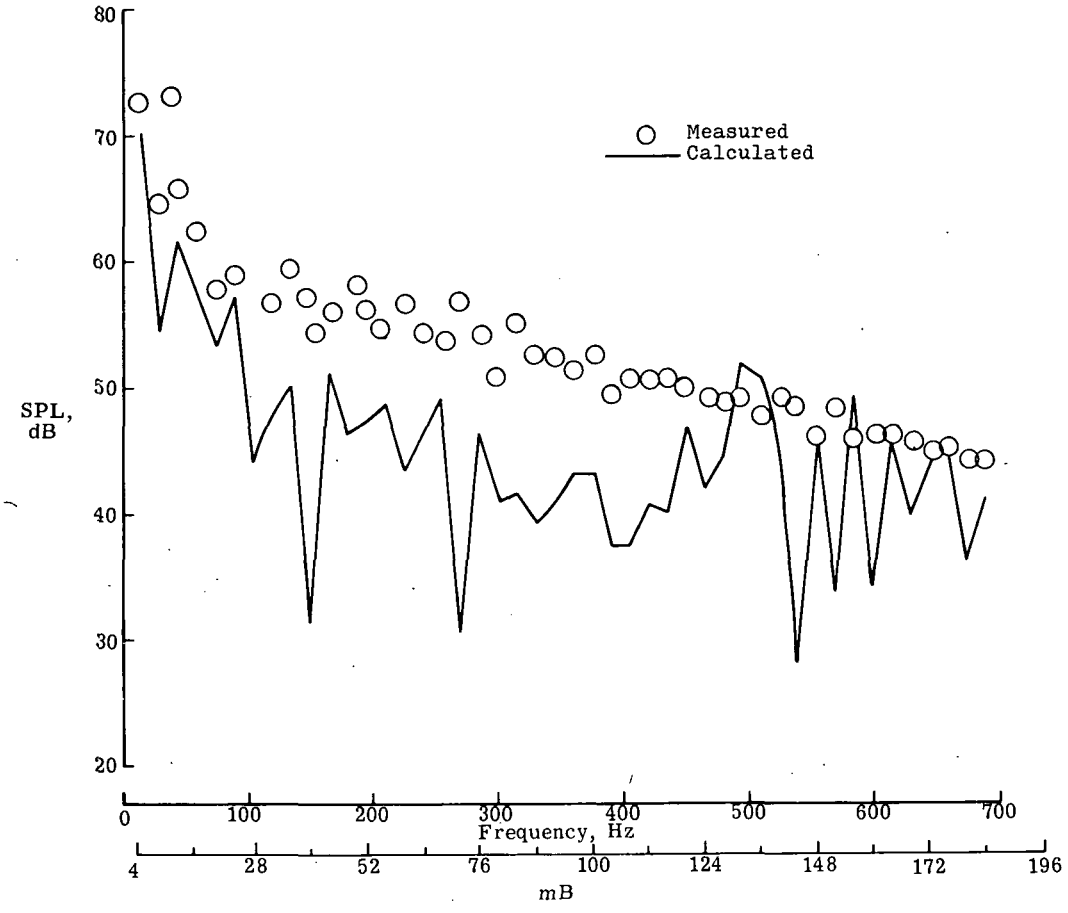

(c) rpm = 225; L_F = 22 743 N (5113 lb); $\overline{C}_L$ = 0.938; $\sigma' = 0^o$ (microphone position 2).

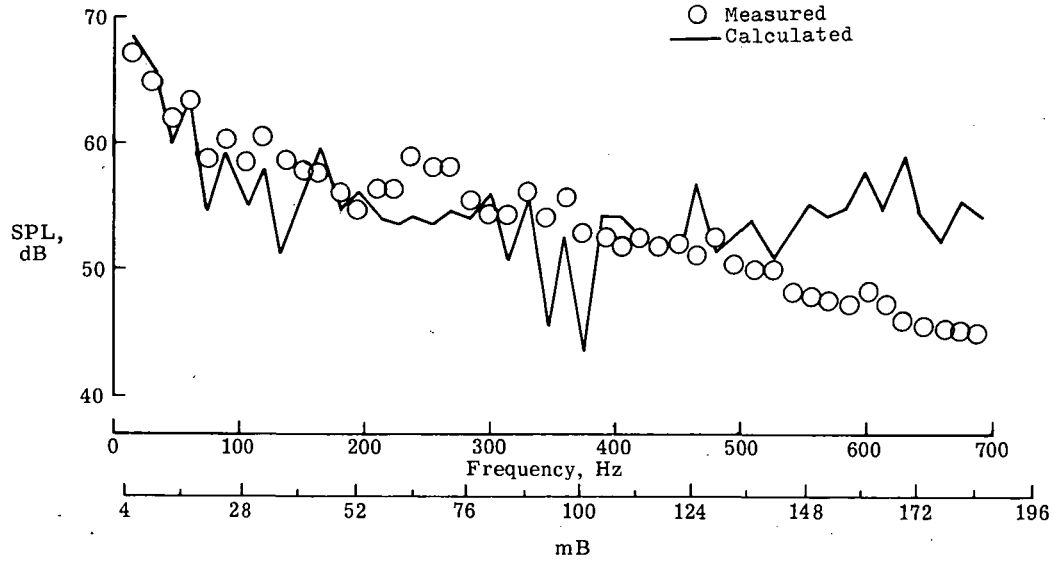

(d) rpm = 225; L_F = 22 743 N (5113 lb); $\overline{C}_L$ = 0.938; $\sigma' = 11^o$ (microphone position 1).

Figure 29.- Continued.

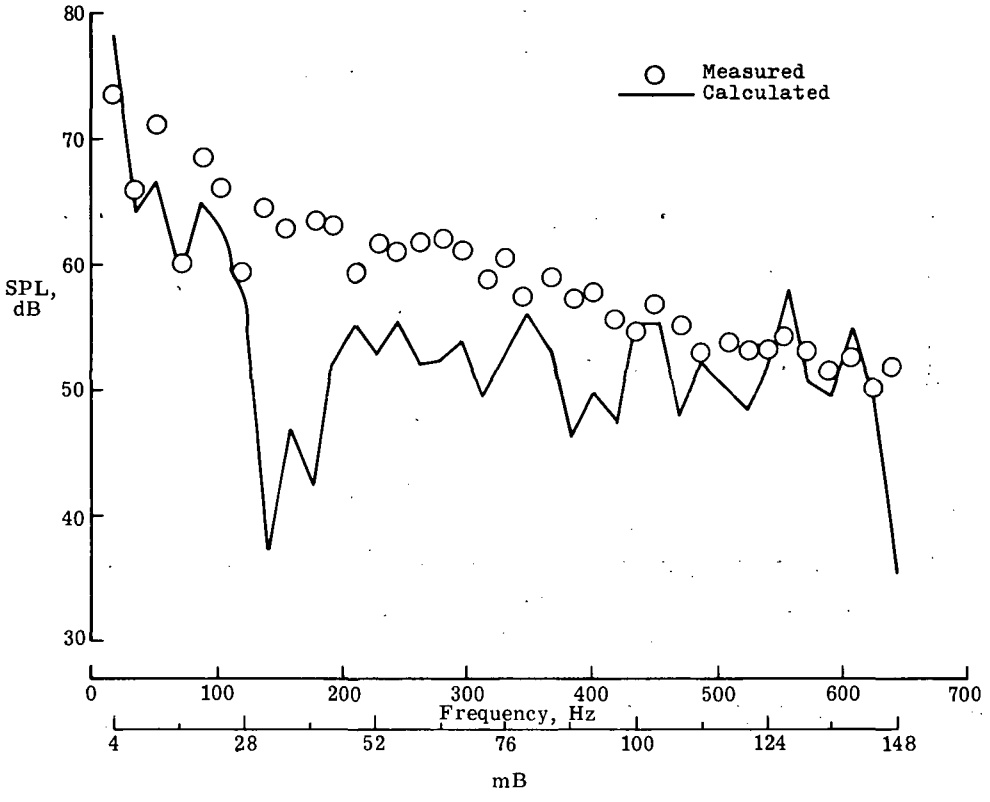

(e) rpm = 261; L_F = 31 714 N (7130 lb); $\overline{C}_L$ = 0.991; σ' = 0° (microphone position 2).

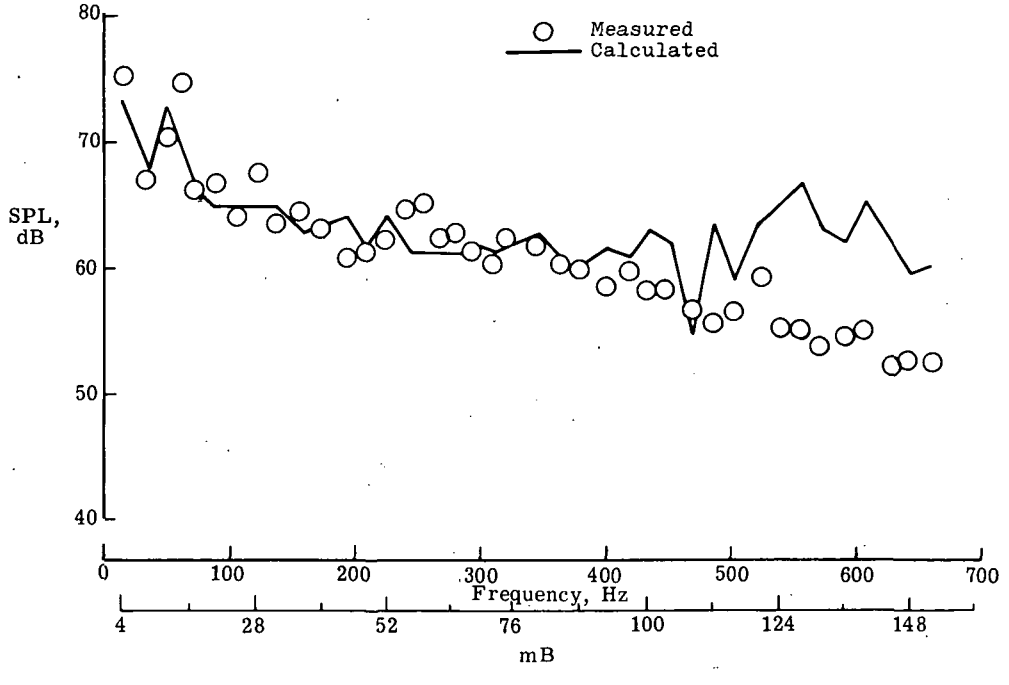

(f) rpm = 261; L_F = 31 714 N (7130 lb); $\overline{C}_L$ = 0.991; σ' = 11° (microphone position 1).

Figure 29.- Continued.

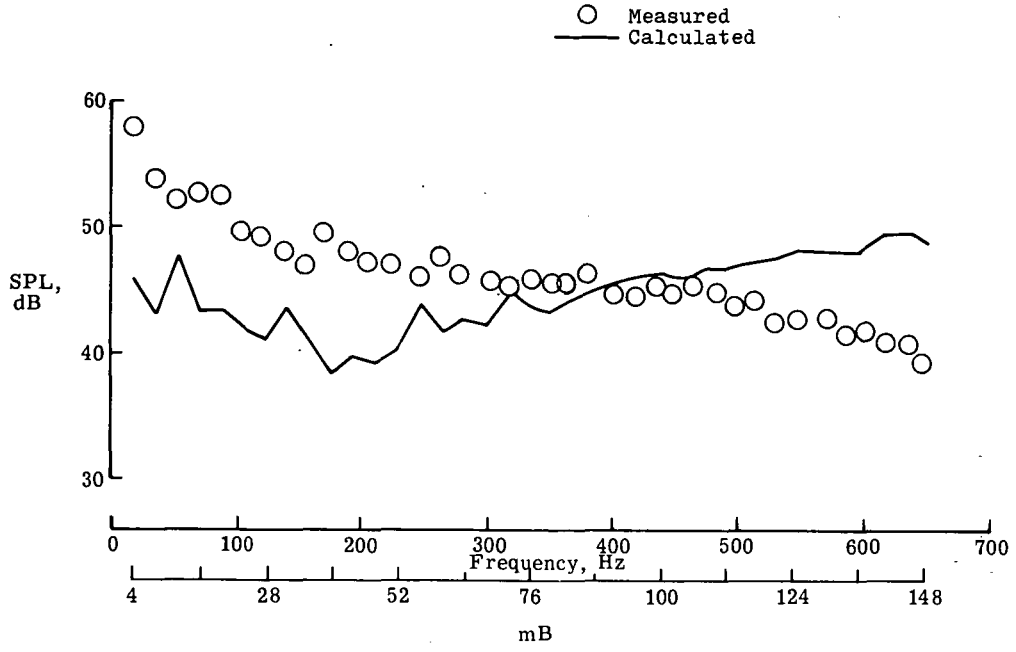

(g) rpm = 263; L_F = 6792 N (1527 lb); $\overline{C}_L$ = 0.210; σ' = 0° (microphone position 2).

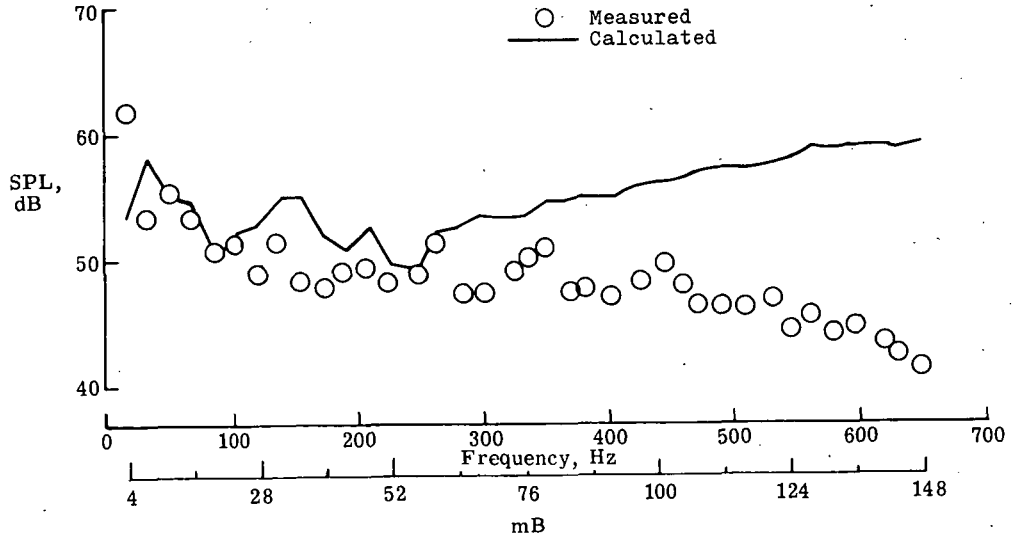

(h) rpm = 263; L_F = 6792 N (1527 lb); $\overline{C}_L$ = 0.210; σ' = 11° (microphone position 1).

Figure 29.- Continued.

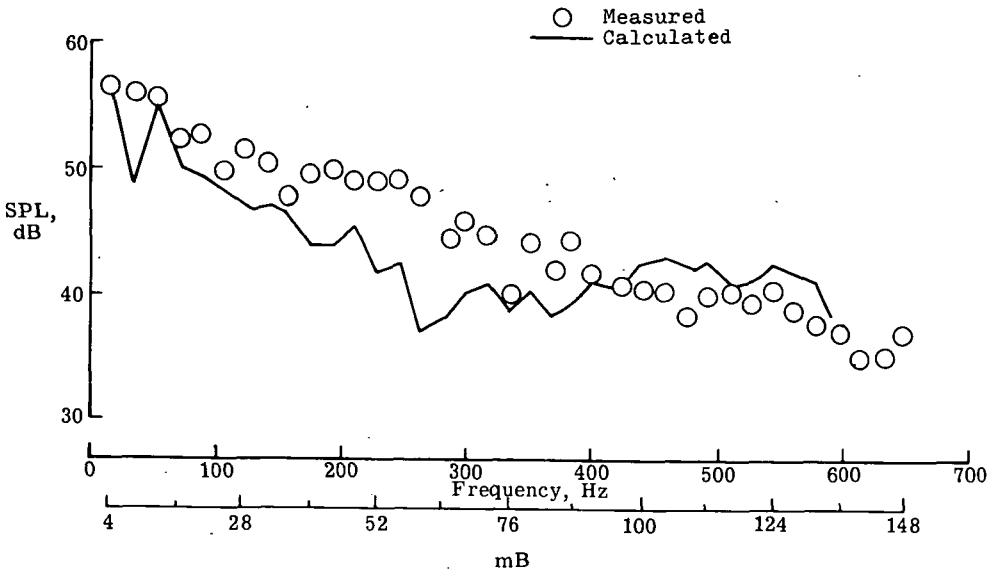

(i) rpm = 265; L_F = 12 530 N (2817 lb); $\overline{C}_L$ = 0.383; $\sigma' = 0^o$ (microphone position 2).

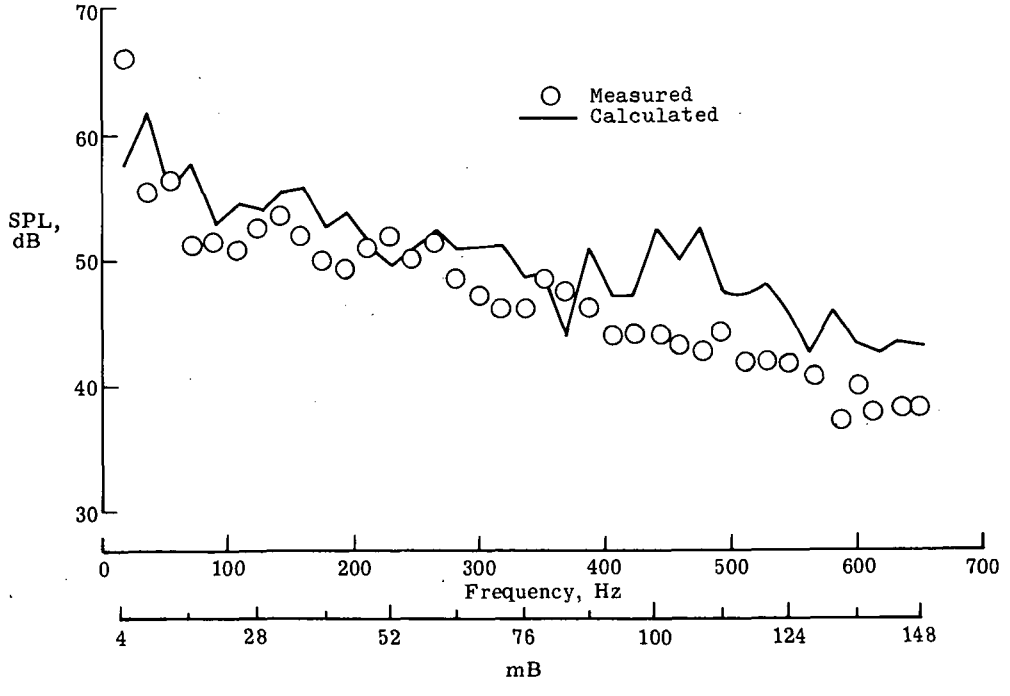

(j) rpm = 265; L_F = 12 530 N (2817 lb); $\overline{C}_L$ = 0.383; $\sigma' = 11^o$ (microphone position 1).

Figure 29.- Continued.

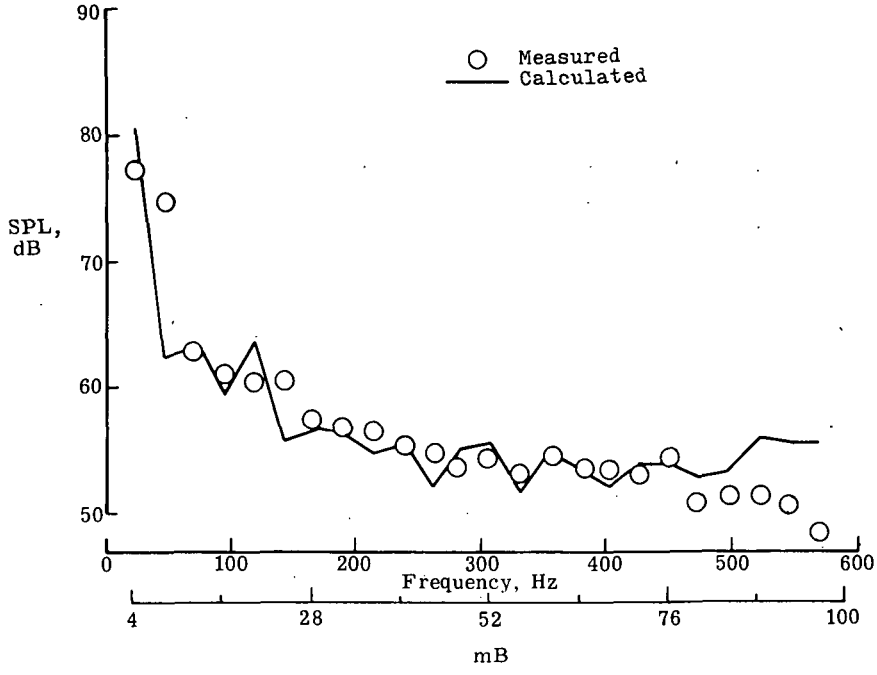

(k) rpm = 355; L_F = 18 553 N (4171 lb); $\overline{C}_L$ = 0.317; σ' = 0^o (microphone position 2).

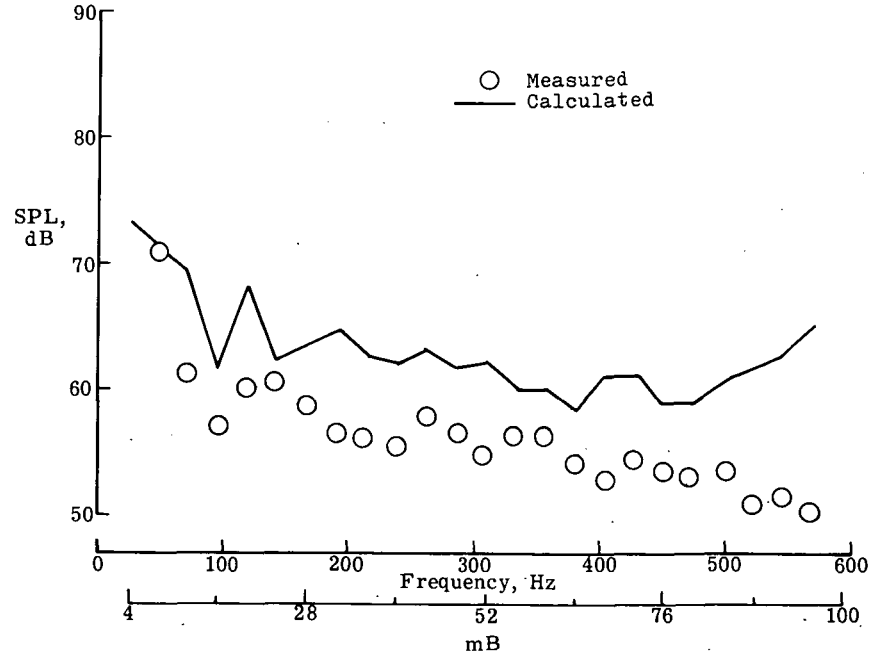

(l) rpm = 355; L_F = 18 553 N (4171 lb); $\overline{C}_L$ = 0.317; σ' = 11^o (microphone position 1).

Figure 29.- Continued.

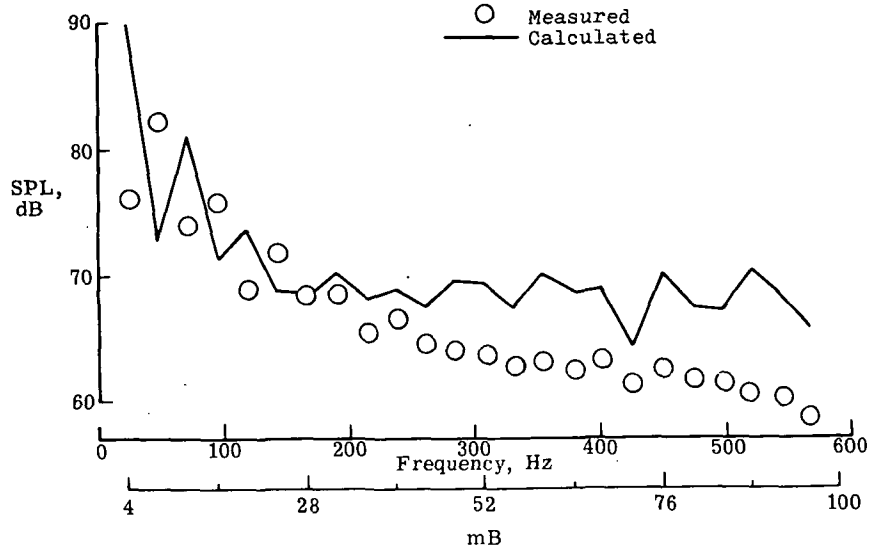

(m) rpm = 355; L_F = 44 613 N (10 030 lb); $\overline{C}_L$ = 0.759; σ' = 0° (microphone position 2).

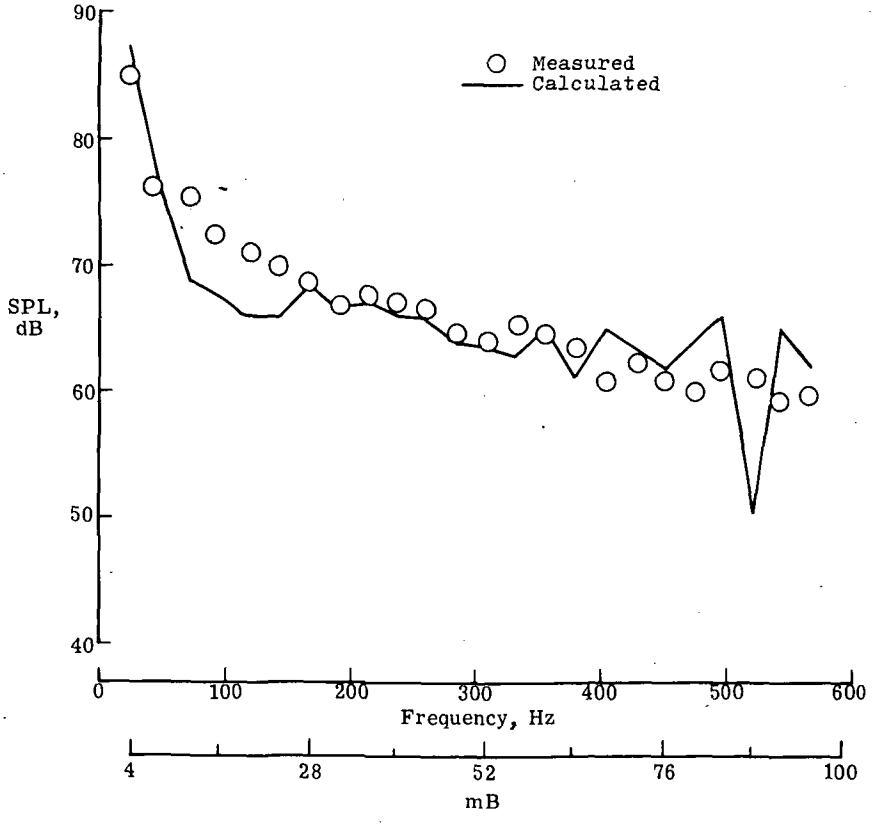

(n) rpm = 355; L_F = 44 613 N (10 030 lb); $\overline{C}_L$ = 0.759; σ' = 11° (microphone position 1).

Figure 29.- Concluded.

CONCLUDING REMARKS

In tests conducted at the Langley helicopter rotor test facility, simultaneous measurements were made of the fluctuating aerodynamic blade surface pressures and the radiated rotor noise. The measured fluctuating surface pressures were then used in Wright's theory to predict the rotational noise. Comparison of the predicted and measured rotational noise showed that the accuracy of the predictions was directly dependent on two things: the number of discrete loading harmonics measured and the chordwise distribution of these loads. In general, test conditions which generated a large number of loading harmonics and which were assumed distributed at a point provided good rotational-noise predictions through 500 to 600 Hz. Within 1 to 5 dB, this is evidence that the compact source assumptions were valid for the operating conditions studied. At higher tip speeds, more realistic loading distributions would probably have to be considered.

Examination of the measured blade pressures revealed that the upper and lower surface fluctuating pressures were quite similar in spectral amplitude and shape. Comparison of the spectra at different chordwise stations, however, showed that the forward chord position contained more pressure harmonics through higher frequencies (up to 500 Hz) than did spectra from aft chord positions. The overall rms pressures were also greater, nearly 1500 N/m^2 gage (0.217 psig), at forward chord positions. The aft chord positions generally contained more broadband pressures starting at lower frequencies (as low as 200 Hz) than did the forward chord positions. Because of their broadband content, pressures from the aft chord positions did not provide good rotational-noise prediction results.

Langley Research Center,
National Aeronautics and Space Administration,
Hampton, Va., October 9, 1974.

APPENDIX A

DERIVATION OF WRIGHT'S SOLUTION

This appendix presents a simplified derivation of the rotational noise equations developed in references 7 and 8 and outlined in the section "Rotor Rotational Noise Theory" of this report.

Generalized Solution of Wave Equation

The rotor and force coordinate systems are shown in figure 20. The wave equation to be solved is

$$\frac{1}{a_0^2}\frac{\partial^2 p}{\partial t^2} - \frac{\partial^2 p}{\partial x_i^2} = -\frac{\partial F_i}{\partial x_i}(\bar{x},t) \tag{A1}$$

where $F_i(\bar{x},t) = f_i(\bar{x},t)\delta(\bar{x}-\bar{y})$ is a general point force, $\bar{y} = \bar{y}(t)$, the bar denotes a vector, and $\delta(\ )$ is a Dirac delta function.

The solution to equation (A1) then is (from Lighthill, ref. 30)

$$p(\bar{x},t) = -\frac{1}{4\pi}\frac{\partial}{\partial x_i}\iiiint \frac{1}{|\bar{x}-\bar{y}_0|} f_i(\bar{y}_0,\tau)\,\delta(\bar{y}_0-\bar{y})\,\delta\left(\tau - t + \frac{|\bar{x}-\bar{y}_0|}{a_0}\right) d\tau\, d\bar{y}_0$$

$$= -\frac{1}{4\pi}\frac{\partial}{\partial x_i}\left[\frac{f_i(\bar{y}(t),t)}{D}\right] \tag{A2}$$

where $D = |\bar{x}-\bar{y}|$, and $[\ ]$ implies retarded time $t - D/a_0$. Therefore,

$$p(\bar{x},t) = -\frac{1}{4\pi D^2}(\bar{x}-\bar{y})\left[\frac{1}{a_0}\frac{\partial[\bar{f}]}{\partial t} + \frac{[\bar{f}]}{D}\right] \tag{A3}$$

Solution of Wave Equation for a Rotating Point Force

A rotating point force distribution can be modeled as follows:

$$\bar{f}(\bar{y}(t),t) = \bar{f}_{0\eta}(r)\exp\left[j(\eta\Omega t - \xi\psi - \phi)\right] \tag{A4}$$

where η and ξ are arbitrary phase constants.

Hence, the radiated sound pressure for each η is:

$$SP_\eta = \frac{-(\bar{x} - \bar{y})}{4\pi D^2} \bar{f}_{0\eta} \left(\frac{j\eta\Omega}{a_0} + \frac{1}{D} \right) \exp\left\{ j\left[\eta\Omega\left(t - \frac{D}{a_0} \right) - \xi\psi - \phi \right] \right\} \tag{A5}$$

From figure 20,

$$D = \left[R^2 + r^2 - 2Rr \cos\sigma' \cos(\theta - \psi) \right]^{\frac{1}{2}}$$

$$\bar{f}_{0\eta} = \left| \bar{f}_{0\eta} \right| \left[\bar{x}_1(-\sin\beta \sin\psi), \bar{x}_2(\sin\beta \cos\psi), \bar{x}_3(-\cos\beta) \right]$$

where $\bar{x}_1$, $\bar{x}_2$, $\bar{x}_3$ are unit vectors in the x_1, x_2, x_3 directions, respectively. Now $\bar{y} \cdot \bar{f}_{0\eta} = 0$ because $\bar{f}_0$ acts in the plane normal to $\bar{y}$. Therefore,

$$(\bar{x} - \bar{y}) \cdot \bar{f}_{0\eta} = \bar{x} \cdot \bar{f}_{0\eta} = -R\left| \bar{f}_{0\eta} \right| \left[\sin\beta \cos\sigma' \sin(\psi - \theta) + \sin\sigma' \cos\beta \right]$$

The sound radiation from a force system distributed over the rotor disk is determined by letting $\left| \bar{f}_{0\eta}(r) \right| = P_\eta(r) \left| d\bar{A} \right| = P_\eta(r) r \, dr \, d\psi$, which yields, for the radiation from the entire disk,

$$SP_\eta = \int_0^{2\pi} \int_0^{r_t} - \frac{R}{4\pi D^2} P_\eta(r) \left[\sin\beta \cos\sigma' \sin(\psi - \theta) + \cos\beta \sin\sigma' \right]$$

$$\left(\frac{j\eta\Omega}{a_0} + \frac{1}{D} \right) \exp\left\{ j\left[\eta\Omega\left(t - \frac{D}{a_0} \right) - \xi\psi - \phi \right] \right\} r \, dr \, d\psi \tag{A6}$$

The following simplifications are made in the analysis at this stage. In order to simplify the integration procedures, the observer azimuthal θ is assumed to be zero since it will amount to only a phase shift in the final solution. It is assumed that the observer is in the far field. That is, $D \rightarrow R$ everywhere except in the phase term where $D \approx R - r \cos\sigma' \cos\psi$.

In addition, the following results are used:

$$\int_0^{2\pi} \exp\left[j(z \cos \psi - \eta\psi)\right] d\psi = 2\pi j^{\eta} J_{\eta}(z)$$

$$\int_0^{2\pi} \sin \psi \exp\left[j(z \cos \psi - \eta\psi)\right] d\psi = -\frac{\eta}{z} 2\pi(-j)^{\eta} J_{\eta}(z)$$

Hence the sound pressure reduces to

$$SP_{\eta} = |\bar{A}| \int_0^{r_t} rP_{\eta}(r)\left(\cos \beta \sin \sigma' - \frac{a_0 \xi}{\eta\Omega r} \sin \beta\right) 2\pi(-j)^{\xi} J_{\xi}\left(\frac{\eta\Omega}{a_0} r \cos \sigma'\right) dr \quad (A7)$$

where $|\bar{A}| = -\frac{j\eta\Omega}{4\pi R a_0} \exp\left[j\eta\Omega\left(t - \frac{R}{a_0}\right)\right] \exp(-j\phi)$.

If it is assumed that the loading is concentrated over Δr at an effective radius r_e and Δr is small enough for J_{ξ} to be constant over Δr, then

$$SP_{\eta} = \frac{\eta\Omega}{2Ra_0} \exp\left\{j\left[\eta\Omega\left(t - \frac{R}{a_0}\right) - \phi\right]\right\} r_e P_{\eta}(r_e) \Delta r \left(\cos \beta \sin \sigma' - \sin \beta \frac{\xi}{\eta M_e}\right) J_{\xi}(\eta M_e \cos \sigma')(-j)^{\xi+1} \quad (A8)$$

The solution (A8) is for the sound radiation from a general pressure pattern, $P_{\eta}(r_e)\exp\left[j(\eta\Omega t - \xi\psi - \phi)\right]$. The helicopter rotational-noise equations are developed along the same lines. All that remains to be done is to model the forces on the rotor disk. These forces are composed of uniform and fluctuating components.

Uniform rotating forces.- For a helicopter the time history of the uniform rotating pressure pattern is as shown in figure 30. For ease of understanding, a rectangular distribution over the chord at $r = r_e$ is shown, although any distribution can be used. This distribution can be represented as

$$f(t) = \sum_{k=-\infty}^{\infty} C_k \exp\left[j(kB\Omega t - kB\psi)\right] \quad (A9)$$

where

$$C_k = \frac{LB}{\pi r_e} \chi_k$$

and

$$\chi_k = \text{Chord spectrum function} = \frac{\sin kBc/2r_e}{kBc/2r_e}$$

for a rectangular distribution.

Wright uses simple chord distribution functions such as rectangular, triangular, and half cosine in his theoretical development. For a particular sound harmonic m, the blade pressure mode of interest is

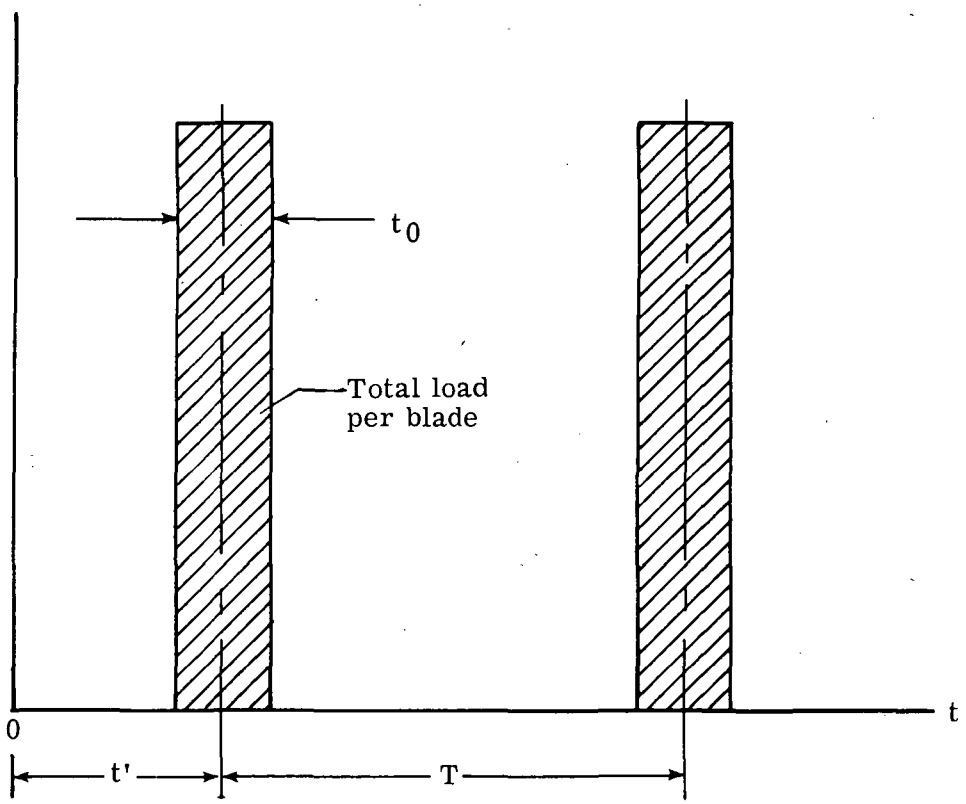

Figure 30.- Uniform rectangular force f(t) distribution seen by an observer on the fluid in the rotor plane at position $\bar{y}$; $f(t) = C_0 + \sum C_m \cos(mB\Omega t - mB\Omega t')$; $C_m = \frac{LB}{\pi r_e} \chi_{mB}$; $T = \frac{2\pi}{B\Omega}$; $t' = \frac{\psi}{\Omega}$; $t_0 = \frac{c}{\Omega r_e}$.

$$P_{mB} = \underline{P}_{mB} \exp\left[j(mB\Omega t - mB\psi)\right] \tag{A10}$$

where $\underline{P}_{mB} = \frac{LB}{\pi r_e} \chi_{mB}$ and $\underline{P}_{mB}$ is independent of ψ for uniform forces.

Fluctuating forces.- For fluctuating pressures, $\underline{P}_{mB}$ is dependent on ψ, that is,

$$P_{mB} = \underline{P}_{mB}(\psi) \exp\left[j(mB\Omega t - mB\psi)\right]$$

If the fluctuating pressures are constrained to have only periodic components,

$$\underline{P}_{mB}(\psi) = \sum_{s=-\infty}^{\infty} \underline{P}_{mB,s} \exp\left[j(s\psi - \phi_s)\right]$$

$$= \underline{P}_{mB} + \sum_{s=1}^{\infty} \underline{P}_{mB,s} \exp\left[j(s\psi - \phi_s)\right] + \sum_{s=-1}^{-\infty} \underline{P}_{mB,s} \exp\left[j(s\psi - \phi_s)\right]$$

$$= \underline{P}_{mB}\left(1 + \sum_{s=1}^{\infty} \frac{\alpha_s}{2} \left\{\exp\left[j(s\psi - \phi_s)\right] + \exp\left[-j(s\psi - \phi_s)\right]\right\}\right) \tag{A11}$$

where

$$\underline{P}_{mB} = \frac{LB}{\pi r_e} \chi_{mB}$$

$$\underline{P}_{mB,s} = \underline{P}_{mB} \alpha_s$$

$$\alpha_s = \frac{P_s}{P_0}$$

$$\phi_s = -\phi_{-s}$$

$$\underline{P}_{mB,-s} = \underline{P}_{mB,s}$$

The pressure pattern for a particular sound harmonic mB and loading harmonic s, is

represented as

$$P_{mB} = \underline{P}_{mB} \frac{\alpha_s}{2} \left\{ \exp\left[j(mB\Omega t - q_- \psi - \phi_s) \right] + \exp\left[j(mB\Omega t - q_+ \psi + \phi_s) \right] \right\} \quad \text{(A12)}$$

where

$$q_\pm = mB \pm s \quad \text{(A13)}$$

Comparing equation (A12) with the general pressure pattern P_η gives

$$\eta = mB$$

$$\xi = q_\pm$$

$$P_\eta(r_e) = \frac{LB\alpha_s}{2\pi r_e} \chi_{mB}$$

$$\phi = \phi_s$$

Hence, neglecting all phase terms, the sound radiation from a particular blade loading harmonic s is

$$\underline{SP}_{mB,s} = \frac{\alpha_s \Omega \chi_{mB}}{2Ra_0} LB\ \Delta r \left[\left(\cos\beta \sin\sigma' - \frac{q_-}{mBM_e} \sin\beta \right) mBJ_{q_-}(mBM_e \cos\sigma') \right.$$

$$\left. + \left(\cos\beta \sin\sigma' - \frac{q_+}{mBM_e} \sin\beta \right) mBJ_{q_+}(mBM_e \cos\sigma') \right] \quad \text{(A14)}$$

Now, $LB\ \Delta r = L_T$, $L_F = L_T \cos\beta$ is the total rotor lift force, and $D_F = L_T \sin\beta$ is the total rotor drag force. Hence,

$$\underline{SP}_{mB,s} = \frac{\alpha_s}{2} \chi_{mB} \left[\left(K_L - K_D \frac{q_-}{mB} \right) \gamma_{q_-} + \left(K_L - K_D \frac{q_+}{mB} \right) \gamma_{q_+} \right] \quad \text{(A15)}$$

where $K_L = \frac{N}{Ra_0} L_F \sin\sigma'$, $K_D = \frac{N}{Ra_0} \frac{D_F}{M_e}$, $N = \frac{\Omega}{2\pi}$, $\gamma_q = mBJ_q(mBM_e \cos\sigma')$, and $\alpha_s = \frac{P_s}{P_0}$. Equation (A15) is the sound radiation from a particular loading harmonic s; it

does not include any phase terms. If all the phase terms are included, equation (A15) then becomes

$$SP_{mB,s} = \frac{\alpha_s}{2} \chi_{mB} \exp\left[jmB\Omega\left(t - \frac{R}{a_0}\right)\right] \left\{\left(K_L - \frac{K_D q_-}{mB}\right)\gamma_{q_-}\left(-j^{q_-+1}\right)\exp\left[j(q_-\theta - \phi_s)\right]\right.$$

$$\left. + \left(K_L - \frac{K_D q_-}{mB}\right)\gamma_{q_+}\left(-j^{q_++1}\right)\exp\left[j(q_+\theta + \phi_s)\right]\right\}$$

$$= \underline{SP}_{mB,s} \exp\left[jmB\Omega\left(t - \frac{R}{a_0}\right)\right] \tag{A16}$$

For convenience, θ was equated to zero earlier in the analysis. As mentioned earlier, θ provides a phase shift of $q\theta$. For multiple blade harmonic radiation, that is, radiation due to all blade loading harmonics, the sound pressure at a particular sound harmonic mB is then

$$SP_{mB} = \sum_{s=0}^{\infty} SP_{mB,s}$$

$$= \exp\left[jmB\Omega\left(t - \frac{R}{a_0}\right)\right] \sum_{s=0}^{\infty} \underline{SP}_{mB,s} \tag{A17}$$

Now,

$$\sum_{s=0}^{\infty} \underline{SP}_{mB,s} = \sum_{s=0}^{\infty} \frac{\alpha_s}{2} \chi_{mB} \left\{\left(K_L - \frac{K_D q_-}{mB}\right)\gamma_{q_-} \exp\left[j(q_-\theta - \phi_s)\right]\left(-j^{q_-+1}\right)\right.$$

$$\left. + \left(K_L - \frac{K_D q_+}{mB}\right)\gamma_{q_+} \exp\left[j(q_+\theta + \phi_s)\right]\left(-j^{q_++1}\right)\right\} \tag{A18}$$

Substituting q for s as given by equation (A13) yields

$$\sum_{s=0}^{\infty} \underline{SP}_{mB,s} = \chi_{mB} \sum_{q=mB}^{-\infty} \frac{\alpha_{mB-q}}{2}\left(K_L - \frac{K_D q}{mB}\right)\gamma_q \exp\left[j\left(q\theta - \phi_{mB-q}\right)\right]\left(-j^{q+1}\right)$$

$$+ \chi_{mB} \sum_{q=mB}^{\infty} \frac{\alpha_{q-mB}}{2}\left(K_L - \frac{K_D q}{mB}\right)\gamma_q \exp\left[j\left(q\theta + \phi_{q-mB}\right)\right]\left(-j^{q+1}\right) \qquad \text{(A19)}$$

Rearranging the terms in equation (A19) gives

$$\sum_{s=0}^{\infty} \underline{SP}_{mB,s} = \frac{\alpha_0}{2}\chi_{mB}\left(K_L - K_D\right)\gamma_{mB} \exp\left[j\left(mB\theta - \phi_0\right)\right]\left(-j^{mB+1}\right)$$

$$+ \frac{\alpha_{mB}}{2}\chi_{mB}\left(K_L\gamma_0\right)\exp\left(-j\phi_{mB}\right)(-j)$$

$$+ \sum_{q=1}^{\infty} \frac{\alpha_{|q-mB|}}{2}\chi_{mB}\left(K_L - \frac{K_D q}{mB}\right)\gamma_q \exp\left\{j\left[q\theta + \left(2S_q - 1\right)\phi_{|q-mB|}\right]\right\}\left(-j^{q+1}\right)$$

$$+ \sum_{q=-1}^{-\infty} \frac{\alpha_{|mB-q|}}{2}\chi_{mB}\left(K_L - \frac{K_D q}{mB}\right)\gamma_q \exp\left[j\left(q\theta + \phi_{|mB-q|}\right)\right]\left(-j^{q+1}\right) \qquad \text{(A20)}$$

where

$$S_q = 0 \quad \text{for} \quad q < mB$$

$$S_q = 1 \quad \text{for} \quad q \geq mB$$

The final result is obtained by substituting equation (A20) into equation (A17) after reversing the order of summation in the last term.

$$SP_{mB} = \exp\left[jmB\Omega\left(t - \frac{R}{a_0}\right)\right] \chi_{mB}\left[\frac{\alpha_0}{2}\left(K_L - K_D\right)\gamma_{mB} \exp\left[j\left(mB\theta - \phi_0\right)\right]\left(-j^{mB+1}\right)\right.$$

$$+ \frac{\alpha_{mB}}{2} K_L \gamma_0 \exp\left(-j\phi_{mB}\right)(-j)$$

$$+ \sum_{q=1}^{\infty}\left(\frac{\alpha_{|q-mB|}}{2}\left(K_L - K_D \frac{q}{mB}\right)\gamma_q \exp\left\{j\left[q\theta + \left(2S_q - 1\right)\phi_{|q-mB|}\right]\right\}\right.$$

$$\left.\left. + \frac{\alpha_{mB+q}}{2}\left(K_L + K_D \frac{q}{mB}\right)\gamma_q \exp\left[-j\left(q\theta - \phi_{|mB+q|}\right)\right]\right)\left(-j^{q+1}\right)\right] \qquad \text{(A21)}$$

APPENDIX B

DETERMINATION OF OBSERVER AZIMUTH ANGLE

The following experimental method was used to determine the blade-observer angle θ. During data acquisition, a blade-position indicator was recorded on tape. The indicator consisted of a large pulse followed by three smaller pulses (fig. 31(a)). The large pulse indicated when the instrumented blade passed a fixed point on the rotor disk plane. The smaller pulses divided the blade path into quadrants.

Let point A (fig. 31(b)) be a fixed point on the disk plane and let M be the microphone (observer) position. Then, θ' is the angle between lines OA and OB corresponding to t' in the rotor plane, and ϕ is the angle between lines OA and OM. Point B represents the time at which data sampling for Fourier analysis was stated. Then, the value of θ, the blade-observer angle at the onset of data analysis, is

$$\theta = \phi - \theta'$$

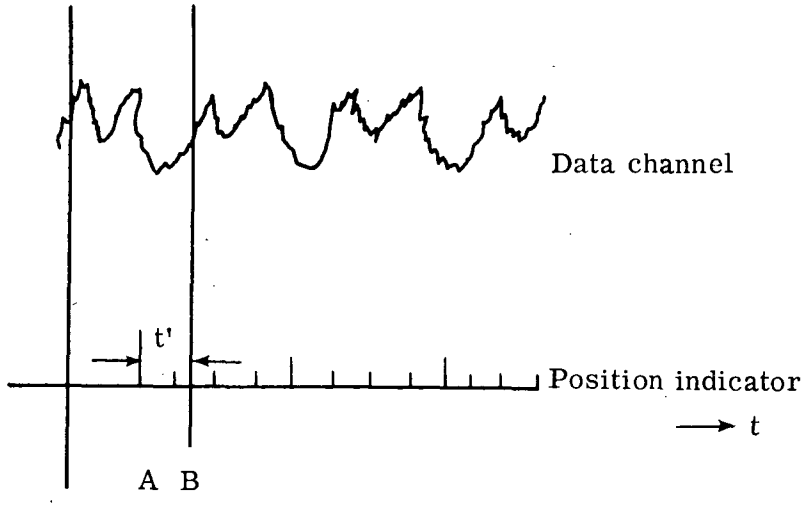

(a) Sample oscillograph record. (t' is defined in eq. 31(b).)

Figure 31.- Determination of θ, the blade-observer azimuthal angle.

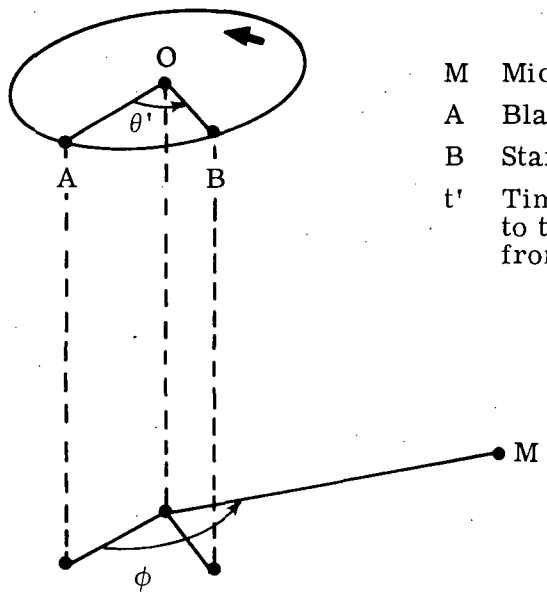

M Microphone position
A Blade position marker
B Starting point for data
t' Time taken for the blade to travel an angle θ' from A to B

(b) Observer orientation.

Figure 31.- Concluded.

REFERENCES

1. Gutin, L.: On the Sound Field of a Rotating Propeller. NACA TM 1195, 1948.

2. Lowson, M. V.: Basic Mechanisms of Noise Generation by Helicopters, V/STOL Aircraft and Ground Effect Machines. J. Sound & Vib., vol. 3, no. 3, May 1966, pp. 454-466.

3. Lowson, M. V.; and Ollerhead, J. B.: Studies of Helicopter Rotor Noise. USAAVLABS Tech. Rep. 68-60, U.S. Army, Jan. 1969.

4. Schlegel, Ronald G.; King, Robert; and Mull, Harold: Helicopter Rotor Noise Generation and Propagation. USAAVLABS Tech. Rep. 66-4, U.S. Army, Oct. 1966.

5. Schlegel, Ronald G.; and Bausch, William E.: Helicopter Rotor Rotational Noise Prediction and Correlation. Volume 1 – Rotational Noise Prediction and Correlation Under Nonuniform Inflow Conditions. USAAVLABS Tech. Rep. 70-1A, U.S. Army, Nov. 1970.

6. Bausch, W. E.; Munch, C. L.; and Schlegel, R. G.: An Experimental Study of Helicopter Rotor Impulsive Noise. USAAVLABS Tech. Rep. 70-72, U.S. Army, June 1971.

7. Wright, S. E.: Sound Radiation From a Lifting Rotor Generated by Asymmetric Disk Loading. J. Sound & Vib., vol. 9, no. 2, Mar. 1969, pp. 223-240.

8. Wright, S. E.: Discrete Radiation From Rotating Periodic Sources. J. Sound & Vib., vol. 17, no. 4, Aug. 22, 1971, pp. 437-498.

9. Stickle, George W.; and Batten, Bobby G.: STOL Transport Parameters (Military and Commercial) With Special Emphasis on Noise. TAC OA TR-70-17, U.S. Air Force, May 1971. (Available from DDC as AD 729 184.)

10. Sadler, S. Gene; and Loewy, Robert G: A Theory for Predicting the Rotational and Vortex Noise of Lifting Rotors in Hover and Forward Flight. NASA CR-1333, 1969.

11. Scheiman, James: A Tabulation of Helicopter Rotor-Blade Differential Pressures, Stresses, and Motion as Measured in Flight. NASA TM X-952, 1964.

12. Johnson, H. Kevin: Development of a Technique for Realistic Prediction and Electronic Synthesis of Helicopter Rotor Noise. USAAMRDL Tech. Rep. 73-8, U.S. Army, Mar. 1973.

13. Ramakrishnan, Ramani: On Discrete Noise Radiation From Helicopters. M.S. Thesis, George Washington Univ., Sept. 1973.

14. Hubbard, H. H.; Lansing, D. L.; and Runyan, H. L.: A Review of Rotating Blade Noise Technology. J. Sound & Vib., vol. 19, no. 3, Dec. 8, 1971, pp. 227-249.

15. Bartsch, E. A.: In-Flight Measurement and Correlation With Theory of Blade Airloads and Responses on the XH-51A Compound Helicopter Rotor. Volume I – Measurement and Data Reduction of Airloads and Structural Loads. USAAVLABS Tech. Rep. 68-22A, U.S. Army, May 1968.

16. Bartsch, E. A.: In-Flight Measurement and Correlation With Theory of Blade Airloads and Responses on the XH-51A Compound Helicopter Rotor. Volume II – Measurement and Data Reduction of Airloads and Structural Loads: Appendixes V Through IX. USAAVLABS Tech. Rep. 68-22B, U.S. Army, May 1968. (Available from DDC as AD 674 194.)

17. Sweers, J. E.: In-Flight Measurement and Correlation With Theory of Blade Airloads and Responses on the XH-51A Compound Helicopter Rotor. Volume III – Theoretical Prediction of Airloads and Structural Loads and Correlation With Flight Test Measurements. USAAVLABS Tech. Rep. 68-22C, U.S. Army, May 1968. (Available from DDC as AD 674 195.)

18. Brown, Thomas J.; Brown, Christine G.; and Hardin, Jay C.: Program for the Analysis of Time Series. NASA TM X-2988, 1974.

19. Reinsch, Christian H.: Smoothing by Spline Functions. II. Numer. Math., Bd. 16, Heft 5, 1971, pp. 451-454.

20. Hildebrand, F. B.: Introduction to Numerical Analysis. McGraw-Hill Book Co., Inc., 1956, pp. 71-76.

21. Tanner, Watson H.: Charts for Estimating Rotary Wing Performance in Hover and at High Forward Speeds. NASA CR-114, 1964.

22. Abbott, Ira H.; Von Doenhoff, Albert E.; and Stivers, Louis S., Jr.: Summary of Airfoil Data. NACA Rep. 824, 1945.

23. McCormick, Barnes W., Jr.: Aerodynamics of V/STOL Flight. Academic Press, Inc., 1967, Sec. 2.

24. Gessow, Alfred; and Myers, Garry C., Jr.: Aerodynamics of the Helicopter. The Macmillan Co., c.1952. (Republished 1967 by Frederick Ungar Pub. Co.)

25. Tanna, H. K.: Theoretical Study of High-Frequency Helicopter Rotor Rotational Noise. I.S.V.R. Contract Rep. No. 70/3 (Contract Nos. DA-ERO-591-70-G001 and AT/2040/072/SRA), Univ. of Southampton, Sept. 1970. (Available from DDC as AD 721 661.)

26. Garrick, I. E.; and Watkins, Charles E.: A Theoretical Study of the Effect of Forward Speed on the Free-Space Sound-Pressure Field Around Propellers. NACA Rep. 1198, 1954. (Supersedes NACA TN 3018.)

27. Holm, Raymond Gust: Discrete Radiation From the Rotating Blades of an Axial-Flow Compressor. M.S. Thesis, George Washington Univ., Sept. 1972.

28. Morse, Philip M.: Theoretical Acoustics. McGraw-Hill Book Co., Inc., c.1968.

29. Sternfeld, H.; Bobo, C.; Carmichael, D.; Fukushima, T.; and Spencer, R.: An Investigation of Noise Generation on a Hovering Rotor. Part II. D210-10550-1 (Contract DAHC04-69-C-0087), Vertol Div., Boeing Co., Nov. 1972. (Available from DDC as AD 753 397.)

30. Lighthill, M. J.: The Bakerian Lecture, 1961: Sound Generated Aerodynamically. Proc. Roy. Soc. (London), ser. A, vol. 267, no. 1329, May 8, 1962, pp. 147-182.

"The aeronautical and space activities of the United States shall be conducted so as to contribute . . . to the expansion of human knowledge of phenomena in the atmosphere and space. The Administration shall provide for the widest practicable and appropriate dissemination of information concerning its activities and the results thereof."

—NATIONAL AERONAUTICS AND SPACE ACT OF 1958

NASA SCIENTIFIC AND TECHNICAL PUBLICATIONS

TECHNICAL REPORTS: Scientific and technical information considered important, complete, and a lasting contribution to existing knowledge.

TECHNICAL NOTES: Information less broad in scope but nevertheless of importance as a contribution to existing knowledge.

TECHNICAL MEMORANDUMS: Information receiving limited distribution because of preliminary data, security classification, or other reasons. Also includes conference proceedings with either limited or unlimited distribution.

CONTRACTOR REPORTS: Scientific and technical information generated under a NASA contract or grant and considered an important contribution to existing knowledge.

TECHNICAL TRANSLATIONS: Information published in a foreign language considered to merit NASA distribution in English.

SPECIAL PUBLICATIONS: Information derived from or of value to NASA activities. Publications include final reports of major projects, monographs, data compilations, handbooks, sourcebooks, and special bibliographies.

TECHNOLOGY UTILIZATION PUBLICATIONS: Information on technology used by NASA that may be of particular interest in commercial and other non-aerospace applications. Publications include Tech Briefs, Technology Utilization Reports and Technology Surveys.

Details on the availability of these publications may be obtained from:

SCIENTIFIC AND TECHNICAL INFORMATION OFFICE

NATIONAL AERONAUTICS AND SPACE ADMINISTRATION

Washington, D.C. 20546